



Technische Universität München

The present work was submitted to the Chair of Space Mobility and Propulsion

presented by

Sven Julius Steinert

Student ID No.: 03773515

Master Thesis

Experimental Characterisation of the XR-100 Resistojet in the ESA Propulsion Laboratory

Munich, November 19, 2024

Supervising professor: Prof. Dr.-Ing. Chiara Manfretti

Assistant supervisor: Ing. Dott.ssa Davina Maria Di Cara (ESA)

1st examiner: Prof. Dr.-Ing. Chiara Manfretti

Eidesstattliche Erklärung

Hiermit erkläre ich, dass die vorliegende Arbeit von mir selbstständig verfasst wurde, und dass keine anderen als die angegebenen Hilfsmittel benutzt wurden. Die Stellen der Arbeit, die anderen Werken dem Wortlaut oder Sinn nach entnommen sind, sind in jedem einzelnen Fall unter Angabe der Quelle als Entlehnung kenntlich gemacht. Diese Erklärung erstreckt sich auch auf in der Arbeit enthaltene Grafiken, Zeichnungen, Kartenskizzen und bildliche Darstellungen.

Ich erkläre mich außerdem damit einverstanden, dass meine Master-, Bachelor- oder Semesterarbeit vom Lehrstuhl auf Anfrage fachlich interessierten Personen, auch über eine Bibliothek, zugänglich gemacht wird, und dass darin enthaltene Ergebnisse sowie dabei entstandene Entwicklungen und Programme vom Lehrstuhl für Raumfahrtantriebe und -mobilität uneingeschränkt genutzt werden dürfen. (Rechte an evtl. entstehenden Programmen und Erfindungen müssen im Vorfeld geklärt werden.)

München, 19.11.2024



Ort, Datum

Unterschrift

Name: Sven Julius Steinert
Matrikelnummer: 03773515

Master Thesis

Experimental Characterisation of the XR-100 Resistojet in the ESA Propulsion Laboratory

Topic

The European Space Agency (ESA) is conducting both internal research activities for ESA missions as well as industry collaborations at the European Space Research and Technology Centre (ESTEC) in Noordwijk, Netherlands. In the ESA Propulsion Laboratory (EPL) the department for electric propulsion (TEC-MPE) is executing characterisation-, acceptance-, and endurance-tests for electric propulsion thrusters in their vacuum facilities. From resistojets to arcjets, hall thrusters, field emission electric propulsion thrusters, gridded ion engines, numerous implementations of electric propulsion were tested in this laboratory. Resistojets are hereby the bridging piece between chemical- and electric propulsion, which offer a noticeable increase in performance compared to a cold gas thrusters for a relatively small increase of system complexity.



Figure: Vacuum Facility in the ESA Propulsion Laboratory
https://www.esa.int/ESA_Multimedia/Images/2014/05/Preparing_vacuum_chamber_in_Propulsion_Lab

In this thesis, the XR-100 resistojet, a sub 100 W class thruster from SITAEL, formerly ALTA SpA, shall be characterised in a test in one of the vacuum facilities in the EPL, specifically in the Small Plasma Facility (SPF). This includes the utilisation of a thrust balance, suitable to measure milli-newtons in thrust. Specifically, the Imperial College London (ICL) thrust balance will be used for this test, which involves calibration and post-processing procedures. The assembly of suitable control and measurement equipment for the thruster operation and installation on the vacuum chamber is to be performed. Complemented by a data acquisition system for gathering of the measurement data. This thesis will be conducted on site at ESTEC in collaboration with ESA.

Tasks

- Literature research on the operating principles of resistojets
- Test setup definition, assembly and execution on the vacuum facility
- Conducting of ESA internal documentation and review stages (TRR, PTR, TRB)
- Enhancing the ICL thrust balance operation by automation of procedures
- LabView software development for the data acquisition system
- Uncertainty budget calculation of the acquired mass flow and thrust
- Determination of the backpressure response of the chamber
- Modelling of the expected thrust and specific impulse under test conditions
- Comparison of experimental measurements to the model
- Documentation and presentation of the results

Contact

Prof. Chiara Manfretti
chiara.manfretti@tum.de

Abstract

Space propulsion thrusters are core elements of any spacecraft, that requires mobility. Electric Propulsion (EP) hereby covers a particular niche in that segment, which utilises electrical energy for thrust creation. As these space thrusters are designed for operation under vacuum conditions, ground based testing ideally replicates those low pressure environments in a vacuum facility for a performance characterisation. In this study, one such characterisation is conducted at the European Space Agency (ESA) on the XR-100 resistojet. The experimental setup was hereby assembled and conducted in the ESA Propulsion Laboratory (EPL), located at the European Space Research and Technology Centre (ESTEC), Netherlands.

This study documents the process of a space thruster characterisation. A concise modelling of the thruster performance is created that is later compared with the experimental results. An extensive list of equipment is listed, that was used in this test to sense and control important parameters before and during the test. In this test the Imperial College London (ICL) Thrust Balance (TB) is used, which can measure particularly low thrust levels of milli-newtons. This study gives special attention to the operation and evaluation of this thrust balance, where multiple enhancements have been implemented. These are the automation of calibration procedures, the automation of the post-processing, enhanced filtering methods for the thrust signal and an extended investigation on the uncertainty. In compliance to the EPL procedures an Uncertainty Budget Calculation (UBC) has been conducted for both the mass flow measurements and the thrust measurements, which are then combined into the description of the specific impulse. Those parameters are the most important performance values, which represent the target values of a thruster characterisation.

The test execution was performed over the main degree of freedom of the resistojet, the inlet pressure, which can linearly scale the thrust. This characterisation was successfully performed in cold flow conditions. The second degree of freedom is the injection of power, which increases the gas temperature and scales the mass flow and specific impulse. Unfortunately, one of the heaters of the resistojet broke during operation, which is why no steady state characterisation could be determined in this operational mode.

When the acquired results are compared to previous characterisations of this thruster unit, a certain alignment with the reference data and the developed model is achieved, however a deviation in the measured thrust remains. The findings suggest that the measured thrust overshoot can only be partially explained by the determined uncertainty, and point to further sources of uncertainty on the thrust balance.

This work demonstrates ground based testing of a space thruster with an applied methodology to uncover deficiencies and the implementation of improvements.

Acknowledgements

I want to express my deepest gratitude to my parents who are the foundation of my personality, on which i was able to build my enthusiasm for physics and space. To my older sisters, who have shaped my childhood and have let me look ahead since an early age. And to my girlfriend, who lifts me up to reach for my dreams and that i am always happy for to have her by my side. To my friends, who i am spending a wonderful life with.

I would like to thank Paul Zabel for supercharging my career entry into space science. Also Prof. Chiara Manfretti, who has guided and supported me throughout my studies and provided by her chair a platform to discover my ultimate passion. And I want to thank Davina Di Cara who gave me the chance to prove myself in electric propulsion, by putting her trust into me when she selected me for an internship at ESA.

To all my colleagues, that I have gotten to know over my time at ESTEC. Which is especially true for my laboratory colleagues, Maxime, Therese, Brenda, Lisa, Hassam and Juliusz. I am grateful for the time I have spent and the experience that I have gained with you. In particular, I want to thank Therese, who supported me in conducting this test, in all its ups and downs.

And thank you, the reader, for taking your time to explore this topic together with me.

Contents

List of Figures	I
List of Tables	III
List of Symbols	V
1. Introduction	1
1.1. Background and Motivation	1
1.2. Objectives of this Thesis	1
2. Electric Propulsion Concepts	3
2.1. Overview	3
3. Theoretical Background	11
3.1. Fundamentals of Resistojet Operation	11
3.2. Performance Parameters of Resistojets	12
3.3. Modeling Approach for Resistojet Performance	12
3.3.1. Heat Model	12
3.3.2. Nozzle Model	16
3.3.3. Model Summary	20
4. Experimental Setup	21
4.1. Overview of the ESA Propulsion Laboratory	21
4.2. ESA EPL process stages	22
4.3. Test Item Description	23
4.3.1. Thruster	23
4.3.2. Thrust Balance	24
4.4. Test Objectives	25
4.5. Test Facility	30
4.6. Test Setup	32
4.6.1. Physical	32
4.6.2. Data Acquisition and Software	36
4.6.3. Electrical	38
4.6.4. Thermocouples	41
4.6.5. Fluidic	42
4.7. Measurement Equipment and Calibration	43
4.7.1. Electrical	43
4.7.2. Physical	43

4.7.3. Auxiliary	48
5. Results and Analysis	49
5.1. Post Processing	49
5.1.1. VCA Characterisation	49
5.1.2. Cross Calibration	50
5.1.3. In-situ Calibration	51
5.1.4. Thrust Measurement Method	53
5.1.5. Pressure Variation Test	58
5.2. Test Results	59
5.2.1. Cold Flow Test	59
5.2.2. Hot Flow Test	61
5.3. Uncertainty Calculation	64
5.3.1. Mass Flow Uncertainty	64
5.3.2. Thrust Uncertainty	68
5.3.3. Specific Impulse Uncertainty	75
5.4. Chamber Response	75
5.5. Model Comparison	76
6. Conclusion and Outlook	77
Bibliography	79
A. Appendix	83
A.1. Resistivity of Tungsten	83
A.2. Flank Detection Algorithm	83
A.3. Heat Capacity Ratio Map of Argon	84
A.4. VCA Characterisation Data	85
A.5. Cross Calibration Data	86
A.6. EPL Noise Characterisation	87

List of Figures

2.1. “Schematic drawings of the main EP systems: (a) resistojet, (b) arcjet, (c) Hall thruster, (d) HEMP thruster, (e) ECR thruster, (f) radiofrequency ion thruster, (g) electron bombardment thruster, and (h) FEEP.” - Holste et al.	4
2.2. Operational Arcjet (TALOS, University Stuttgart)	4
2.3. Operational Hall Effect Thruster (PPS-1350G, Safran Aircraft Engines, originally CNES, 2015)	5
2.4. Operational High Efficiency Multistage Plasma Thruster (HTA, HEMPT-NG)	6
2.5. Operational Radiofrequency Ionisation Thruster (BIT-3 RF, Busek)	6
2.6. Operational Gridded Ion Thruster - Kaufman Thruster (T6, QinetiQ)	7
2.7. Operational Magneto-Plasma-Dynamic Thruster (SX3, University Stuttgart)	7
2.8. Operational Field Emission Electric Propulsion Thruster (IFM Nano, Enpulsion)	8
2.9. Exhaust velocities as a function of typical vehicle accelerations.	9
3.1. “Sectional view of UoSat-12 100-W resistojet”	11
3.2. Simplified heat transfer model between the main entities in the XR100 resistojet	13
3.3. Converging diverging nozzle with notation allocation	17
4.1. The ESA Propulsion Laboratory (EPL) (picture made in 2009).	21
4.2. The XR100 resistojet in the ESA propulsion laboratory	23
4.3. The Imperial College London Thrust Balance in the EPL	24
4.4. CAD rendering of the Imperial College London Thrust Balance	25
4.5. Primary pumps on the SPF used in this test (PP5,PP6 and PP7,PP8)	30
4.6. Schematics of the Small Plasma Facility (SPF) Vacuum Facility	31
4.7. Front view of the entire test setup	32
4.8. XR100 mounted to the Imperial College London thrust balance	32
4.9. Front view of the test setup inside the vacuum facility	33
4.10. Right view of the test setup inside the vacuum facility	33
4.11. Main view of the test setup with key components marked	34
4.12. Side view of the test setup with key components marked	35
4.13. Resistojet data acquisition system (RJ DAQ)	36
4.14. Extra data acquisition system (EXTRA DAQ)	37
4.15. ICL thrust balance data acquisition system (ICL DAQ)	37
4.16. Electrical wiring of the RJ DAQ	38
4.17. Electrical wiring of the EXTRA DAQ	39
4.18. Electrical wiring of the ICL DAQ	40
4.19. Vacuum feedthrough of the electrical power connections to the resistojet	40

4.20. Location of thermocouples: TC1 thruster internal (top left), TC2 SPF gas temperature (top right), TC3 balance flexure block (bottom left) and TC4 thruster interface plate (bottom right)	41
4.21. Fluidic setup marked with key components	42
5.1. Linear fit for the VCA characterisation	49
5.2. Pattern alignment of the auto-cross-calibration.	50
5.3. Linear fit for the cross calibration	51
5.4. Pattern alignment of the auto in-situ calibration	52
5.5. Distribution of the time step variation in the two thrust measurements	54
5.6. Fast Fourier transform of the cold flow measurement in the frequency domain	54
5.7. Filtered fast Fourier transform of the cold flow measurement in the frequency domain	55
5.8. Result of the natural frequency removal of the cold flow laser distance data	55
5.9. No thrust phases marked in the filtered laser distance of the cold flow test	56
5.10. Zero reference $Z(t)$ determination of the cold flow measurement (closeup)	57
5.11. Displacement $D(t)$ of the cold flow measurement	57
5.12. Thrust $F(t)$ of the cold flow measurement	58
5.13. Cold flow test timeline in normalised units (steady state sections marked in grey)	59
5.14. Performance map of the XR-100 in cold gas mode (normalised)	60
5.15. Thrust results of multiple tests of the XR-100 in cold gas mode (normalised)	61
5.16. Hot flow test timeline in normalised units	62
5.17. The firing XR100 resistojet, emitting a point of light inside the vacuum facility during its heat up phase	63
5.18. Performance map of the XR-100 in cold gas mode compared to the model	76
A.1. The heat capacity ratio γ of the gas phase of Argon depending on temperature and pressure.	84
A.2. Noise spectral density (NDS) on structures with no thrust applied of a previous test in the vacuum facility GALILEO on the uNTB	87
A.3. Noise spectral density (NDS) with thrust applied of a previous test in the vacuum facility GALILEO on the uNTB	87

List of Tables

3.1. Fitting constants for the argon solidification line	19
4.1. Service Level Definition	22
4.2. Definition of the SL plan for test activities in the EPL according to EPL-Process-Definition (O = optional, GP = general process applicable/ no records required)	22
4.3. Technical Specifications of the XR100 model in 2015 according to its product sheet.	23
4.4. Test Objectives as Pass Fail Criterion	26
4.5. Electrical Measurement Equipment	44
4.6. Physical Measurement Equipment	47
4.7. Auxiliary Equipment	48
5.1. In-situ calibration baseline result	52
5.2. In-situ calibration spot check result	53
5.3. Result of the pressure variation test in normalised units	58
5.4. Result table of the cold flow test in normalised units	60
5.5. Comparison of the cold flow test to the acceptance test in normalised units	60
5.6. Variable definition of the mass flow uncertainty budget calculation	64
5.7. Mass flow uncertainty influences summary, types and distributions	64
5.8. Mass flow uncertainty normalised GUM Workbench Pro result table of OP1	67
5.9. Mass flow uncertainty normalised GUM Workbench Pro result table of OP13	67
5.10. Mass flow uncertainty result table in normalised units	67
5.11. Variable definition of the thrust uncertainty budget calculation	68
5.12. Thrust uncertainty influences summary, types and distributions	69
5.13. Effect of the coil alignment on the cross calibration gradient c_1	72
5.14. Thrust uncertainty normalised GUM Workbench Pro result table of OP1	74
5.15. Thrust uncertainty normalised GUM Workbench Pro result table of OP13	74
5.16. Thrust uncertainty result table in normalised units	74
5.17. Specific impulse uncertainty result table in normalised units	75
A.1. Resistivity of tungsten depending on temperature	83
A.2. Result data table of the VCA Characterisation	85
A.3. Result data table of the auto cross calibration	86

List of Symbols

General Symbols

\varnothing	[m]	Diameter
\mathfrak{M}	[kg/mol]	Molar mass
A	[m ²]	Area
B	[Tesla]	Magnetic field
b_{cal}	[mm]	Intercept of the sensitivity calibration
C	[-]	Fitting coefficient
c	[J/(kg · K)]	Specific heat capacity
C_p	[J/K]	Heat capacity
c_1	[mm/mA]	Gradient of the cross calibration
c_2	[mm]	Intercept of the cross calibration
D	[mm]	Displacement
E	[V/m]	Electric field
f	[Hz]	Frequency
F	[N]	Force / Thrust
$F_{\square \rightarrow \square}$	[-]	View factor
g_0	[m/s ²]	Standard gravity
H	[J]	Enthalpy
hw	[-]	Half width
I	[A]	Current
I_{sp}	[s]	Specific impulse
k	[-]	Coverage factor
k	[W/(m · K)]	Thermal conductivity
l	[m]	Length

L	[mm]	Laser distance
Ma	[-]	Mach number
N	[-]	Number of samples
p	[Pa]	Pressure
P	[W]	Power
Q	[J]	Heat
R	[Ω]	Resistance
R	[J/(kg · K)]	Gas constant
R^2	[-]	Coefficient of determination
R_0	[J/(kg · mol)]	Universal gas constant
s	[-]	Sample standard deviation
S_{cal}	[mm/mN]	Sensitivity parameter
S_{eff}	[L/s]	Effective pumping speed
T	[K]	Temperature
t	[s]	Time
u	[-]	Standard uncertainty
U	[V]	Voltage
V	[m/s]	Velocity
v_1	[mN/mA]	Gradient of the VCA characterisation
v_2	[mN]	Intercept of the VCA characterisation
x	[-]	Sample measurement
x	[m]	Spatial coordinate
x	[mm]	Displacement measurement
Z	[mm]	Zero reference

Greek Symbols

α	[-]	Absorptivity
α	[-]	Sensitivity coefficient (uncertainty)
Δ	[-]	Finite difference
δ	[-]	Infinitesimal difference
η	[-]	Efficiency

Γ	[-]	Compressed term of the heat capacity ratio
γ	[-]	Heat capacity ratio
∂	[-]	Partial derivative
ρ	[$\Omega \cdot m$]	Electrical resistivity
σ	[-]	Standard deviation
σ_b	[$W / m^2 \cdot K^4$]	Stefan–Boltzmann constant
ε	[-]	Emissivity
ϱ	[kg/m^3]	Density
$\vec{\phi}_q$	[W/m^2]	Heat flux density

Subscripts

\dot{m}	Mass flow
∞	Infinity
$align$	Alignment
Ar	Argon
$axis$	Axis aligned
$back$	Background
$calc$	Calculated
$calib$	Calibration
cos	Misalignment cosine term
c	Chamber
c	Combined (uncertainty)
el	Electric
e	Exit
e	Expanded (uncertainty)
$filament$	Filament
fit	Fitted
F	Thrust
f	Flow
$heater$	Heater
I_{sp}	Specific Impulse

\square_{in}	Inlet
\square_{laser}	LASER (light amplification by stimulated emission of radiation)
\square_{leak}	Leakage
\square_{life}	Lifetime
\square_{meas}	Measured
\square_n	Natural
\square_{press}	Pressure variation
\square_{PT}	Pressure transducer
\square_{rad}	Radiation
\square_{rand}	Random
\square_{read}	Reading
\square_{real}	Realistic
\square_{rel}	Relative
\square_{Scal}	Sensitivity Parameter
\square_{set}	Set value
\square_{solid}	Solidification
\square_{sp}	Specific
\square_{St}	Steel
$\square_{thruster}$	Thruster
\square_{th}	Throat
\square_{ult}	Ultimate
\square_{vap}	Vapour
\square_{VCA}	Voice coil actuator
\square_W	Tungsten

Special Symbols

\square	Average
\square	Time derivative / Flow

Abbreviations

CAD	computer-aided design.
CFP	cold flow performance.
DAQ	data acquisition.
ECR	Electron Cyclotron Resonance.
EP	Electric Propulsion.
EPL	ESA Propulsion Laboratory.
ESA	European Space Agency.
ESTEC	European Space Research and Technology Centre.
FEEP	Field-Emission Electric Propulsion.
FFT	fast Fourier transform.
FS	full scale.
HEMPT	Highly Efficient Multistage Plasma Thruster.
ICL	Imperial College London.
ICTV	in-situ calibration threshold value.
MFC	Mass Flow Controller.
MPD	Magneto-Plasma-Dynamic Thruster.
OP	operation point.
PP	Primary Pump.
PSU	Power Supply Unit.
PT	Pressure Transducer.
PTR	Post Test Review.
RD	read value.
RIT	Radiofrequency Ionisation Thruster.
RJ	Resistojet.
RJP	resistojet performance.
SL	Service-level.
SPF	Small Plasma Facility.
TB	Thrust Balance.
TC	Thermocouple.
TP	Turbo Pump.
TRR	Test Readiness Review.
UBC	Uncertainty Budget Calculation.
VCA	Voice Coil Actuator.
VF	Vacuum Facility.
VG	Vacuum Gauge.

1. Introduction

1.1. Background and Motivation

Space propulsion is the empowering piece to reach a target destination practically anywhere in our solar system. As a launcher can currently only inject a payload on a specific escape trajectory or an orbit around earth, an on-board propulsion system is, what enables advanced maneuverability in space and high fidelity missions including precise maneuvers as gravity assists. The historical bedrock is chemical space propulsion, where highly reactive chemicals are deployed to release their bond energy into a hot gas that can be expanded through a rocket nozzle. Chemical space propulsion captivates by its high thrust capabilities, that can achieve major orbital changes in seconds to minutes. The one downside it has, is its domination of system mass made up by the propellant. This is caused by an upper limit on specific impulse, that the chosen chemical reaction can achieve. This is the point where electrical space propulsion overcomes these limitations. It's operation fundamentally differs by using electrical energy to accelerate the expended mass. This objective is simple, yet the solution space to this task is incredibly rich in variety. The most commonly used implementations are ion engines, where through a chosen process ions are created from a neutral propellant which are then accelerated by an electric field. An operational principle like this completely re-defines any limits in possible specific impulse, as the kinetic energy of an ion is set by its charge and the applied voltage alone. In principle, only the speed of light marks the end of these possibilities. In real life however, there are many good reasons to stop way earlier. Reasons as diminishing returns in propellant mass saving and limited power availability are hereby the typical show stoppers. Practical electric propulsion systems typically surpass chemical propulsion systems by the order of one magnitude in specific impulse. Their biggest downside however is their low thrust level, which typically only ranges in the order of hundred's of mN. This results in the necessity to fire an electric thruster over weeks or months to achieve the desired change in velocity. When found in a suitable mission scenario, an electric propulsion system ultimately shines by an overall lower system mass, for the expense of a longer travel time. Therefore both chemical and electric space propulsion have their own application regime and together make up the state of the art technology for human kinds space exploration. To advance our capabilities in these methods, experimental testing is a key component to try out new implementations or to verify expected performances.

1.2. Objectives of this Thesis

This thesis is the outcome of my stay of half a year at the European space agencies propulsion laboratory in the section of electric propulsion. Research activities on electric propulsion are coordinated from here all across Europe, as well ESA mission related testing and industry prototype testing is holding place in this laboratory. The ESA Propulsion Laboratory (EPL) is the leading facility in the public domain in Europe

and the birthplace of electric propulsion at ESA. Decades in testing experience across many missions and projects is accumulated here in personnel and hardware. The objective of this thesis is to personally deeply acquire the methods that are used here for experimental testing and apply them on an example, the resistojet. As shown later by the test equipment, it becomes obvious that a characterisation of a thruster includes a massive amount of support hardware from a wide spectrum of technologies. Planning, utilising, controlling and post-processing all those instruments correctly is hereby exemplary for the characterisation of any electric propulsion thruster. This means that the general objective surpasses the individual parameter test objectives, by being a demonstrator for the ability of thruster characterisation in general.

2. Electric Propulsion Concepts

As tasered in the introduction, electric propulsion systems have a rich variety of implementations and utilised concepts. The main concepts are introduced here together with the resistojet that is later experimentally characterised.

2.1. Overview

Electric propulsion systems are often categorised by their method of primary acceleration contribution into electro-thermal, electro-magnetic and electro-static. In many of those cases, these physical effects overlap, which sometimes makes a definite classification harder than may be initially expected.

Resistojet The most simple implementation of electric propulsion is the resistojet. This principle is effectively an additive to a kinetic type thruster, the cold gas thruster. The cold gas thruster is similar to chemical propulsion systems, however its energy stems entirely from the elastic potential energy of the compressed gas, making it neither electric nor chemical but here called kinetic. The performance of a cold gas thruster depends highly on the utilised gas and its molecular weight \mathfrak{M} and its heat capacity ratio γ and typically lies between 50 to 100 seconds in specific impulse [48]. Now the addition that a resistojet is doing is heating the gas inside the chamber before it is expanded through the nozzle. The exhaust velocity has a positive correlation with the gas chamber temperature, therefore increasing the temperature leads to an increased specific impulse. This is achieved by an electrical heater that is embedded within the thruster unit as a filament. With this addition of an electrical heater, the specific impulse can be increased to hundreds of seconds, but typically lower than 500 seconds [21] due to temperature and material constraints. Due to the utilisation of thermal energy, it is categorised as electro-thermal [48]. The concept of a resistojet is visualised in cell a) of Figure 2.1.

Arcjet The arcjet extends the core idea of the resistojet, to produce a hotter gas to expand by a nozzle. It overcomes the temperature limitations of the resistojet by not using a heater but striking an electrical arc through the gas itself. This is typically achieved by the cathode being placed in the center of the chamber before the nozzle and the anode closer to the diverging section of the nozzle. A laminar zone is created in the constrictor, which enables a stable operation and heat transfer to the throughput gas. The electrical arc can vastly exceed the melting temperature of any material and heat the gas to extreme levels in temperature, which starts dissociation and ionisation effects [4]. The gas is being only weakly ionised, which primarily classifies the arcjet as an electro-thermal and secondary as electro-magnetic thruster [48]. The limitations are hereby again the materials that are exposed with the heat first, which results in a specific impulse of up to 800 seconds and a rather low thrust efficiency of around 50 % [48]. The concept of an arcjet is visualised in cell b) of Figure 2.1. An operational arcjet is depicted in Figure 2.2.

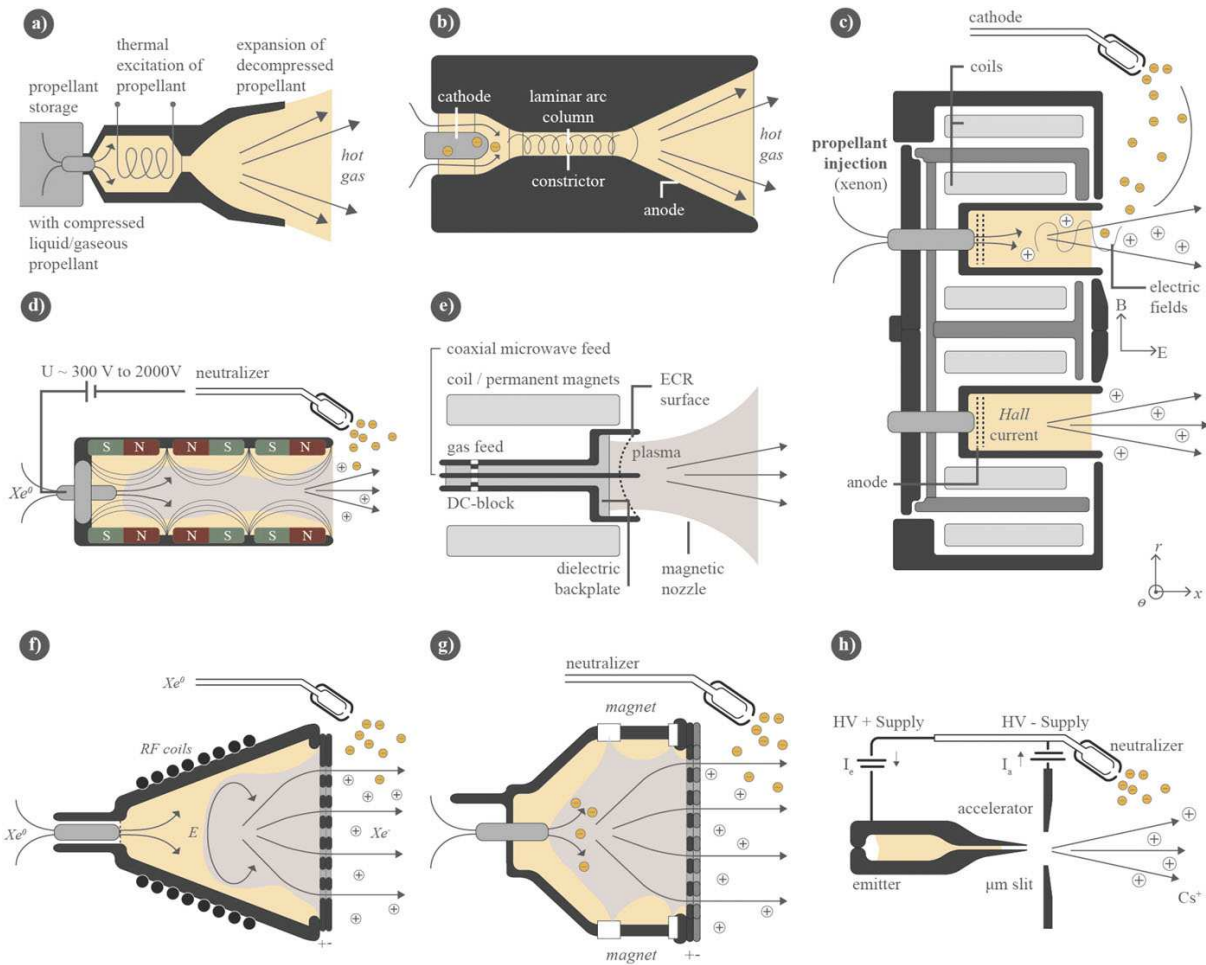


Figure 2.1.: “Schematic drawings of the main EP systems: (a) resistojets, (b) arcjet, (c) Hall thruster, (d) HEMP thruster, (e) ECR thruster, (f) radiofrequency ion thruster, (g) electron bombardment thruster, and (h) FEEP.” - Holste et al. [25]

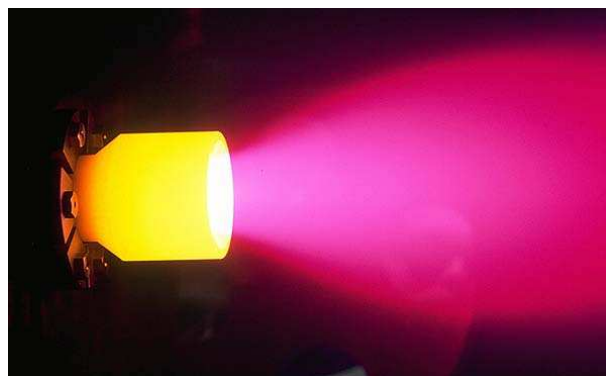


Figure 2.2.: Operational Arcjet (TALOS, University Stuttgart) [42]

Hall Thruster With the hall thruster, the realm of ion utilisation is now finally entered. The operational principle can be simply described by an ionisation of neutral gas through electron bombardment and the acceleration of the ions through an electro-static field. Hereby are the electrons emitted from a cathode and flow into the thruster from the outside into the discharge channel towards the anode which is placed

in the bottom of that discharge channel, where also the inflow of the propellant is located. However, with those pieces alone, the cross section and therefore the interaction probability between the high energy electrons and the in-flowing neutral particles would be extremely low. An applied magnetic field near the exit plane is making all the difference, as by the perpendicular field arrangement of an ExB field, charged particles can be magnetised and are drifting in the off plane direction, the so called ExB drift. This arrangement of a magnetic field is causing the electrons to be effectively trapped due to as their ExB drift causes them to float around the circular discharge chamber but not towards the anode unless they experience a collision. The resulting current of trapped electrons is called hall current, which gives the thruster its name. The categorisation of the hall thruster into either electro-static or electro-magnetic is debatable, as the acceleration of the ions is done via an electro-static field, however the compensation of the reactive force of the electrons is exerted through the magnetic field. Hall thrusters have been developed by the Russians in the 1960s and became the most used electric propulsion system nowadays. Next to Xenon as the classical propellant, also alternative propellants are being used, as for example Krypton on the Starlink mega constellation [44] or oxygen from water in experimentally research [33], where i have even designed myself an implementation recently [47]. All together hall thrusters typically deliver around 2000 s in specific impulse and a higher thrust level than other ion thrusters at a given power [21]. One prominent usage of a hall thruster was ESAs SMART-1 mission, which has set a corner stone for electric propulsion in Europe. [29] With a latest thrust efficiency record of 76 % on a power level of 10 kW [23] they mark one of the most important electric propulsion systems today. The concept of a hall thruster is visualised in cell c) of Figure 2.1. An operational hall thruster is depicted in Figure 2.3.



Figure 2.3.: Operational Hall Effect Thruster (PPS-1350G, Safran Aircraft Engines) [11] Originally CNES, 2015

HEMPT In the Highly Efficient Multistage Plasma Thruster (HEMPT), electrons also enter the discharge channel from an outer cathode. Due to an arrangement of permanent magnets that alter in orientation, a specific magnetic field configuration is created. This field creates ionisation regions in between the magnet stages and also confines the formed plasma. This confinement is minimising the plasma wall interaction and therefore erosion patterns, which is why the HEMPT shows excellent lifetime. The benefits of a HEMPT are low system complexity, low mass, low cost and long lifetime but has a low maturity and flight heritage. The concept of a HEMPT is visualised in cell d) of Figure 2.1. An operational HEMPT can be seen in Figure 2.4.

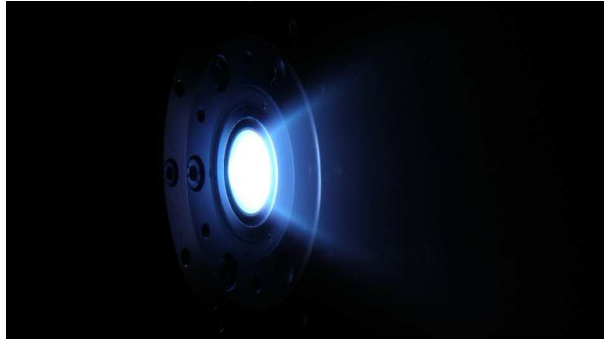


Figure 2.4.: Operational High Efficiency Multistage Plasma Thruster (HTA, HEMPT-NG) [22]

ECR Thruster The Electron Cyclotron Resonance (ECR) thrusters embrace a plasma physics phenomenon, that when electrons are held in a strong enough magnetic field to become magnetised, they gyrate with a fixed frequency. When the electrons are now exposed to an electric field that has the identical frequency, a resonance is created and energy is deposited into the electrons. The high energy electrons ionise the gas and form a plasma. This high temperature plasma is then expanded through a magnetic nozzle to produce thrust. The frequency is usually in the microwave range and specific impulses of around 1000 seconds can be reached but with a thrust efficiency of only 10 % [51]. The benefit of the ECR thruster is their reliability and low cost, but the downsides are low technological maturity and low efficiency. The concept of an ECR thruster is visualised in cell e) of Figure 2.1.

RIT The Radiofrequency Ionisation Thruster (RIT) is also using radio waves to deposit energy into electrons, however in a confined space called plasma chamber. Hereby is the excitation frequency in a closed loop system with a feedback of the plasma. [50] The ions are extracted by a grid configuration of typically two layers. The first grid is positively biased in voltage and the second grid is negatively biased. If a charged particle now randomly enters the hole region in those grids, the electrons are repelled back into the plasma chamber, but the ions get accelerated out instead. This leads to an ion extraction through each of the holes in this grid assembly. The ejected ions are then as typical neutralised by an externally placed cathode. Radio frequency ionisation thruster are currently under development for the ESA mission NGGM [13]. The concept of a RIT is visualised in cell f) of Figure 2.1. An operational RIT can be seen in Figure 2.5.

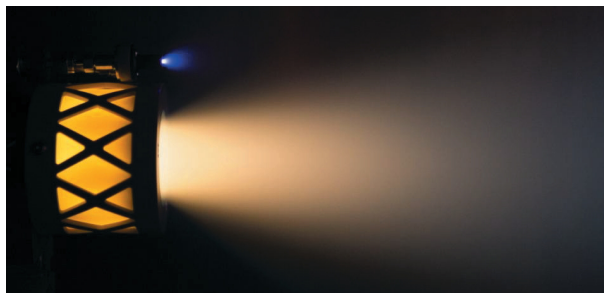


Figure 2.5.: Operational Radiofrequency Ionisation Thruster (BIT-3 RF, Busek) [49]

Gridded Ion Thruster - Kaufman Thruster The Kaufman type gridded ion thruster also utilises a plasma chamber and an extraction via a grid assembly as the RIT, however the ionisation is reached by electron bombardment instead. For this, a hollow cathode is placed inside the plasma chamber to inject electrons. Through a magnetic configuration these electrons create an enhanced ionisation region, efficiently forming a plasma. The gridded ion thruster has prominent flight heritage of the QinetiQ T6 on ESAs BepiColombo mission and the T5 for ESAs GOCE mission. [26] These thrusters achieve 3000 to over 4000 seconds in specific impulse with a high thrust efficiency of 64%. [43] The concept of a gridded ion thruster is visualised in cell g) of Figure 2.1. An operational gridded ion thruster can be seen in Figure 2.6.

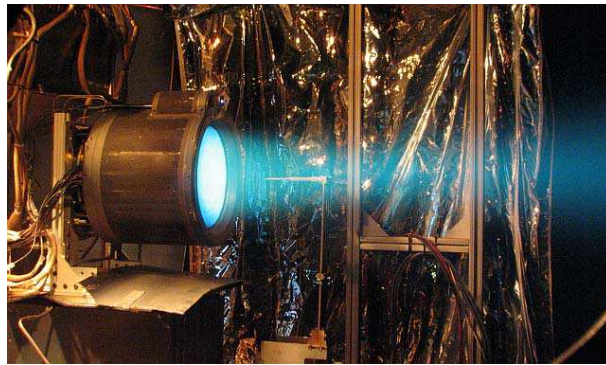


Figure 2.6.: Operational Gridded Ion Thruster - Kaufman Thruster (T6, QinetiQ) [43]

MPD The Magneto-Plasma-Dynamic Thruster (MPD) uses the Lorentz force to accelerate the entire quasi-neutral plasma all together. This is achieved by a steady state of a crossed electric and magnetic field configuration. Hereby is the main acceleration exerted through magnetic interactions, instead the electro-static. The thruster consists of a cylindrical shaped anode, where the cathode is positioned as a pole in the center. An MPD can be either create the magnetic field through the current between the cathode and anode itself, which is then called self-field MPD or it can be provided externally through a coil, which is then called applied-field MPD. [1] These thrusters typically require very high power levels of around 50kW up to 1MW, which is why most testing of these thrusters was ground based only under a low technological readiness level. However, they have an exceptional thrust density and have the best potential for high power applications. An operational gridded MPD can be seen in Figure 2.7.



Figure 2.7.: Operational Magneto-Plasma-Dynamic Thruster (SX3, University Stuttgart) [8]

FEEP The Field-Emission Electric Propulsion (FEEP) thrusters work on the principle that ions can be emitted by an electric field of extreme intensity. In these thrusters a conductive liquid is utilised as propellant. The liquid is exposed to porous needles, which transfer the liquid by capillary forces to the tip of the needle. The needle itself is the anode and an accelerator plate on top is the cathode, with a hole above the needle. Between the anode and the cathode a very high voltage of around 10kV is applied, which creates a strong electric field. Due to the combination of surface tension effects and the exposure to the high electric field, which get intensified towards the tip of the needle, a so called Taylor cone is formed at the very tip. The fluid particles at the tip of that Taylor cone are exposed to an electric field that is strong enough to ionise the particle directly, which creates an emission on the tip of the needle. This concept is typically restricted by low mass flows, as otherwise the Taylor cone becomes unstable, which is why modern FEEP systems embed a high number of these needles together into a so called crown. [39] FEEP systems naturally have a very high specific impulse, due to the high applied voltage, which is often traded in favour of a higher thrust level. The concept of FEEP is visualised in cell h) of Figure 2.1. An operational FEEP thruster can be seen in Figure 2.8.

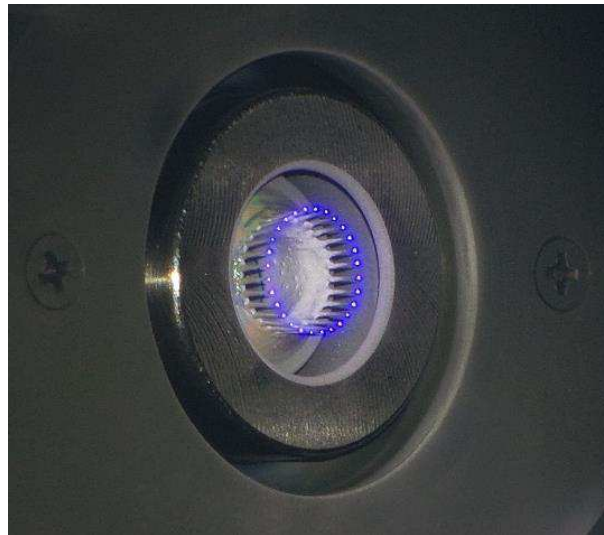


Figure 2.8.: Operational Field Emission Electric Propulsion Thruster (IFM Nano, Enpulsion) [30]

This concludes the overview of electric propulsion systems, where in Figure 2.9 the resistojet can be seen in context with other propulsion methods.

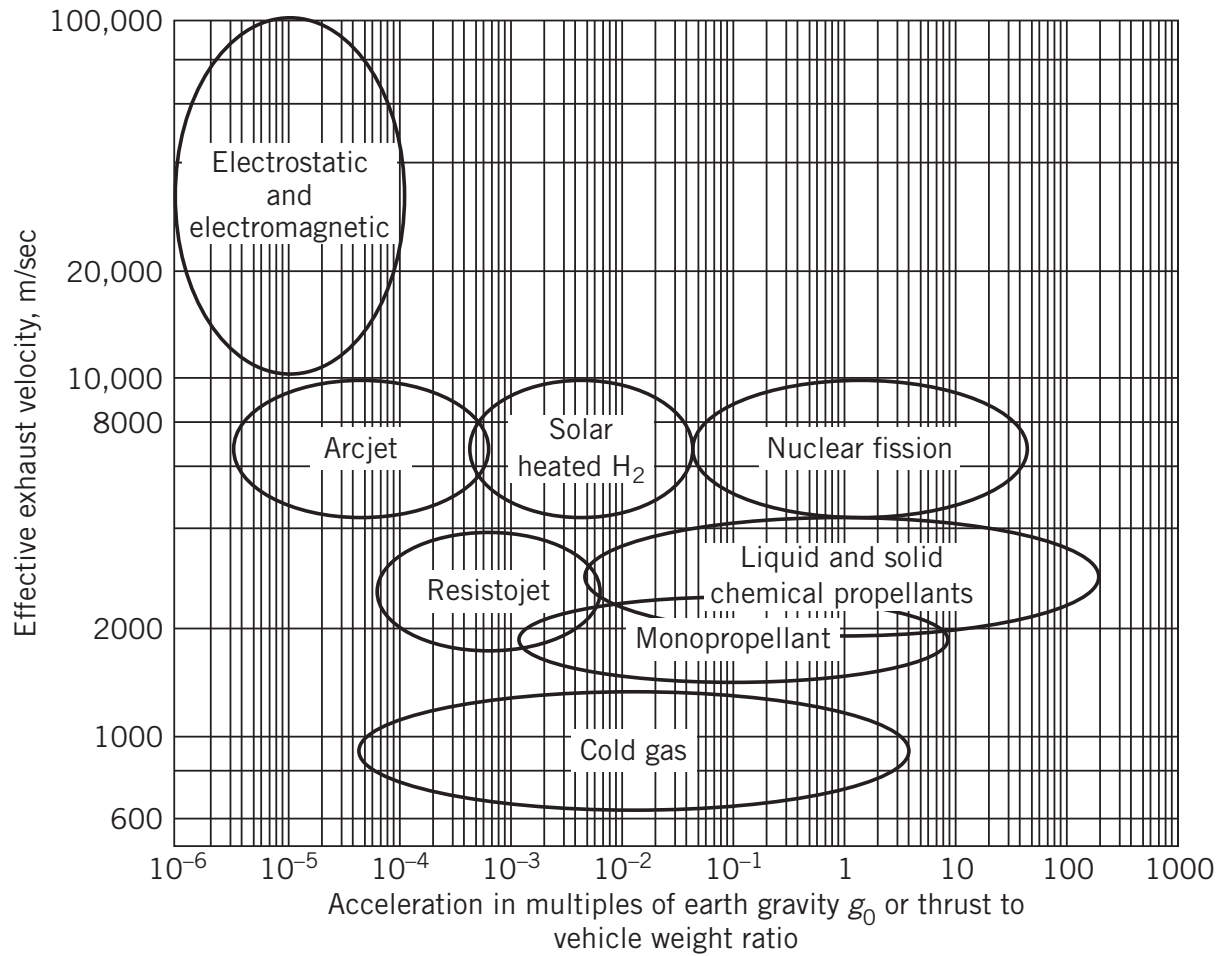


Figure 2.9.: “Exhaust velocities as a function of typical vehicle accelerations. Regions indicate approximate performance values for different types of propulsion systems. The mass of the vehicle includes the propulsion system, but the payload is assumed to be zero. Nuclear fission is shown only for comparison as it is not being pursued.” - Sutton and Biblarz [48]

3. Theoretical Background

3.1. Fundamentals of Resistojet Operation

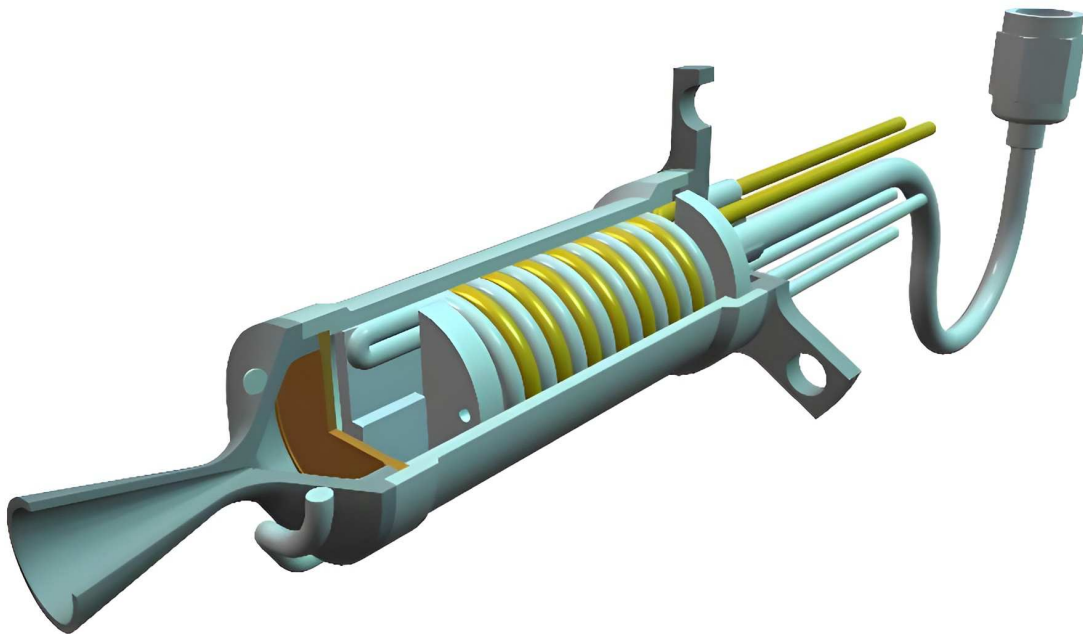


Figure 3.1.: “Sectional view of UoSAT-12 100-W resistojet” - from [2], originally [20]

The operational principle of a resistojet can be simply summarized as a coupling of a cold gas thruster with an electric heater. Through the increased gas temperatures induced by the heating element, higher specific impulses can be achieved. The required internal components can be seen in Figure 3.1, which are mainly the gas inlet pipe, the heat ex-changer with the heating element, a particle filter and the converging diverging nozzle. As a propellant usually non-reactive materials are used which primarily serve the purpose to pick up the heat of the resistor and then to be expanded through the nozzle to create thrust. The particular advantage of resistojets is, that with a relatively small addition of complexity a considerable performance increase in specific impulse can be achieved, through the elevated temperatures. Despite the specific impulse being higher than cold gas thrusters, it is still lower than effectively all other propulsion systems, both electric and chemical, which puts the resistojet in a niche application regime. A resistojet furthermore requires a heat-up and cool-down phase of minutes when operated electrically, which limits the capabilities of achievable impulse bits drastically. Consequentially small impulse bits can only achieved by operating the resistojet in cold gas mode.

3.2. Performance Parameters of Resistojets

The most relevant performance parameters of a resistojet thruster are the level of thrust F and the specific impulse I_{sp} . Additionally the utilization of the electrical power can be evaluated in a thrust efficiency η_F . Important operational parameters are the consumed power P_{el} , the type of usable propellants, the required inlet pressure p_{in} and required voltage U [15].

The level of thrust is only barely altered by the addition of the heating element, as later visible in Equation 3.23. Therefore, the design steps regarding the thrust level are identical to a cold gas thruster. The important parameters here are the type of gas (with its molecular weight \mathfrak{M} and heat capacity ratio γ), the nozzle geometry (with its throat area A_{th} , the exit area A_e) and the chamber pressure p_c .

The specific impulse however, is directly influenced by the increase of chamber gas temperature T_c . An elevated temperature decreases the choked mass flow \dot{m} and simultaneously increases the exit velocity V_e . This results in roughly the same thrust, but with less mass flow, hence an increase in specific impulse. This is summarised in the proportional relation in Equation 3.1.

$$I_{sp} \propto V_e \propto \sqrt{T_c} \quad (3.1)$$

The parameters to achieve the maximum I_{sp} therefore translate to maximizing T_c , which is directly dependent on the heater design. The heater filament equilibrium temperature T_{Heater} is aimed to be as high as possible to offer a higher temperature gradient and hence a bigger heat transfer from the filament to the gas. Additionally, the internal geometry highly influences the flow around the heater and consequentially the heat transfer. Hereby is a longer exposure to the heater filament desired, which is often accomplished by forcing the gas through a spiral to increase the flow path [15].

3.3. Modeling Approach for Resistojet Performance

In this chapter a model is developed to predict the performance that is later compared to the experimental results.

3.3.1. Heat Model

The general entities in a resistojet have been abstracted into Figure 3.2 in order to get an overview of the thermal influences during operation. In steady state conditions of the resistojet, a thermal equilibrium exists between the listed entities. When the individual heat contributions are attempted to be quantified, it quickly becomes evident that the full knowledge of the internal geometry and materials is required. Even though there is some information present to me about the design, there is no internal geometry available that would be required to determine the equilibrium accurately. The consequence of this is, that the heat model will be an unspecified parameter model or a model overview, that can only present an approach and no input-output predictions.

The relevant heat transfers can be hereby categorised into the electrical induced heat creation, the conductive heat transfer and the radiation heat transfer. In the following paragraphs an analytical description is derived to quantify these influences.

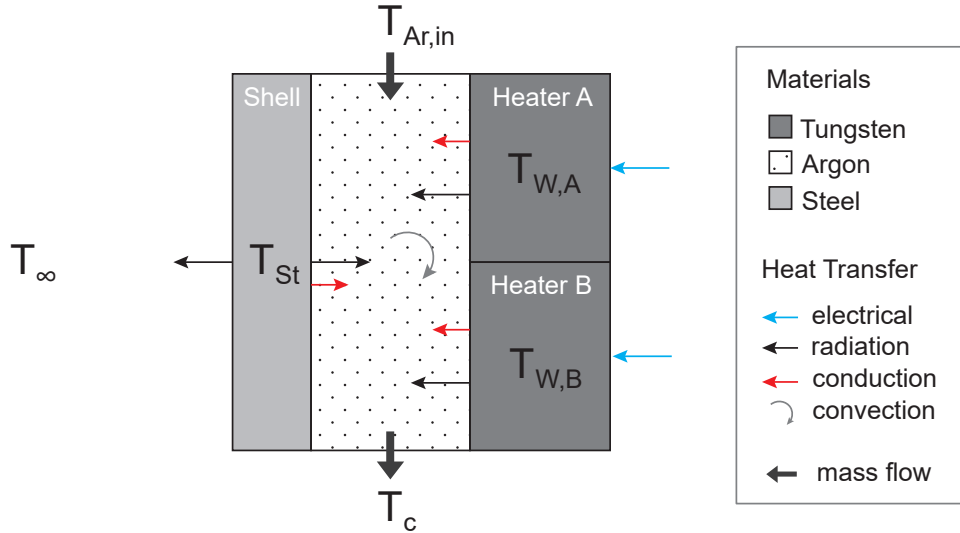


Figure 3.2.: Simplified heat transfer model between the main entities in the XR100 resistojet

Electrical

The first influence is the heat induction into the thruster from the electrical energy. The heat is hereby created directly via ohms law by the filaments resistance. The very crucial point is hereby the temperature dependent resistance of the material of the filament and its melting point. When the filament is operated with a constant voltage, this has a slight self dampening effect, as the resistance increases with filament temperature and therefore less current can flow and less power is absorbed. However, this effect is not nearly enough to prevent overheating and melting of the filament. As the temperature of the filament is crucial for further heat transfer to the gas, and therefore its efficiency, the filament temperature has to be accurately balanced. In order to achieve this, the resistivity of the filament material, in this case tungsten, needs to be known precisely. Table A.1 holds a collection of measurements that have been determined in fundamental research on the resistivity of tungsten [14].

This temperature dependent relationship is highly non-linear and is fitted by the authors [14] into the continuous formulation for the resistivity of tungsten $\rho_W(T)$ in Equation 3.3.

$$\rho_W(T) = \begin{cases} 1K \leq T \leq 40K & \rho_W(T) = 0.000015 + 7 \cdot 10^{-7} \cdot T^2 + 5.2 \cdot 10^{-10} \cdot T^5 \\ 40K \leq T \leq 90K & \rho_W(T) = 0.14407 - 1.16651 \cdot 10^{-2} \cdot T + 2.41437 \cdot 10^{-4} \cdot T^2 \\ & \quad - 3.66335 \cdot 10^{-9} \cdot T^4 \\ 90K \leq T \leq 750K & \rho_W(T) = -1.06871 + 2.06884 \cdot 10^{-2} \cdot T + 1.27971 \cdot 10^{-6} \cdot T^2 \\ & \quad + 8.53101 \cdot 10^{-9} \cdot T^3 - 5.14195 \cdot 10^{-12} \cdot T^4 \\ 750K \leq T \leq 3600K & \rho_W(T) = -1.72573 + 2.14350 \cdot 10^{-2} \cdot T + 5.74811 \cdot 10^{-6} \cdot T^2 \\ & \quad - 1.13698 \cdot 10^{-9} \cdot T^3 + 1.1167 \cdot 10^{-13} \cdot T^4 \end{cases} \quad (3.2)$$

The resistance of the tungsten filament can now be determined by Equation 3.3 with the filament length

l and the filament cross section A . However, these geometric values l and A are unknown for the XR100.

$$R_{filament}(T) = \rho(T) \cdot \frac{l}{A} \quad (3.3)$$

When ohms law is now applied, by operating the resistor with a constant voltage source U , the Equation 3.4 describes the current flow I and Equation 3.5 the power absorption P_{el} of the filament.

$$I = \frac{U}{R_{filament}(T)} \quad (3.4)$$

$$P_{el} = U \cdot I = \frac{U^2}{R_{filament}(T)} \quad (3.5)$$

This power can be directly transferred with the applied time dt to the change in heat ΔQ_{el} caused by resistive heating in Equation 3.6, as there are no losses during this energy conversion.

$$\Delta Q_{el} = P_{el} \cdot \Delta t \quad (3.6)$$

The change in temperature of the filament due to the electrical power induction can be determined by the specific heat capacity for tungsten c_W and the mass of the tungsten filament m_W .

$$\Delta T_{W,el} = \frac{\Delta Q_{el}}{c_W \cdot m_W} \quad (3.7)$$

The mass of the filament is hereby gained over the density and volume of the filament $m_W = \rho_W \cdot l \cdot A$ and requires once again geometric information. The specific heat capacity for is obtained from the molar mass $\mathfrak{M}_W = 183.84E - 3 \text{ kg/mol}$, and the heat capacity C_p , which is again temperature dependent.

$$c_W = C_{p,W}(T)/\mathfrak{M}_W \quad (3.8)$$

The temperature dependent heat capacity of tungsten [10] is supplied a continuous fit in Equation 3.9.

$$C_{p,W}(T) = \begin{cases} 298K \leq T \leq 1900K & C_{p,W}(T) = 23.95930 + 2.639680 \cdot \frac{T}{1000} + 1.257750 \cdot \left(\frac{T}{1000}\right)^2 \\ & - 0.254642 \cdot \left(\frac{T}{1000}\right)^3 - 0.048407 / \left(\frac{T}{1000}\right)^2 \\ 1900K \leq T \leq 3680K & C_{p,W}(T) = -22.57640 + 90.27980 \cdot \frac{T}{1000} - 44.27150 \cdot \left(\frac{T}{1000}\right)^2 \\ & + 7.176630 \cdot \left(\frac{T}{1000}\right)^3 - 24.0974 / \left(\frac{T}{1000}\right)^2 \end{cases} \quad (3.9)$$

Note that Δt is hereby the time step parameter that can be attached with a numerical integrator, like Runge-Kutta 4th order, to simulate the temperature over time. In a final implementation the net change of heat would be determined first from various sources before the change in temperature for an entity is applied.

Radiation

The heat transfer by thermal radiation is based on the emitted power of the Stefan–Boltzmann law, shown in Equation 3.10. The variables are hereby the Stefan–Boltzmann-constant $\sigma_b = 5.670374 \cdot 10^{-8} \frac{W}{m^2 \cdot K^4}$ [32], the emissivity of the material $0 \leq \varepsilon \leq 1$, the surface area A and the surface temperature T .

$$P_{rad} = \sigma_b \cdot \varepsilon \cdot A \cdot T^4 \quad (3.10)$$

When this emitted power is radiated towards a second entity ($1 \rightarrow 2$), not necessarily all photons lie in the line of sight, which creates the view factor $0 \leq F_{1 \rightarrow 2} \leq 1$. Furthermore, not all incoming photons are being absorbed by the second entity, which causes the absorptivity $0 \leq \alpha \leq 1$, which is simplified with the Kirchoff's law to be equal to the emissivity of the second entity ε_2 . As all entities in the heat model have a non-zero temperature, the heat radiation is always evaluated in both ways, as shown in Equation 3.11.

$$\begin{aligned} \dot{Q}_{1,rad} &= \varepsilon_2 \cdot F_{1 \rightarrow 2} \cdot \sigma_b \cdot \varepsilon_1 \cdot A_1 \cdot T_1^4 \\ \dot{Q}_{2,rad} &= \varepsilon_1 \cdot F_{2 \rightarrow 1} \cdot \sigma_b \cdot \varepsilon_2 \cdot A_2 \cdot T_2^4 \end{aligned} \quad (3.11)$$

Due to $A_1 \cdot F_{1 \rightarrow 2} = A_2 \cdot F_{2 \rightarrow 1}$, this can be compressed into the net rate of heat flow in Equation 3.12, which can either be positive or negative.

$$\dot{Q}_{1 \rightarrow 2,rad} = \varepsilon_1 \cdot \varepsilon_2 \cdot F_{1 \rightarrow 2} \cdot \sigma \cdot A_1 \cdot (T_1^4 - T_2^4) \quad (3.12)$$

In the resistojet all entities are part of this radiative heat exchange and need to be evaluated all towards each other to find an entities total net change ΔQ_{rad} , when evaluated over the change in time Δt . Note that the emmissivity for gases, such as the argon in the cavity, is generally very low and is highly pressure and temperature dependent [16]. Due to noble gases having no molecular structure, which would increase the absorptivity due to vibration modes, the emissivity of argon is extremely low. This results for the resistojet that the main portion of the radiation, that is emitted by the filament, is being injected into the shell instead the gas.

The resulting change in temperature for an entity due to radiation can be computed as previously through Equation 3.13, here shown for the shell material. Note that the shell is interacting also with the background temperature T_∞ , which is the main loss of thermal energy in a resistojet.

$$\Delta T_{St,rad} = \frac{\Delta Q_{rad}}{c_{St} \cdot m_{St}} \quad (3.13)$$

Conduction

The heat transfer via conduction does not only occur between the different entities, but also within one material. The limited thermal conductivity is the reason for a material to experience spatial temperature gradients. A proper thermal simulation with a meshing of the entities would cover this problem at best, however in this work, only the core principle is stated to give an overview on the relevant parameters.

The conductive heat transfer generally can be modeled through the heat flux density $\vec{\phi}_q$ by Fourier's law, shown for one dimension in Equation 3.14. The variables are hereby $k(x)$ the thermal conductivity of a material depending on the location x , and the temperature $T(x)$ depending on the location x . The negative notation expresses that the heat flux flows from a higher temperature to a lower temperature.

$$\vec{\phi}_q = -k(x) \cdot \frac{\partial}{\partial x} T(x) \quad (3.14)$$

From this general relationship, two core takeaways for the resistojet can be derived. Firstly, the high thermal conductivity k of the metals (tungsten and steel) have a proportional effect on the heat flux density, which results in a slow internal temperature decline in the metals and a faster decline in temperature per unit of length x for the argon gas. Secondly, the transported heat increases proportionally with the temperature gradient $\frac{\partial}{\partial x} T(x)$, which highlights the importance of the temperature difference at the interface between the tungsten filament and the argon gas.

In steady state conditions a thermal equilibrium with a temperature profile can be calculated, however that the argon gas is being in motion increases the complexity rapidly.

Convection

The convective heat transfer describes the transfer by physical movement of the particles themselves. As the individual atoms for the metals are kept stationary due to their strong lattice bonding, fluids or here gases undergo this phenomena. Under normal conditions, Earth's gravitation supports the uprising of hotter particles, due to their usually decreased density. In space, the gravitational influence and the resulting buoyancy effects fall away, however forced convection is present, as the gas inside the resistojet is forced by a pressure difference through the heating element. This does not only result in a heat transport downstream the heater, but under turbulent flow conditions also an intermixing within the flow canal. A modelling of these effects can be achieved via a computational fluid dynamics simulation of the gas flow through the heating element.

3.3.2. Nozzle Model

The main part of the model will be handled by the nozzle model. In this section the high temperature, high pressure conditions inside the chamber are expanded via a converging diverging nozzle. The relevant parameters are annotated in the illustration in Figure 3.3, which shows an example nozzle cross section.

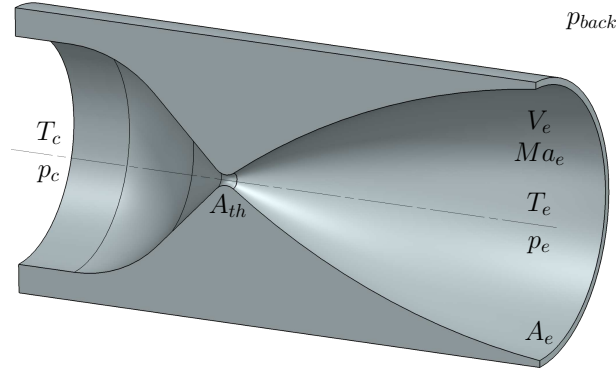


Figure 3.3.: Converging diverging nozzle with notation allocation

The nozzle model which is crafted here determines the performance under choked flow conditions, which is an assumption that is given also for lower pressures for a space thruster. The following set of Equations originate from fundamental rocketry literature [3], under which the performance of Thrust and specific impulse will be computed from.

To define the gas parameters for argon the following definitions have been applied. The specific gas constant of argon R is yielded by the universal gas constant $R_0 = 8.31446 \frac{J}{K \cdot mol}$ [32] and the molar mass for argon $\mathfrak{M} = 39.948 \cdot 10^{-3} \frac{kg}{mol}$ [31]. This results by Equation 3.15 to $R = 208.132 \frac{J}{kg \cdot K}$ for argon.

$$R = \frac{R_0}{\mathfrak{M}} \quad (3.15)$$

The heat capacity ratio γ for argon is set to a constant $\gamma = 1.67$, which is often used by literature [52] and which makes up the major part in the phase diagram, which is plotted in Figure A.1. Note that under extreme conditions, when the argon solidification line is approached, this simplification can introduce errors. By Equation 3.16 the influence of the heat capacity ratio can be put into a compressed form, yielding $\Gamma = 0.7267$ for argon.

$$\Gamma = \sqrt{\gamma} \left(\frac{2}{\gamma + 1} \right)^{\frac{\gamma+1}{2(\gamma-1)}} \quad (3.16)$$

With those parameters defined, the mass flow \dot{m} of a nozzle under choked flow conditions can be directly computed via Equation 3.17, with the chamber pressure p_c , chamber temperature T_c and the throat area A_{th} . Note, that this mass flow is conserved over the nozzle in steady state conditions, and therefore applies over the entirety of the nozzle. With the mass flow determined, already one of the major performance parameters of a thruster is found. Note that \dot{m} increases proportionally with p_c , but decreases with the square root of T_c , which applied on a resistojet means that under constant p_c the increased temperature from the heater will reduce the mass flow.

$$\dot{m} = \Gamma \cdot \frac{p_c \cdot A_{th}}{\sqrt{R \cdot T_c}} \quad (3.17)$$

From here, two different approaches can be applied for the expansion of the nozzle to yield the exit velocity of the gas. If the nozzle is assumed to expand from the chamber pressure p_c to a certain exit

pressure p_e , the exit velocity V_e can be directly determined by Equation 3.18.

$$V_e = \sqrt{\frac{2\gamma}{\gamma-1} \cdot \frac{R_0}{\mathfrak{M}} \cdot T_c \left[1 - \left(\frac{p_e}{p_c} \right)^{\frac{\gamma-1}{\gamma}} \right]} \quad (3.18)$$

If the exit pressure is not to be assumed but determined instead by the geometric dimensions of the nozzle, the following equations model the isentropic expansion specifically. The exit Mach number Ma_e can be converged from Equation 3.19, by iterating an assumption for Ma_e until the known expansion ratio $\frac{A_e}{A_{th}}$ is reached.

$$\frac{A_e}{A_{th}} = \left(\frac{\gamma+1}{2} \right)^{-(\gamma+1)/(2 \cdot (\gamma-1))} \cdot \frac{1}{Ma_e} \cdot \left(1 + Ma_e^2 \cdot \frac{\gamma-1}{2} \right)^{(\gamma+1)/(2 \cdot (\gamma-1))} \quad (3.19)$$

With the exit Mach number found, the exit temperature T_e and exit pressure p_e can be now computed via Equation 3.20 and 3.21.

$$T_e = T_c \cdot \left(1 + \frac{\gamma-1}{2} \cdot Ma_e^2 \right)^{-1} \quad (3.20)$$

$$p_e = p_c \cdot \left(1 + \frac{\gamma-1}{2} \cdot Ma_e^2 \right)^{-\gamma/(\gamma-1)} \quad (3.21)$$

From these conditions the exit velocity V_e can now also be computed in Equation 3.22.

$$V_e = Ma_e \cdot \sqrt{\gamma \cdot R \cdot T_e} \quad (3.22)$$

In both cases, the resulting thrust exerted by the thruster is defined by Equation 3.23. Note that the pressure difference to the back pressure p_{back} can either provide an additional kick in the case for under-expansion ($p_e > p_{back}$) or a drag in the case of an over-expansion ($p_e < p_{back}$).

$$F = \dot{m} \cdot V_e + (p_e - p_{back}) \cdot A_e \quad (3.23)$$

The specific impulse I_{sp} is finally determined via Equation 3.24.

$$I_{sp} = \frac{F}{\dot{m} \cdot g_0} \quad (3.24)$$

With the mass flow, thrust and the specific impulse quantified, the three main performance parameters of the thruster are found.

Additional Considerations As this model is being an 1D isentropic flow calculation, any realistically occurring 3D effects are not covered, as well as surface layer interactions to the nozzle material and its surface roughness. Additionally, with high expansion ratios, the model can yield extremely low exit

temperatures, which could end up in a suggested phase change of the gas to becoming a solid during expansion. This opposes a challenge, as a phase change is not an isentropic process and would need to be modeled separately. The previously mentioned assumed constant heat capacity ratio γ also plays into this problematic regime, as towards the solidification line the assumption does not hold true anymore.

In order to investigate when a result falls into a suggested phase change regime, the solidification line of argon is derived here next. One reference for solidification lines of common vacuum gases is found in a book from 1966 named "Vacuum Technology and Space Simulation" [24]. The plot of the argon solidification line [24] is taken and fitted on the theoretical relationship for solidification lines to yield a continuous description. The theoretical relationship is described by the Clausius-Clapeyron relation which is shown in its approximate form in Equation 3.25, where $\Delta_{vap}H$ is the molar enthalpy of vaporization and C_1 is the first fitting constant.

$$p_{solid}(T) = \exp \left\{ \frac{\Delta_{vap}H}{R_0} \cdot \frac{1}{T} + C_1 \right\} \quad (3.25)$$

The characteristic of the molar enthalpy of vaporization is approximated by the polynomial in Equation 3.26, which is a polynomial that is being used to approximate the molar enthalpy of vaporization of water.

$$\Delta_{vap}H = C_2 - C_3 \cdot \left(\frac{T}{1000} \right) - C_4 \cdot \left(\frac{T}{1000} \right)^2 \quad (3.26)$$

When those equations are put together, the final fitting equation for the solidification line of argo is Equation 3.27. This equation is fitted on the data that originates from the plot of the book reference [24].

$$p_{Ar,solid}(T) = f_{fit}(T) = \exp \left\{ \frac{C_2 - C_3 \cdot \left(\frac{T}{1000} \right) - C_4 \cdot \left(\frac{T}{1000} \right)^2}{R_0} \cdot \frac{1}{T} + C_1 \right\} \quad (3.27)$$

The result of the corresponding fitting constants is listed here in Table 3.1.

Table 3.1.: Fitting constants for the argon solidification line

Variable	Value
C_1	$-1.31258174E + 3$
C_2	$7.75199007E + 3$
C_3	$1.10847031E + 4$
C_4	$1.63108906E - 1$

With the continuous definition of the solidification line in place, a model option was implemented to expand the gas through the nozzle only until the solidification line was met. The assumption being here that any further effects are having a negligible contribution to the thrust and specific impulse, which turned out not to be the case, as the resulting performance parameter showed less realistic values for F and I_{sp} .

3.3.3. Model Summary

Due to the unavailable information on the internal geometries of the heating elements, a heat model from the operation voltage to the equilibrium gas temperature could not be implemented. Instead, the equilibrium gas temperature is treated as known and used as an input for the nozzle model, so that the performance can be computed for different levels in temperature.

The nozzle model is a simple 1D model for isentropic choked flow conditions. Due to the very high expansion ratio of the XR-100, considerations about the truthfulness of the exit temperature have been raised, as the solidification line for argon is crossed, when an expansion over the full nozzle length is assumed. Attempts have been made to counteract this with an expansion only until the solidification line was met. However, for the estimation of the most important performance variables (\dot{m} , F and I_{sp}), the expansion up to a given exit pressure yielded the most realistic results. For a more correct modelling, near absolute zero temperature effects and near solidification effects on the gas need to be considered.

The structure of the model is illustrated in Equation 3.28 in forward execution.

$$\begin{array}{ccc}
 & & Ma_e \\
 & & V_e \\
 p_c & & p_e \approx p_{back} \\
 T_c & \rightarrow \boxed{\text{model}} \rightarrow & T_e \\
 p_{back} & & \dot{m} \\
 & & F \\
 & & I_{sp}
 \end{array} \quad (3.28)$$

This model will be used to simulate the performance of the thruster over the operating range in inlet pressure (which is assumed to be maintained as chamber pressure) and thruster gas temperature with a fixed expected background pressure. The comparison of the model results to the experimental results is carried out in Section 5.5.

4. Experimental Setup

4.1. Overview of the ESA Propulsion Laboratory

The ESA Propulsion Laboratory (EPL), located on site at the European Space Research and Technology Centre (ESTEC), is the heart of electric propulsion at the European Space Agency (ESA). In this laboratory the entire history of electric propulsion in ESA missions is contained. In the very beginnings cold gas thrusters have been characterised for example for the CryoSat, GOCE or GAIA mission. Also resistojets have been characterised here e.g. for the very first GALILEO satellite. Over the last decades, countless tests over every aspect in electric propulsion have been conducted here: arcjets, cathodes, hall thruster, RIT, FEEP, helicon thruster, colloid thruster, coupling tests, plasma-diagnostics, thrust balance verification, thruster acceptance or qualifications and many more. In order to conduct so many tests with so many different requirements, a vast amount of hardware is needed. The EPL achieves this by having a rich set of vacuum equipment, with multiple vacuum chambers in various sizes, capabilities and pump systems. This is also represented in the measurement and control equipment, which ranges from dozens of power supplies, mass flow controller, pressure transducers, pressure regulators, vacuum gauges or data acquisition systems in any desired range or precision needed to execute tests in up-most precision. Also for thrust balances this laboratory has several implementations with different ranges and resolutions, which can resolve up to pico Newtons of force in the extreme cases. The current facility of the laboratory is shown in Figure 4.1.



Figure 4.1.: The ESA Propulsion Laboratory (EPL) (picture made in 2009) [19]

Next to the experiments conducted from the electric propulsion section (TEC-MPE), the chemical propulsion section (TEC-MPC) and the section of flight vehicles and aerothermodynamics (TEC-MPA) also share this laboratory to conduct their own tests here. As a more recent development, this laboratory is also available to be booked by external companies in electric propulsion, who can test or verify their prototypes here. All together, this laboratory is a very mature and well equipped testing ground with many capabilities for ESA itself and industry.

4.2. ESA EPL process stages

In the EPL a predefined sequence of events and reviews are to be held for any conducted test in the laboratory. Depending on the tests complexity the requirements depend on the assigned so called Service-level (SL). The definition of when which SL shall be assigned can be seen in Table 4.1.

Table 4.1.: Service Level Definition

Service Level	Definition / Applicability
Service Level A	Test items related to actual flight hardware
Service Level B	Qualification of test models used for flight hardware and other equipment
Service Level C	Testing of Engineering Models
Service Level D	Basic Prototype testing, and/or repeatable tests

Consequently all test service activities are set as either required, optional (O) or general process applicable (GP), according to table 4.2.

Table 4.2.: Definition of the SL plan for test activities in the EPL according to [5] (O = optional, GP = general process applicable/ no records required)

Test Services Activities	SL-D	SL-C	SL-B	SL-A
Kick-Off	GP	Required	Required	Required
Planning	GP		Required	Required
Interface meeting	GP	Required	Required	Required
Test Procedure Development	Required	Required	Required	Required
Purchasing/Manufacturing	GP	GP	GP	GP
Integration	GP	GP	GP	GP
Calibration/Validation	O	Required	Required	Required
Pre-test(s)	O	O	O	Required
Test Readiness Review (TRR)	O	O	Required	Required
Test	Required	Required	Required	Required
Post-Test Review (PTR)	O	O	Required	Required
Reporting	Required	Required	Required	Required
Test Review Board (TRB)	O	O	Required	Required

This test is categorised as SL-D, which requires less documentation than higher levels, however more than these necessary steps have been carried out. The test started with a kick-off meeting on the 07.06.2024, after which the test preparation phase has begun and a test logbook was started. The test setup had a major restructuring in between, which resulted in delays in the time schedule. Additionally, non functional pump systems delayed the test preparation phase even further. During the test preparation, all pre-tests and calibration steps are executed, resulting in the execution of most of the as-run procedures in this phase. The ESA internal test plan document [45] is the outcome of these test preparations, which is a very detailed documentation (236 pages) of the test setup, equipment and all procedures. The Test Readiness Review (TRR) occurred on the 28.08.2024, which verified the test plan and authorized the test execution. The primary test execution occurred on the 05.09.2024 where the resistojet was fired. The Post Test Review (PTR) occurred on the 11.09.2024, which verifies the successful acquisition of data and authorizes the venting of the chamber and the disassembly of the test setup. The PTR occurred on the 24.09.2024, where the results are presented and the test is concluded. Finally, the results are documented in the ESA internal test report document [46] (58 pages).

4.3. Test Item Description

4.3.1. Thruster

The test item is the XR100 resistojet made by ALTA SpA in 2011, which is presented in Figure 4.2. ALTA SpA has undergone a corporate fusion into SITAEL in 2015, under which the XR-resistojet family is by the day of writing available as commercial off the shelf (COTS) component. [18]



Figure 4.2.: The XR100 resistojet in the ESA propulsion laboratory

Due to protection of intellectual property of SITAEL, the published information in this thesis is restricted, in particular on the performance and absolute values of the test item. Consequentially, all relevant values are normalized in this thesis, however one reference for the performance of the XR100 model is publicly available in a product sheet published by SITAEL in 2015, which is summarised in Table 4.3.

Table 4.3.: Technical Specifications of the XR100 model in 2015 according to its product sheet [53]

	variable	value	unit
Propellant Type		Ar, Xe, N_2	
Power	P	≤ 80	W
Bus Voltage	U	28	V
Thrust	F	125	mN
Specific Impulse	I_{sp}	63..105	s
Thrust Efficiency	η_T	≤ 60	%
Lifetime	t_{life}	> 200	h
Thruster Mass	m_T	0.220	kg

As visible in Figure 4.2, the Resistojet (RJ) has a 1/8" Swagelok compression fitting connector for the gas inlet, one type-K thermocouple interface for the internal temperature, as well as 4 connectors for the electrical power input. The 4 connectors are due to the presence of two separated heater filaments, which are referred to as heater A and heater B. The standard configuration to drive this thruster is powering both heaters simultaneously from the identical Power Supply Unit (PSU) in an parallel electrical circuit.

4.3.2. Thrust Balance

The thrust balance used in this test is referred to as the "ICL Thrust Balance", due to it being designed and supplied by the Imperial College London. A photo of the balance in the EPL is shown in Figure 4.3.

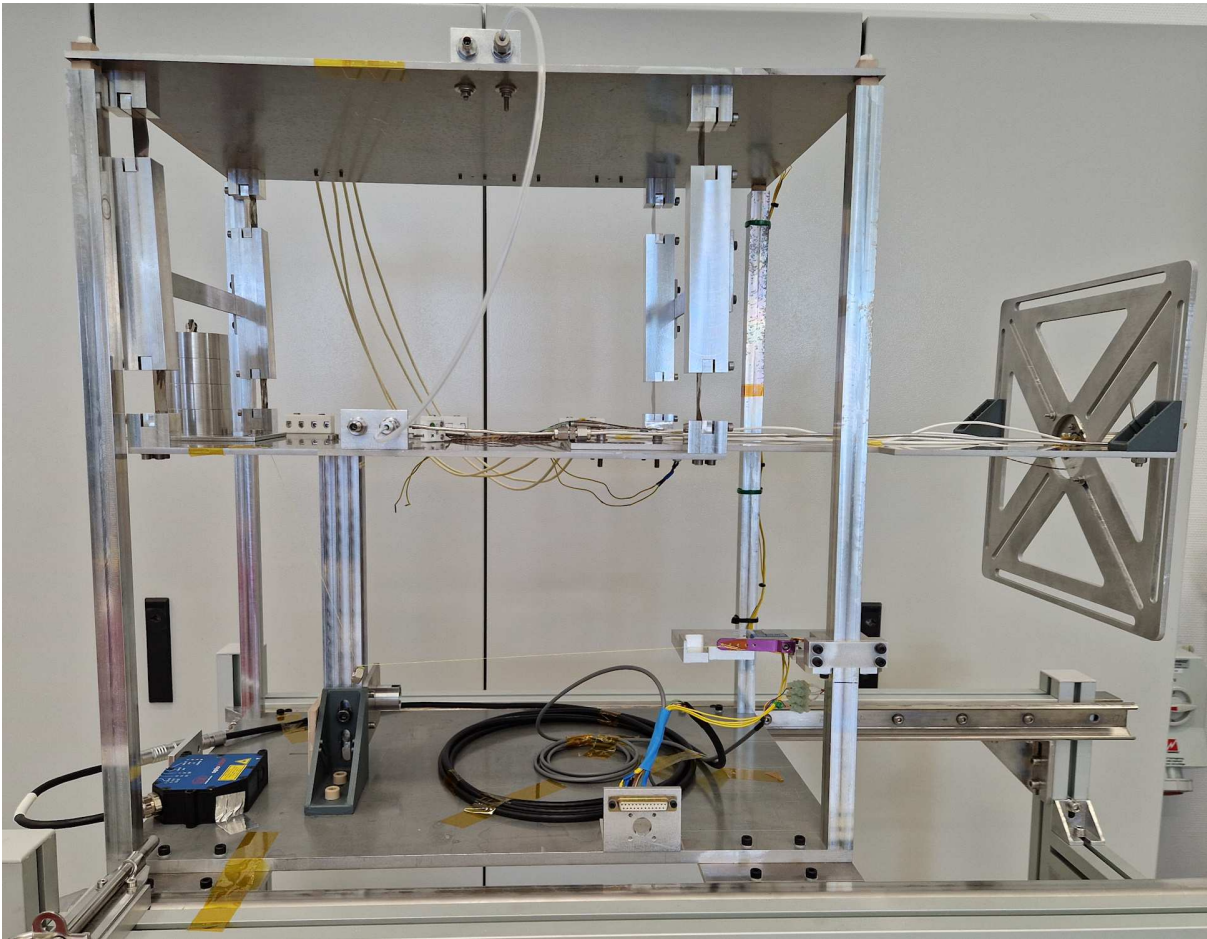


Figure 4.3.: The Imperial College London Thrust Balance in the EPL

This thrust balance is a hanging pendulum implementation, where the thruster is mounted to the movable part. When a force is applied by the thruster, the pendulum experiences a displacement which is measured by a laser. This displacement is then mapped to a force, by a sensitivity factor that was determined in a calibration procedure beforehand. Hereby is the movable part of the balance designed to be as easily disturbed as possible, in order to measure low thrust levels of mN, common in electric propulsion systems. This is achieved by flexures of thin sheet metal that restrict the movement in one axis and create a hinge point with very low dampening while still supporting the weight of the movable part up to 8kg. Due to its undampend characteristics, the pendulum oscillates on its natural frequency, both during no-thrust and during thrust phases. Therefore the thrust signal is "contaminated" with the natural oscillation, when the displacement is measured by the laser. Note that the absolute distance is not of importance and always a relative displacement is being used. The laser is a commercial component (model optoNCDT 1700-10) with a resolution of $0.5 \mu\text{m}$. The calibration is performed via a Voice Coil Actuator (VCA), that is being installed on the balance right before the facility is pumped down to vacuum. This VCA is applying a known force to the balance and the resulting change in distance is recorded. The VCA is characterised

beforehand on a mass balance to identify the relationship between the current applied on the VCA and the exerted force. The balance is supplied with the capability to make a point measurement of thrust, which requires the thruster to be shut off in order to measure this relative displacement. A rendering of the computer-aided design (CAD) model is shown in Figure 4.4, with key elements highlighted.

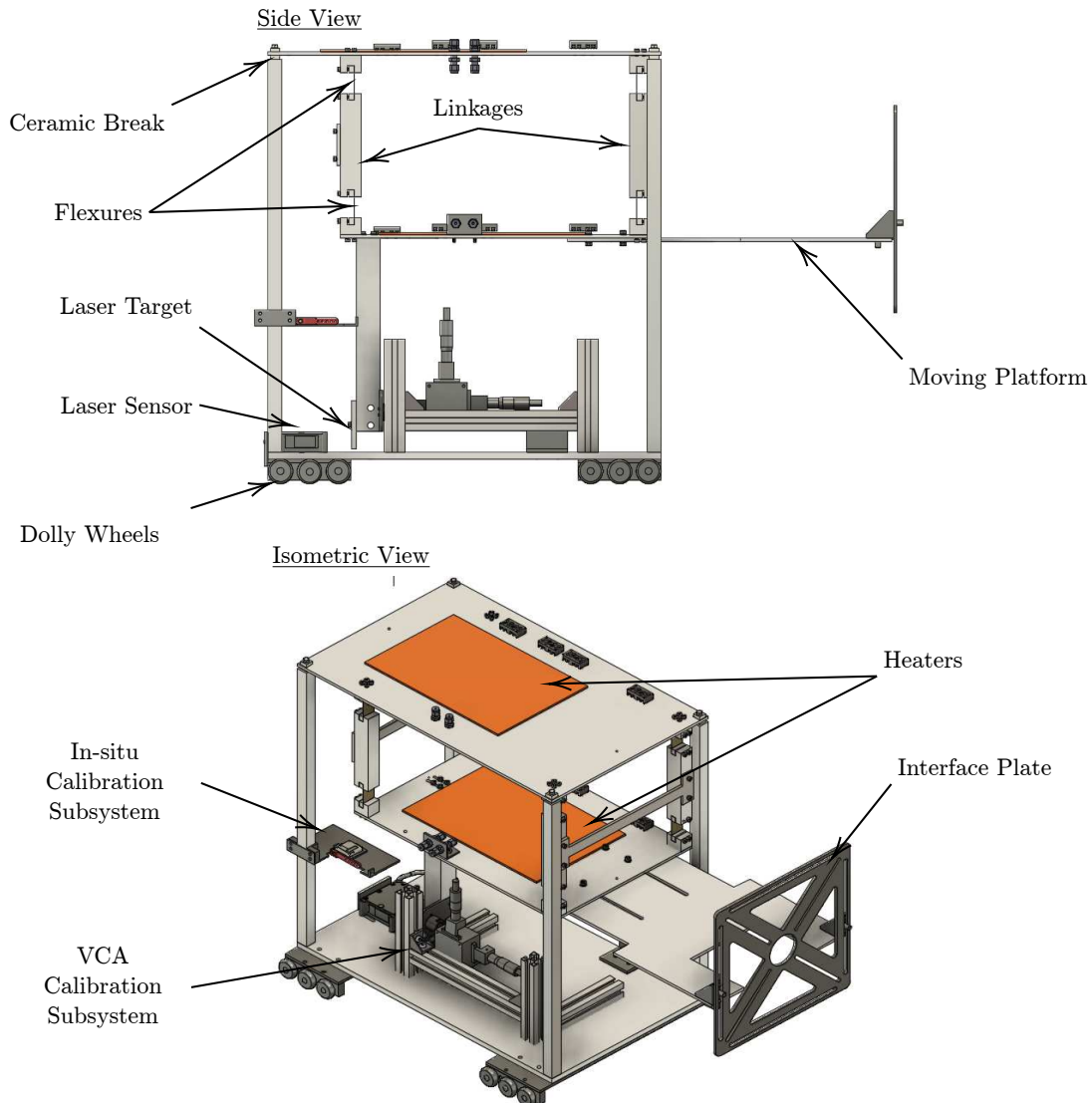


Figure 4.4.: CAD rendering of the Imperial College London Thrust Balance [41]

4.4. Test Objectives

The general objective of this test is the characterisation of the XR100 with the ICL balance, in order to verify functionality of the thruster and achieve operational improvements on the thrust balance. The central point of comparison of the thruster is the *Acceptance Test* of the XR100 [9], which provides a reference in cold flow performance (CFP) and reference in the resistojet performance (RJP). Several operation point (OP)s have been defined being OP1 to OP13, as increments in mass flow during the cold gas mode, and OP14 as nominal resistojet mode (later also referred to as hot flow). The individual test objectives are formulated as pass fail criteria and are listed in Table 4.4.

Table 4.4.: Test Objectives as Pass Fail Criterion

#ID	Title	Criterion Description	Requirement (CFP and RJP from [9])	Method Applied to fulfill the Criterion Description
01	XR100 RJ Thrust	Measure a value of the thrust produced by the RJ for all OPs	A thrust value is successfully recorded for each OP.	The ICL TB's laser output (a displacement value) will be read and converted to a thrust value, using the ICL TB calibration methods.
02	XR100 RJ Thrust Comparison	Compare the measured thrust value to the thrust value in the <i>Acceptance Test</i> for two OPs (CFP and RJP).	The measured thrust value is: CFP: \square mN $\pm 20\%$ RJP: \square mN $\pm 20\%$	The thrust value produced by the RJ will be determined for CFP (OP13) and RJP (OP14). and then compared to the results from the <i>Acceptance Test</i> .
03	XR100 RJ Thrust Uncertainty Budget	Perform an uncertainty budget of the measured thrust value.	An uncertainty budget is successfully computed for the recorded thrust values.	An uncertainty budget of the measured thrust values will be performed by following the procedure used in [6].
04	XR100 RJ Mass Flow	Read and set a mass flow to the RJ for all OPs	A mass flow is successfully set and recorded.	For every OP, a value of the RJ's inlet mass flow will be set and read by a software used to set and read the Mass Flow Controller (MFC).
05	XR100 RJ Mass Flow Comparison	Compare the measured mass flow value to the mass flow value in the <i>Acceptance Test</i> for two OPs (CFP and RJP).	The measured mass flow value is: CFP: \square mg/s Ar $\pm 20\%$ RJP: \square mg/s Ar $\pm 20\%$	A value of the RJ's inlet mass flow will be measured for two OPs, CFP (OP13) and RJP (OP14), and then compared to the results from the <i>Acceptance Test</i> .
06	XR100 RJ Mass Flow Uncertainty Budget	Perform an uncertainty budget of the mass flow measurement values.	A mass flow measurement uncertainty budget is successfully computed	A mass flow UBC will be performed according to the procedure in [38].

07	XR100 RJ Isp	Compute a value of the Isp produced by the RJ for two OPs (CFP and RJP).	A value for Isp is successfully computed.	An Isp of the RJ will be computed of each mode (CFP and RJP) by using a value of the RJ's read inlet mass flow (measured with the MFC) and a value of the RJ's read thrust (measured with the ICL TB). The Isp is computed with the following formula: $I_{sp} = \frac{F}{\dot{m} \cdot g_0}$
08	XR100 RJ Isp Comparison	Compare the computed Isp to the Isp from the <i>Acceptance Test</i> for two OPs (CFP and RJP).	An Isp is recorded for: CFP: [] s $\pm 20\%$ RJP: [] s $\pm 20\%$	A value of the RJ's Isp, measured for two OPs, CFP (OP13) and RJP (OP14) will be compared to the results from the <i>Acceptance Test</i> .
09	XR100 RJ Power	Set the voltage at which the RJ is running, for two modes (CFP and RJP).	The set voltage is: CFP: 0 V RJP: 28 V	The power to the RJ will be indirectly set by the voltage.
10	XR100 RJ Power Comparison	Compare the read power for two modes (CFP and RJP), to the ones stated in the <i>Acceptance Test</i> .	The read power is: CFP: 0 W RJP: [] W $\pm 20\%$	The power (which was set by volage) will be read by the current according to OP14, using a PSU connected to the RJ's internal heaters. The power is derived from the voltage and current accordingly: $P = U \cdot I$
11	XR100 RJ Pressure	Set the inlet pressure to the RJ as the same as applied in the <i>Acceptance Test</i> for two OPs (CFP and RJP).	The set RJ inlet pressure is: CFP: [] bar (a) $\pm 5\%$ RJP: [] bar (a) $\pm 5\%$	The RJ's inlet pressure will be set by a pressure regulator on the argon bottle.

12	XR100 RJ Pressure Comparison	Read the inlet pressure to the RJ and compare it to the <i>Acceptance Test</i> for two OPs (CFP and RJP).	The read RJ inlet pressure is: CFP: [] bar (a) $\pm 5\%$ RJP: [] bar (a) $\pm 5\%$	The inlet pressure will be read by a Pressure Transducer (PT) placed on the feeding line, reading the MFC's outlet pressure. (When the MFC restricts the flow, the inlet pressure is different from the set pressure before the MFC.)
13	XR100 RJ Temperature	Read the temperature of the RJ.	A temperature of the RJ is successfully acquired.	The temperature of the RJ will be read by one Thermocouple (TC) (TC1), placed inside the RJ.
14	Interface Temperature	Read the temperature of the interface the RJ is mounted on	A temperature of the RJ's interface is successfully acquired.	The temperature of the interface plate where the RJ is mounted is measured by a TC (TC4).
15	Flexure Temperature	Read the temperature near the flexure of the balance	A temperature of a flexure is successfully acquired.	The temperature of the metal block which holds the flexures is measured by a TC (TC3). Verify that the temperature here does not thermally drift higher than the requirement.
16	SPF Gas Temperature	Read the temperature of the gas inside the Vacuum Facility (VF) .	A temperature of the RJ's chamber gas is successfully acquired.	The temperature of the gas inside the VF will be measured by a TC (TC2) placed freely hanging above the thruster inside the VF, mounted to the steady part of the balance from an outwards extending pipe.

17	SPF Vacuum Pressure	Read the ultimate pressure and the background pressure in the VF for the two OPs that was used in the <i>Acceptance Test</i> (CFP and RJP).	<p>The background pressure is: CFP: [] mbar N2 ±50% RJP: [] mbar N2 ±50%</p> <p>However, higher pressures are expected, as a weaker Primary Pump (PP) combination (PP7 and PP8) is used.</p> <p>For the ultimate pressure, no reference is found.</p>	<p>The background pressure will be measured in the hatch and in the main chamber. In both of them two different models (TTR91 and ITR90) are used for acquisition, resulting in 4 Vacuum Gauge (VG)s in total. These two models have different accuracies at different operating ranges, meaning that when the RJ is firing and the turbopump is off, one VG is appropriate (TTR91), but while the turbopump is on and lower pressures are reached, the other model (ITR90) provides a more accurate reading. Before the test starts, the ultimate pressure will be recorded by these VGs.</p>
18	SPF Pumping Speed	Compute the pumping speed of the used pumps of the VF and compare it to what is specified on the pump's datasheet.	<p>The pumping speed is: for PP7 & PP8 (together): 111 L/s (air)</p>	<p>The pumping speed of the VF will be computed by reading the ultimate pressure and the background pressure in the VF, the temperature inside the VF and the inlet mass flow to the RJ when the RJ power is off and when the RJ power is on, which should result in a different gas temperature</p>

4.5. Test Facility

The vacuum facility used in this test is the Small Plasma Facility (SPF), which is the second biggest vacuum chamber standing in the EPL. This facility was also used for the *Acceptance Test* of the XR100 in the EPL. The facility is split into the main chamber and the so called hatch, where the thrust balance will be located. The dimensions are $3.35m \times \varnothing 2m$ for the main chamber and $1m \times \varnothing 1m$ for the hatch. This facility is one of the main EPL chambers that is running in daily business and has a booked out calendar for planned tests. The SPF has installed a great number of pump systems, which are being a turbo pump with a primary pump backing in each section, two additional primary pump systems, one two-staged cryo pump, 4 cryo heads and a liquid nitrogen cooled target. A schematics of the facilities is shown in Figure 4.6. Its lowest achievable pressure is around 10^{-7} mbar with a theoretical pumping speed of 128000 L/s of Nitrogen in nominal test conditions [17]. These pressure levels however can only be maintained with a very low mass flow, which will not be the case in this test. As the expected pressures during this test are too high for the cryo pumps or even the Turbo Pump (TP), this test will run on primary pumps only. During the test preparations, the primary pump system (PP5 and PP6) and the turbo pumps (TP1 and TP2) with their backing pumps have been used to leak detect the entire vacuum facility. During the thruster firing, the replacement primary pump system (PP7 and PP8), which can be seen in Figure 4.5, was used due to multiple repairs on the other initially planned primary pumps. This replacement system has a lower pumping speed than the primary pumps used during the *Acceptance Test* of the XR100, which is why higher background pressures are expected during firing.



Figure 4.5.: Primary pumps on the SPF used in this test (PP5,PP6 and PP7,PP8)

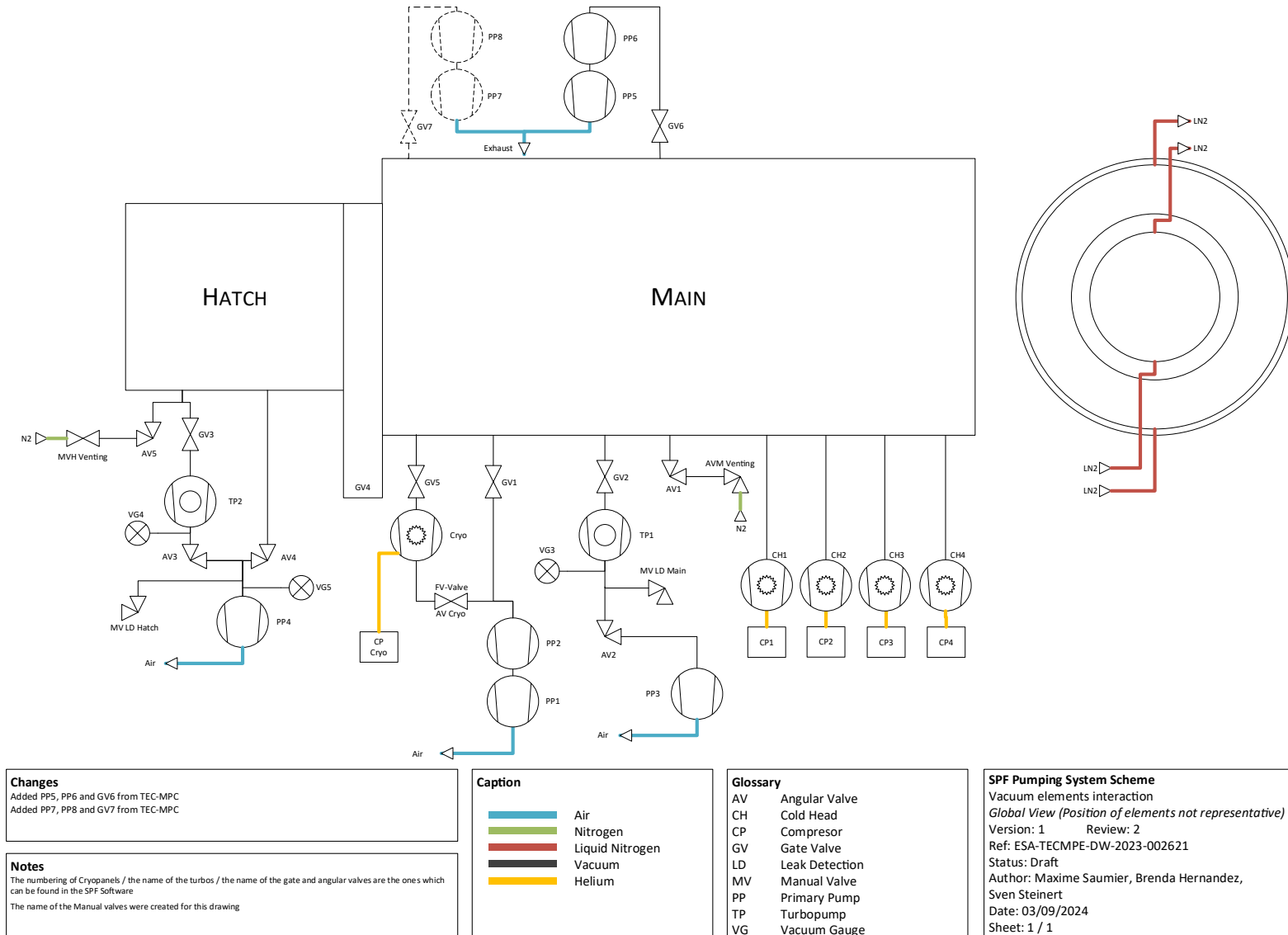


Figure 4.6.: Schematics of the Small Plasma Facility (SPF) Vacuum Facility

4.6. Test Setup

4.6.1. Physical



Figure 4.7.: Front view of the entire test setup

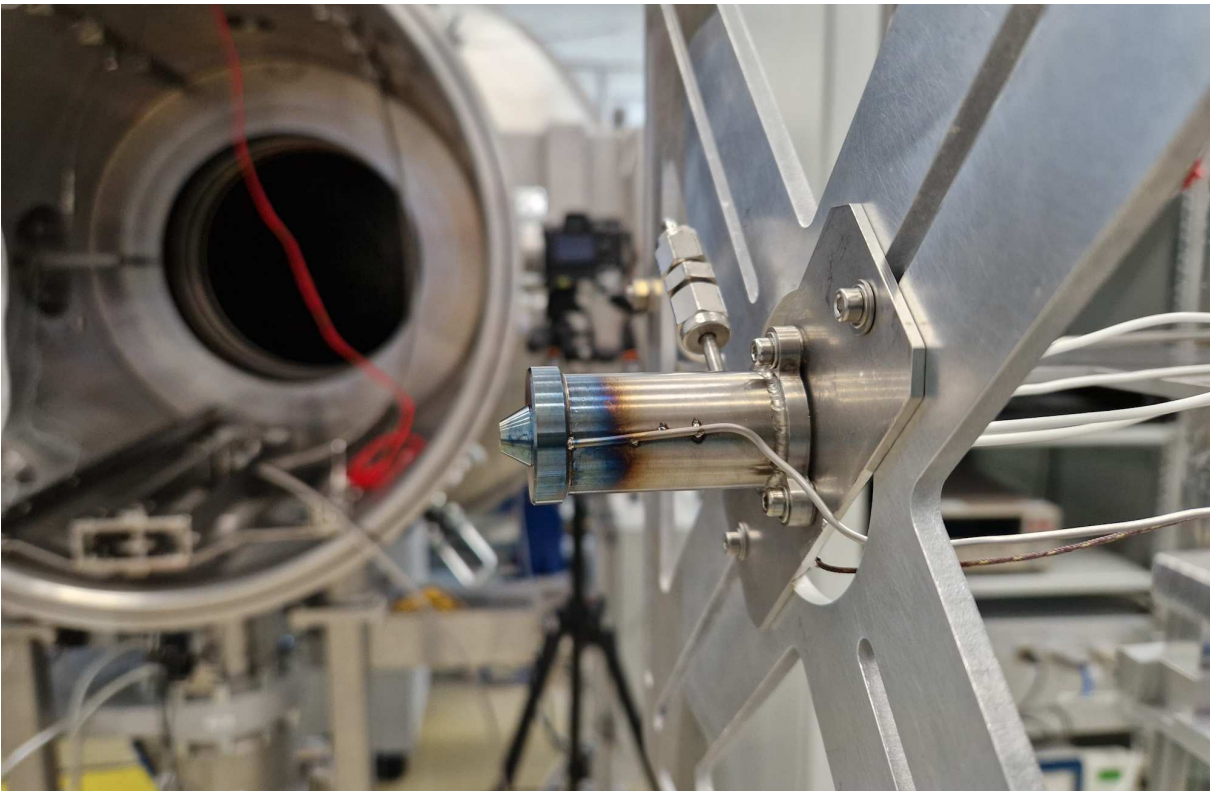


Figure 4.8.: XR100 mounted to the Imperial College London thrust balance

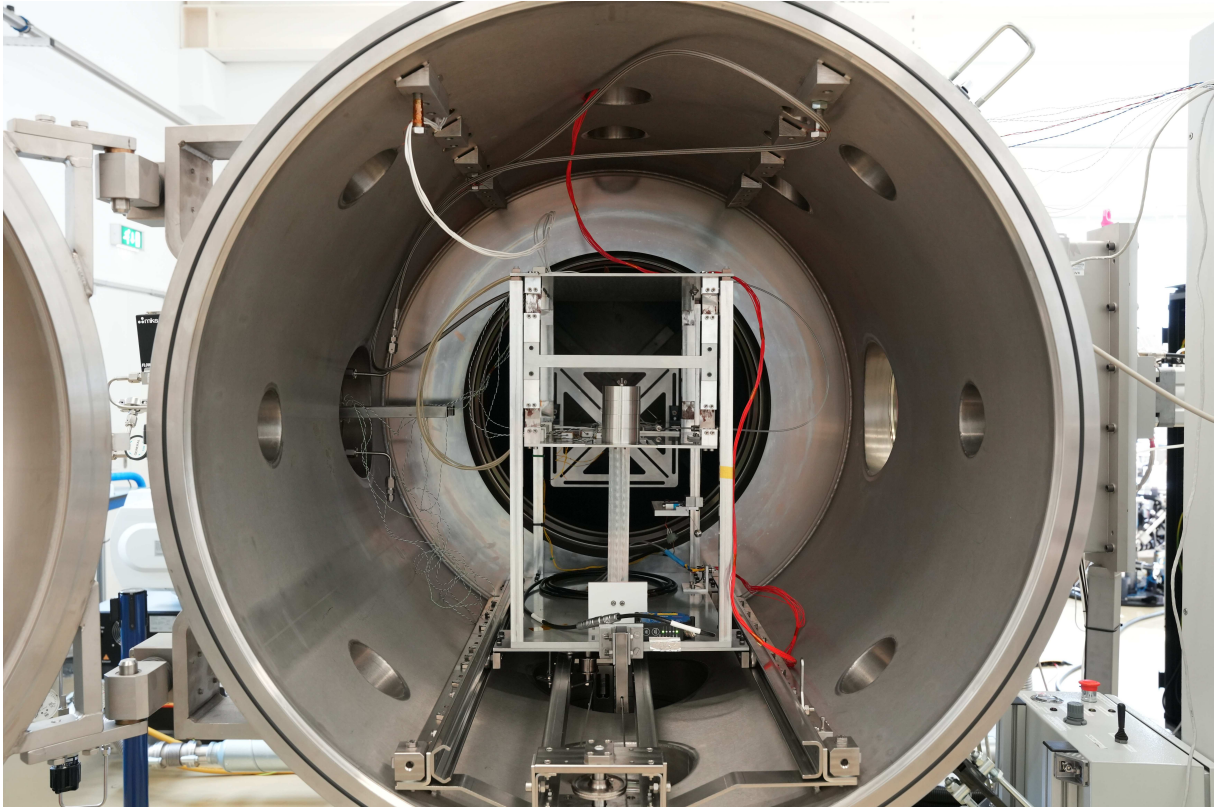


Figure 4.9.: Front view of the test setup inside the vacuum facility

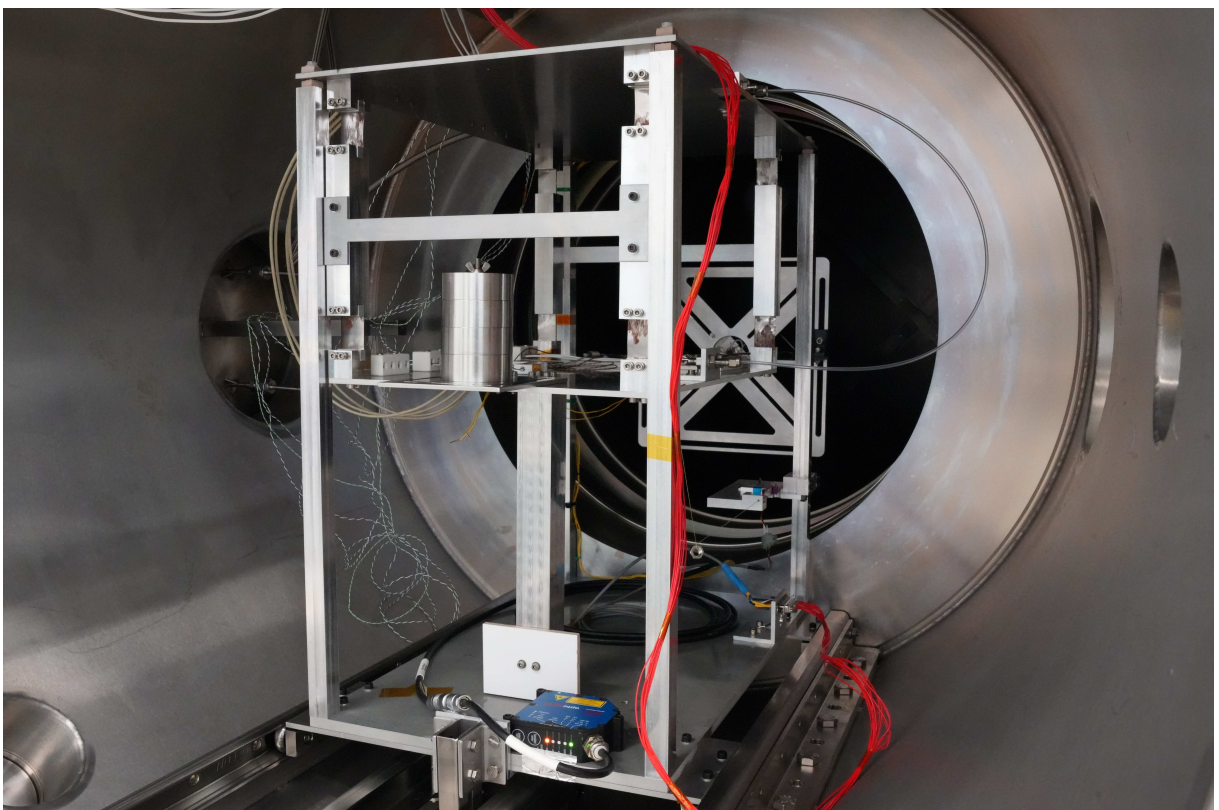


Figure 4.10.: Right view of the test setup inside the vacuum facility

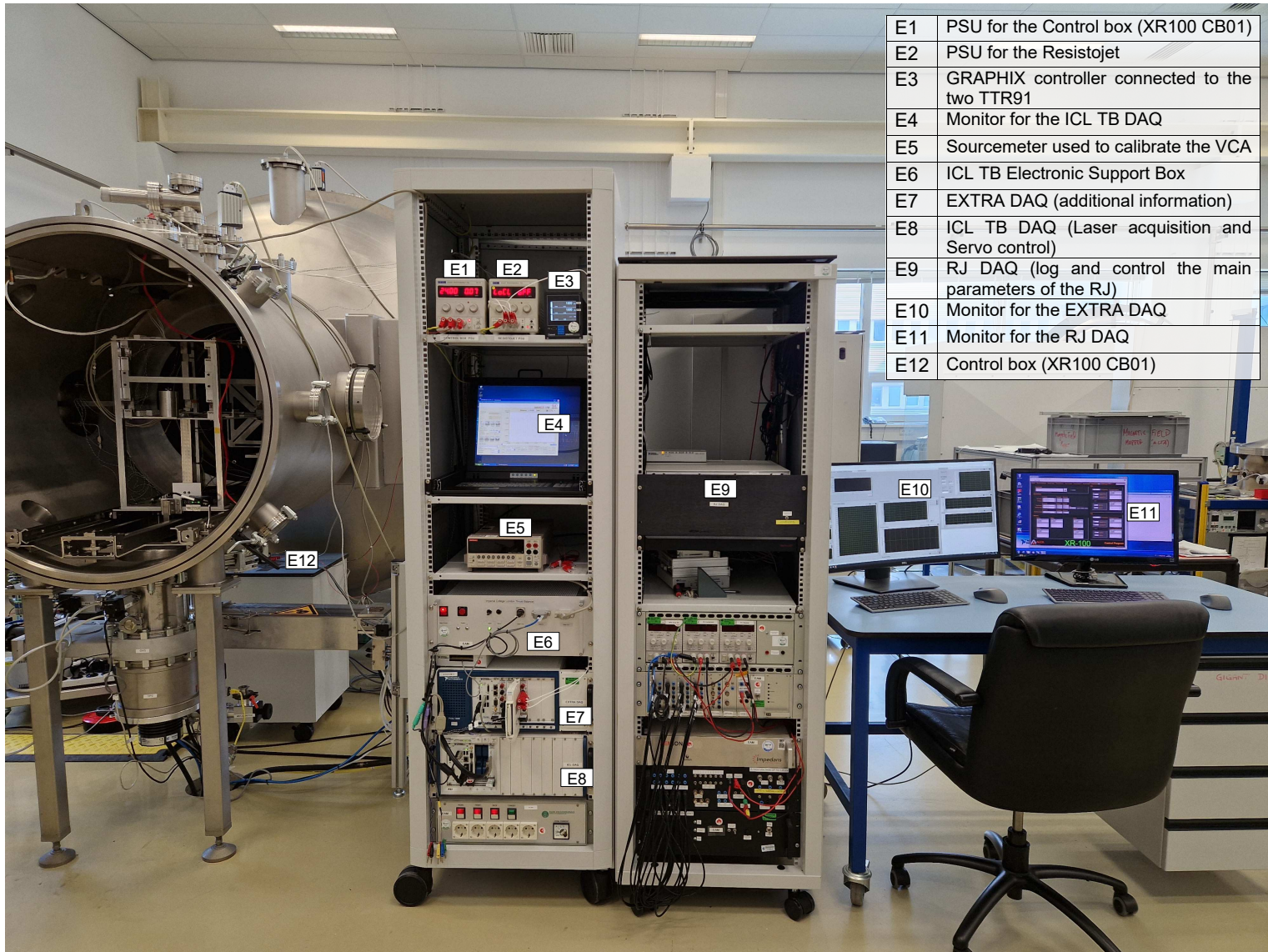


Figure 4.11.: Main view of the test setup with key components marked



E13	Monitor for the SPF DAQ
E14	CENTER controller connected to the two ITR90
E15	SPF DAQ (facility pump control)

Figure 4.12.: Side view of the test setup with key components marked

4.6.2. Data Acquisition and Software

The data acquisition (DAQ) is spread over three separate units, that each record a set of variables with their own software. These systems are National Instrument computers which can be expanded by modules to suit any given test setup. These proprietary National Instrument systems with all expansion cards are operated and programmed via their associated LabVIEW software.

Resistojet DAQ The first DAQ is the resistojet DAQ, which is assembled by the components that are used in the user manual [36] and the acceptance test of the thruster [9]. This assembled hardware can be seen in Figure 4.13. ALTA did also provide a corresponding LabVIEW software with which the thruster is operated and tracked. This software came with the restriction that nothing could be edited, as it was pre-compiled. This has the consequence, that if any additional variables are planned to be recorded, an additional DAQ is required. The parameters that can be recorded with the XR100 control software are: the mass flow (MFC), the inlet pressure (PT2), the resistojets total power consumption (RJ glsPSU), the thruster temperature (TC1) and the interface temperature (TC4).

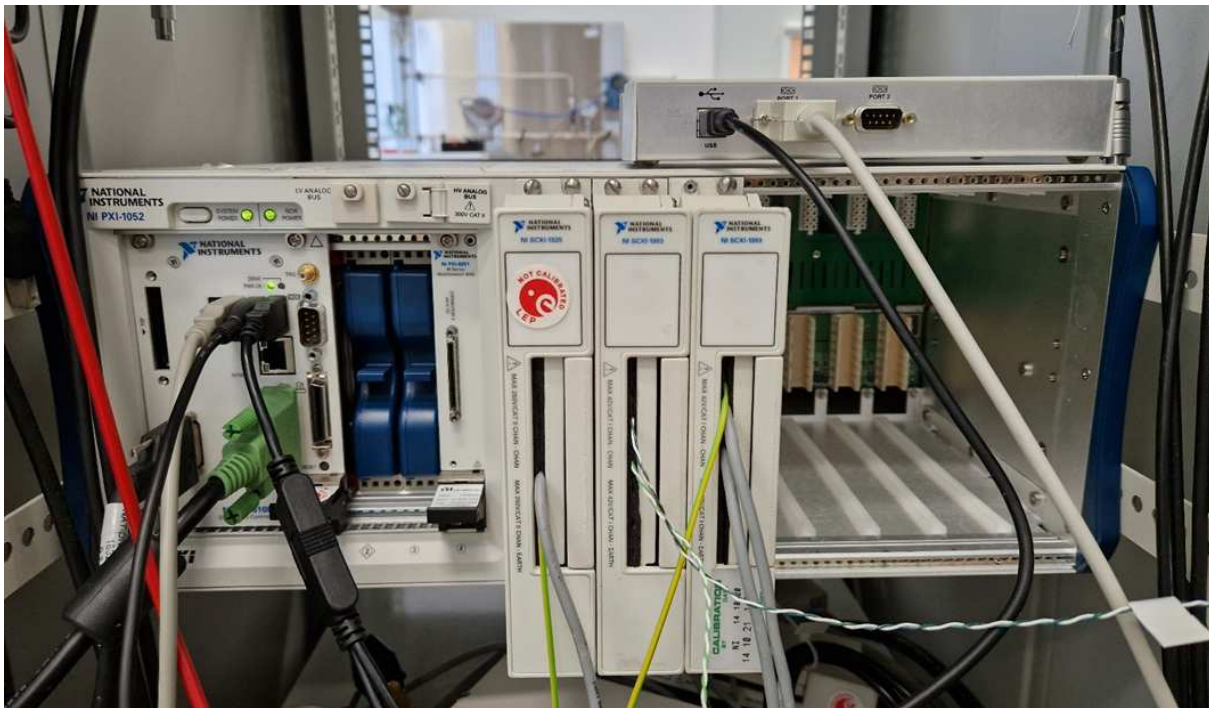


Figure 4.13.: Resistojet data acquisition system (RJ DAQ)

EXTRA DAQ The EXTRA DAQ is the solution to track any extra variables for this test. Those are being all the four vacuum gauges, two additional thermocouples (TC2 and TC3), one additional pressure transducer (PT1) and the current through one of the heaters (heater A). Note that for this DAQ no restrictions of older hardware was given, which leads to this DAQ being built from a more modern architecture, which can measure for example the thermocouple signal with a substantial increased precision. The LabVIEW software on this DAQ was self-developed.



Figure 4.14.: Extra data acquisition system (EXTRA DAQ)

ICL DAQ The DAQ for the ICL thrust balance consists of most parts that are bound to the balance, as e.g. the electronic support box, and was delivered with multiple small softwares for each of its tasks. The acquisition of the laser distance data is done via a standalone application from the sensor manufacturer. For the servo control (used during the In-situ calibration) a LabVIEW software was supplied. In order to also automate the cross calibration, an additional LabVIEW software was self-developed to control the sourcemeter in a predefined pattern. The assembly of the ICL DAQ is pictured in Figure 4.15.

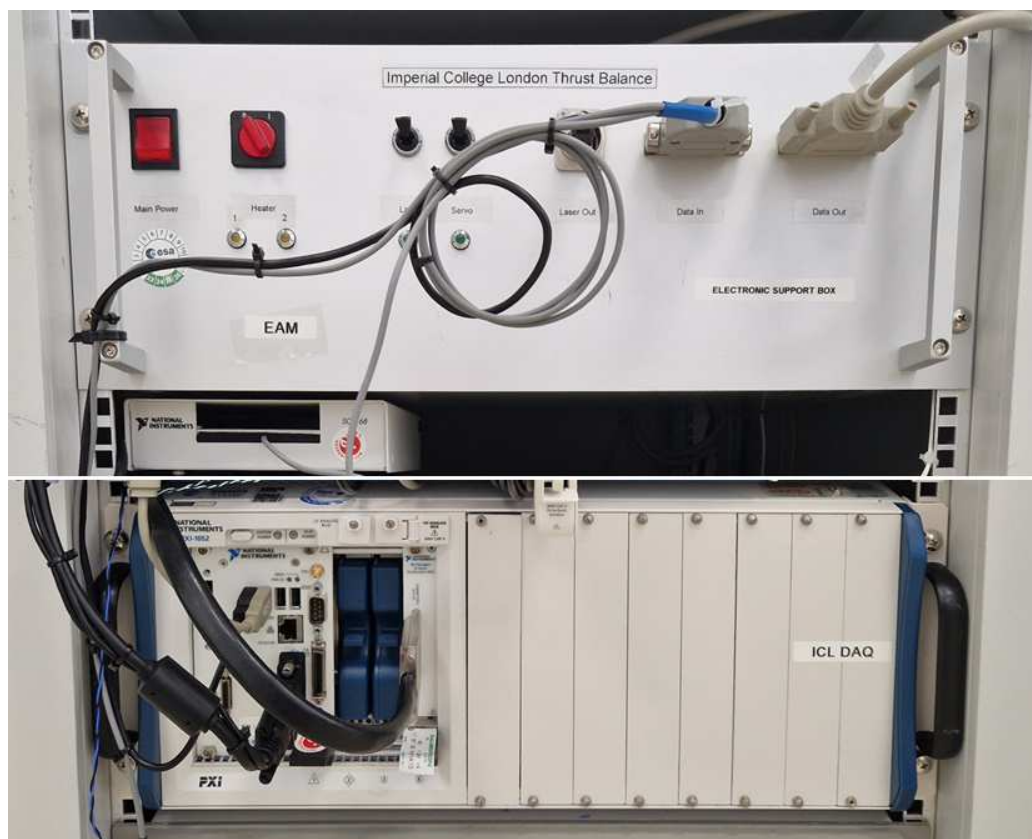


Figure 4.15.: ICL thrust balance data acquisition system (ICL DAQ)

4.6.3. Electrical

The electrical wiring is separated here into three nets, one for each of the data acquisition systems.

RJ DAQ The first net is from the resistojet DAQ (RJ DAQ), which is laid out in Figure 4.16. It connects the main pieces for the resistojet, as the MFC, the PSU and the inlet pressure from the second pressure transducer (PT2). The original electrical connection did only record the total current of both heaters together, however this was modified on purpose to gain insight on each heater currents individually. This was achieved by tapping into one of the power lines of the resistojet with an ammeter which is controlled by the EXTRA DAQ.

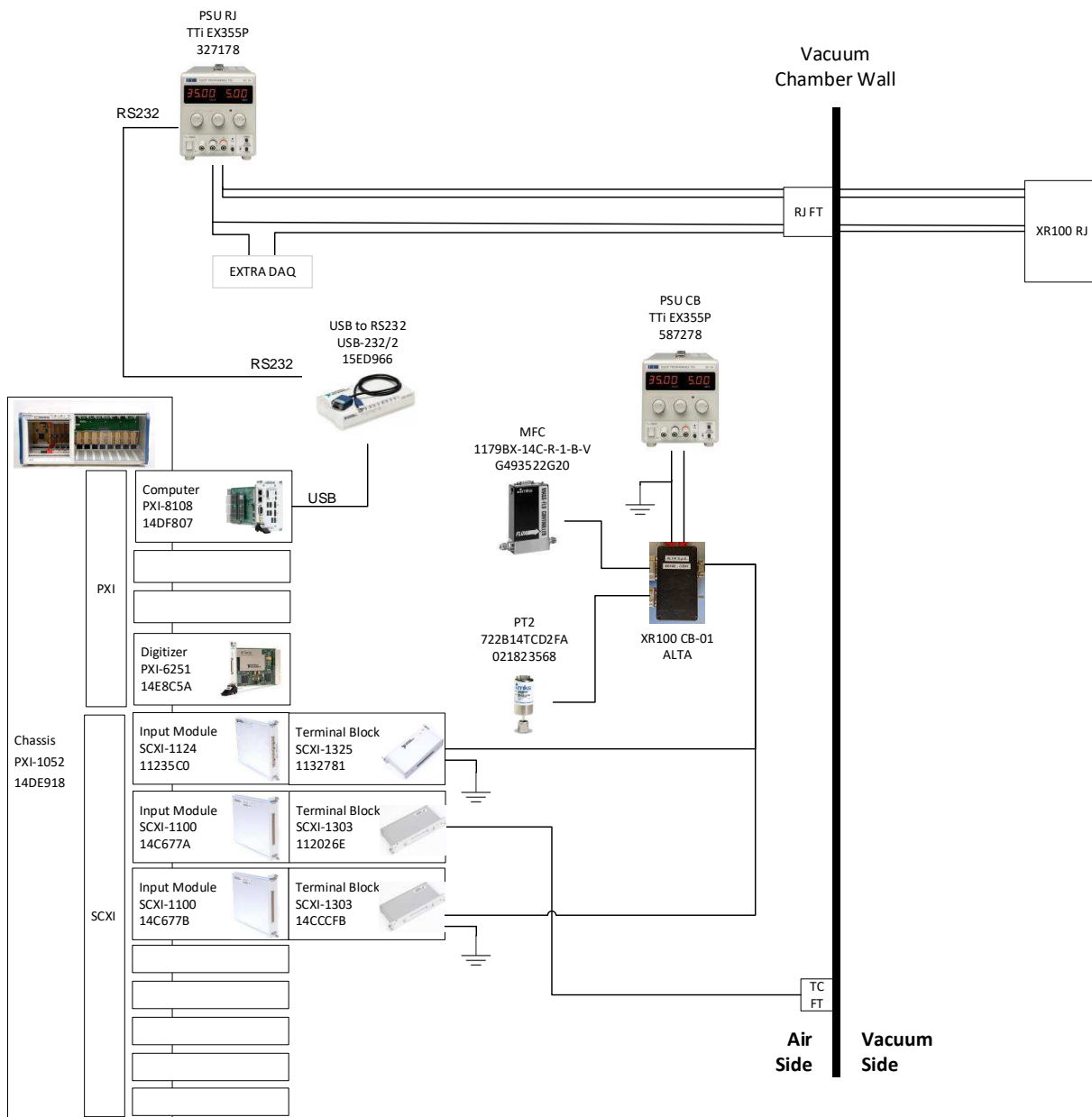


Figure 4.16.: Electrical wiring of the RJ DAQ

EXTRA DAQ The second net is from the EXTRA DAQ, which connects to all vacuum gauges and the first pressure transducer (PT1) that measures the pressure before the MFC. Additionally, the tap-in current measurement to one of the resistojets heaters is shown here. Hereby is a current divider utilised, as the maximum expected current could exceed the maximum current allowed by the multimeter. The current divider was realised by a simple bypass of the same cable that normally carries the current, which results in only a tiny fraction of the current to flow through the multimeter. The fraction by how much the current is divided depends on the two used resistances (the internal resistance of the multimeter, and the resistance of the bypass cable) and was characterised beforehand with the sourcemeter, which yielded accurate and reproducible results.

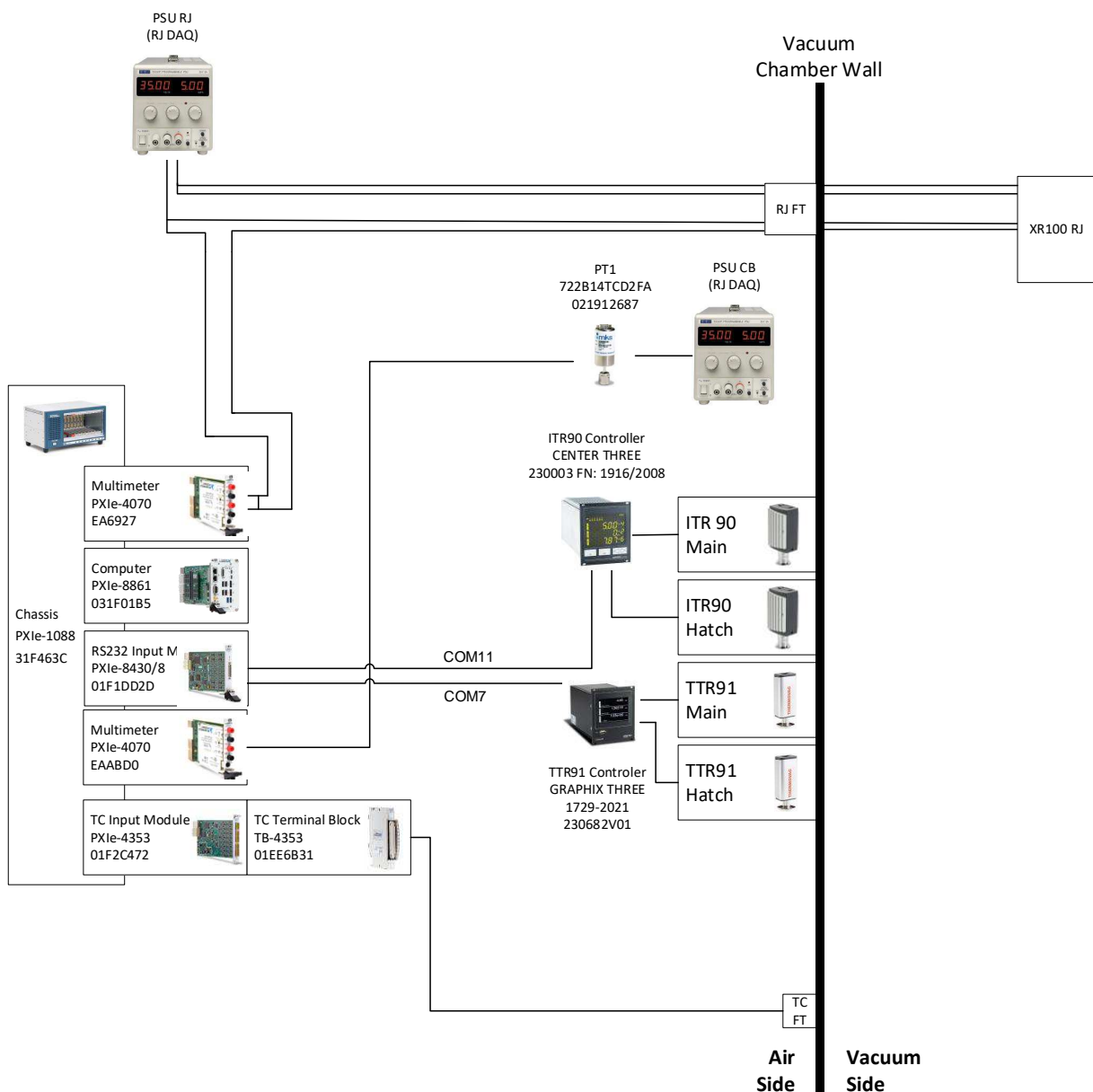


Figure 4.17.: Electrical wiring of the EXTRA DAQ

4. Experimental Setup

ICL DAQ The third net is from the ICL DAQ, which connects to the sourcemeter (drives the VCA during cross calibration) and the electronic support box (ESB), which controls the laser distance sensor, and the servo.

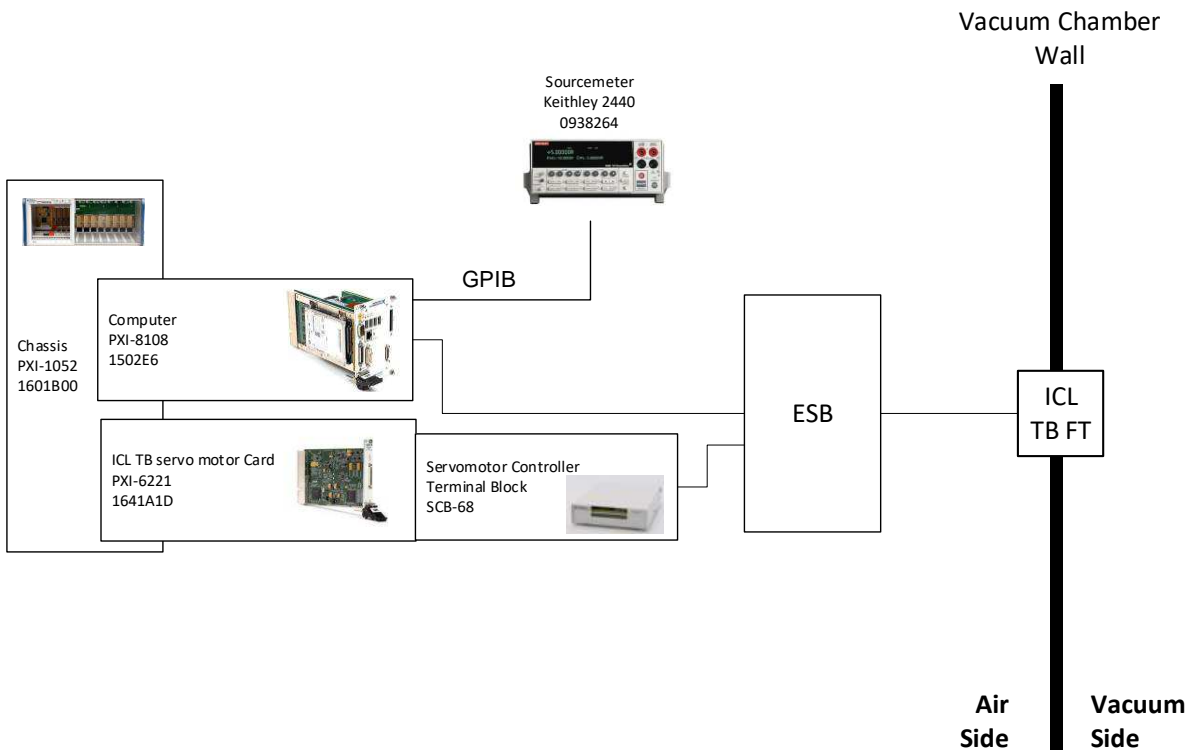


Figure 4.18.: Electrical wiring of the ICL DAQ

Many vacuum ports had to be modified for this test, where one is shown here for reference in Figure 4.19.

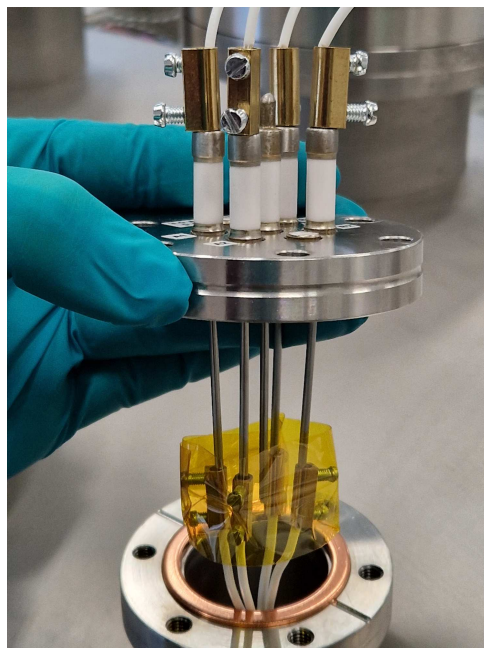


Figure 4.19.: Vacuum feedthrough of the electrical power connections to the resistojet

4.6.4. Thermocouples

In this test are four thermocouples utilised to quantify different thermal aspects. The first thermocouple (TC1) is contained within the thruster unit and gives information of the conditions inside the thruster. The second thermocouple (TC2) is mounted on an extended rod that hangs freely into the vacuum chamber to measure the SPF gas temperature. The third thermocouple (TC3) is mounted on the block that holds the flexures of the thrust balance, in order to capture if thermal drift could be present. The fourth thermocouple (TC4) is mounted on the back of the interface plate of the thruster unit, hereby has this temperature a maximum that shall not be exceeded, according to the user manual of the thrust unit [36]. All thermocouples, except internal one (TC1), are made with type-K "OMEGA cement-on" fast response surface thermocouples that have a welded tip. The four mentioned thermocouples are shown in Figure 4.20 on their mounting location, covered with aluminium tape for better heat conduction.

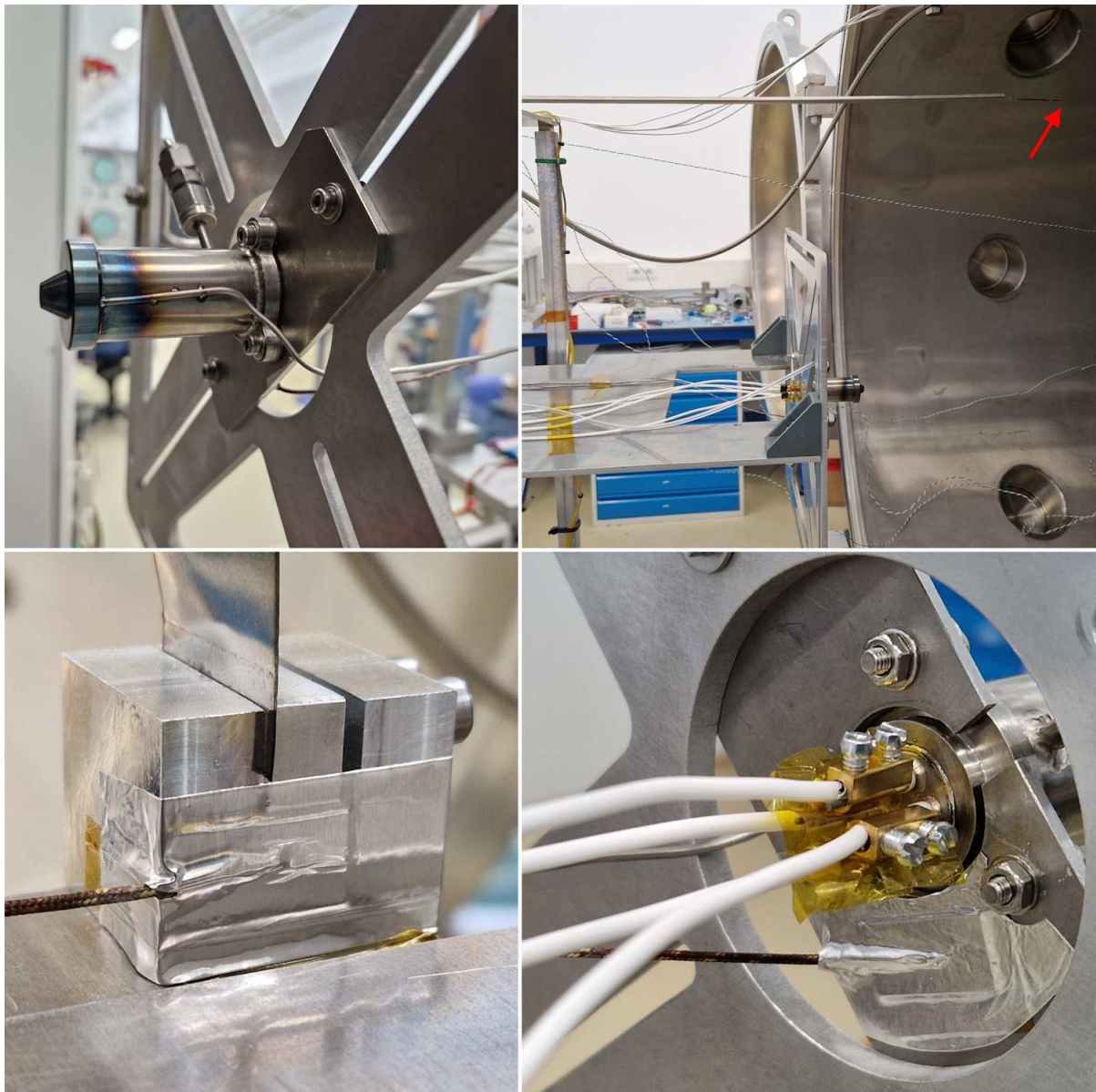


Figure 4.20.: Location of thermocouples: TC1 thruster internal (top left), TC2 SPF gas temperature (top right), TC3 balance flexure block (bottom left) and TC4 thruster interface plate (bottom right)

4.6.5. Fluidic

The fluidic components in are shown in their assembled feeding line in Figure 4.21.

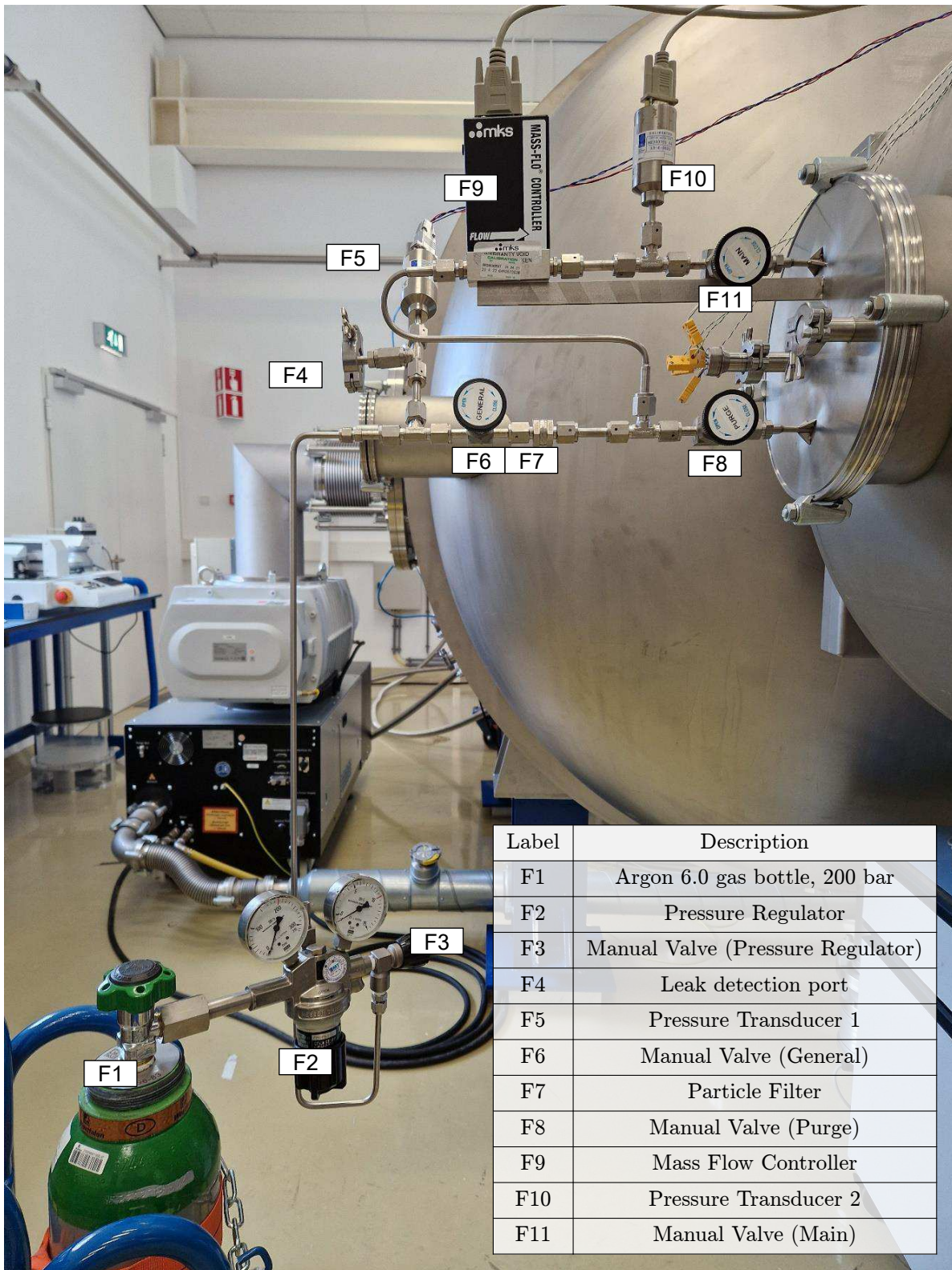


Figure 4.21.: Fluidic setup marked with key components

4.7. Measurement Equipment and Calibration

The selection and integration of all the necessary hardware was a great subject during the test preparations, where in this chapter the resulting list of used equipment is provided. All relevant measurement equipment is undergoing a regular calibration schedule in the EPL. However, despite best efforts, multiple of the used parts have been over their due date in calibration. This is a sensitive aspect, especially when those sensors are used for uncertainty calculations and the results are of major importance. For this test this turned out not to be an issue, as the most important components for the uncertainty calculation, the sourcemeter, the MFC and the mass balance have a valid calibration.

4.7.1. Electrical

The electrical measurement equipment is listed in a tabular form in Table 4.5.

4.7.2. Physical

The physical measurement equipment is listed in a tabular form in Table 4.6.

Table 4.5.: Electrical Measurement Equipment

Requirement	Range	Resolution and Uncertainty	Manufacturer	Model Number	Calibration Due Date	NEN3140 Due Date
PSU for CB01 (MFC and PT) 30V 0.3A	0-35 V 0-5 A	Resolutions: 10mV; 10mA Voltage: 0.3% RD \pm 1 digit Current: 0.6% RD \pm 1 digit	TTi	EX355P	not calibrated (new item)	01.07.2028
PSU for the RJ 30V 4A	0-35 V 0-5 A	Resolutions: 10mV; 10mA Voltage: 0.3% RD \pm 1 digit Current: 0.6% RD \pm 1 digit	TTi	EX355P	02.11.2024	01.05.2027
RJ DAQ chassis 2 PXI and 3 SCXI slots	4 PXI 8 SCXI	-	NI	PXI-1052	-	01.09.2025
RJ DAQ Computer embedded controller CPU	-	-	NI	PXI-8108 (PXIMod1)	-	-
RJ DAQ Chassis communicator to digitize SCXI cards (Multifunction DAQ)	-	Gain Error: 60-150 ppm RD Offset Error: 20-150 ppm FS	NI	PXI-6251 (PXIMod4)	10.03.2025	-
RJ DAQ Input Module to set the MFC setpoint 1 channel, 0-5V	12 bit 0 - 10V \pm 5mA	Voltage: 0.05% FS Current: \pm 0.1% FS	NI	SCXI-1124 (SC1Mod1)	11.04.2024	-
RJ DAQ Terminal Block to set the MFC setpoint	-	-	NI	SCXI-1325 (SC1Mod1)	-	-
RJ DAQ Input Module to read the TCs 2 Channel	32 Channel \pm 100mV 10kHz filter	Gain Error: 0.1% RD Offset Error: 100 μ V	NI	SCXI-1100 (SC1Mod2)	22.03.2024	-

RJ DAQ Terminal Block to read the TCs 2 Channel	Thermistor cold junction	0.5 °C from 15 to 35 °C 0.9 °C from 0 to 15 °C 0.9 °C from 35 to 55 °C Not calibrated as chain	NI	SCXI-1303 (SC1Mod2)	13.10.2021	-
RJ DAQ Input Module to read the MFC and PT	32 Channel ±10V 10kHz filter	Gain Error: 0.04% RD Offset Error: 600 μV	NI	SCXI-1100 (SC1Mod3)	15.10.2021	-
RJ DAQ Terminal Block to read the MFC and PT 2 Channel	32 Channel	-	NI	SCXI-1303 (SC1Mod3)	14.10.2021	-
RJ DAQ USB to RS232 interface	2 Channel	-	NI	USB-232/2	-	-
ITR90 Controller 2 Channel	16 bit 3 Channel	Gain error: ≤ 0.005 % FS Offset error: ≤ 0.01 % FS	Leybold	CENTER THREE	-	01.06.2028
TTR91 Controller 2 Channel	16 bit 3 Channel	Gain error ≤ 0.02 % FS Offset error ≤ 0.05 % FS	Leybold	GRAPHIX THREE	-	01.06.2028
EXTRA DAQ Chassis	-	-	NI	PXIe-1088	-	01.09.2025
EXTRA DAQ Computer Embedded controller	-	-	NI	PXIe-8861	-	-
EXTRA DAQ RS232 Serial Interface Card 2 Channel	8 Channel	-	NI	PXI-8430/8	-	-
EXTRA DAQ Digital Multimeter Read PT1 voltage	1 Channel 6½ digits (10 μV)	26 ppm of reading + 7 ppm of range	NI	PXI-4070	22.09.2023	-

EXTRA DAQ Digital Multimeter Read Heater A partial current	1 Channel 6½ digits	50 ppm of reading + 5 ppm of range	NI	PXI-4070	22.09.2023	-
EXTRA DAQ TC Terminal Block 2 Channel, Type K	32-Channel, 24-Bit -100 – 1400°C	see input module for uncertainty	NI	PXIe-4353 TB	12.11.2021	-
EXTRA DAQ TC Input module	-100 – 1400°C	When paired with PXIe-4353 TB, for K-type TC measuring between 0-300°C, Uncertainty: 0.38°C Not calibrated as chain	NI	PXIe-4353	29.11.2023	-
SPF DAQ chassis	-	-	NI	PXIe-1088	-	01.09.2025
SPF DAQ computer Embedded controller	-	-	NI	PXIe-8861	-	-
ICL DAQ computer Embedded controller	-	-	NI	PXI-8108	-	-
ICL DAQ Chassis	-	-	NI	PXI-1052	-	01.05.2027
ICL DAQ Command of servomotor PWM signal	±10 V	At full scale 3.23µV	NI	PXI-6221	17.07.2020	-
Servomotor Controller Terminal Block	-	-	NI	SCB-68	-	-
PSU for the ICL TB VCA Characterization (Sourcemeater)	0-42V 0-5.25A	(Error ± Uncertainty) (Range) (0.0 ± 1.4) (200mV) (0.0 ± 0.24) mV (40V) (0.0 ± 0.5) nA (10µA)	Keithley	2440	09.11.2024	06.01.2028

Table 4.6.: Physical Measurement Equipment

Requirement	Range	Resolution and Uncertainty	Manufacturer	Model Number	Calibration Due Date	NEN3140 Due Date
MFC for Argon to RJ (from ALTA) expected mass flow X mg/s Ar at expected pressure X bar	10000 sccm N2 at 1 bar(a)	analog signal $\pm(0.5\% \text{ RD} + 0.1\% \text{ FS})$	MKS	1179BX 14C R 1 B V	06/12/2024	-
PT after the MFC for RJ inlet pressure (PT2)	10 000 torr (~ 13 bar)	analog signal $\pm 0.5\% \text{ RD}$	MKS	722B14TCD2FA	13/04/2024	-
PT before the MFC for the mass flow UBC (PT1)	10 000 torr (~ 13 bar)	analog signal $\pm 0.5\% \text{ RD}$	MKS	722B14TCD2FA	20/04/2024	-
VG TTR91 Main Measure vacuum pressure 1E-2 - 1000 mbar	5E-4 – 1000 mbar	analog signal $\pm 5\% \text{ RD}$ at 1E-3 to 100 mbar	Leybold	TTR91	01/04/2016	-
VG TTR91 Hatch Measure vacuum pressure 1E-2 - 1000 mbar	5E-4 – 1000 mbar	analog signal $\pm 5\% \text{ RD}$ at 1E-3 to 100 mbar	Leybold	TTR91	26/03/2016	-
VG ITR90 Main Measure vacuum pressure 1E-4 - 1000 mbar	5E-10 – 1000 mbar	analog signal 15%RD at 1E-8 – 1E-2 mbar > 15% RD at 1E-1 - 1000 mbar	Leybold	ITR90	01/06/2024	-
VG ITR90 Hatch Measure vacuum pressure 1E-4 - 1000 mbar	5E-10 – 1000 mbar	analog signal 15% RD at 1E-8 – 1E-2 mbar > 15% RD at 1E-1 - 1000 mbar	Leybold	ITR90	12/12/2023	-

4.7.3. Auxiliary

The auxiliary equipment is also supplied in a tabular form in Table 4.7.

Table 4.7.: Auxiliary Equipment

Equipment/Resource	Use/Properties
ALTA Control Box XR100 CB-01	To connect the MFC and PT to the system
Swagelok filter SS-4FW-VCR-15	Filter to prevent particles 15 μ m from RJ inlet
Swagelok valves SS-4BG-V51	To manually control the flow during procedures
ISO-K 250 flange with two KF16 FT-connections and two VCR connections	Support the weight of the MFC, PT and whole gas feeding line.
TC FT KF16, Type K, TFT2KY00008 from Kurt J. Lesker	Thermocouple feedthrough into the vacuum chamber to connect all 4 thermocouples
RJ heater electrical FT model undetermined reaching 56 degC with 3.5A	Power to the RJ's internal heaters. All 4 wires are passed through (A1,A2,B1,B2).
Argon bottle	Propellant for the RJ. Westfalen Argon 6.0, Volume: 10 Liters, Pressure: 200 bar(a)
Pressure regulator for Argon Messer FM60-1	Nitrogen max. in pressure 200 bar max. out pressure 10 bar
Leak detector Leybold PhoeniXL300	Outputs leak rate of detected Helium to quantify leaks (Calibrated in 09/2023)
Helium Bottle	To spray Helium on the connections for leak detection
GPIB Adapter from NI	To connect the sourcemeter to the EXTRA DAQ
Camera Sony Alpha 7 IV (ILCE-7M4)	Used to video record the view inside the vacuum chamber during the test
Mass balance Sartorius BP 211D	Used during the procedure to characterize the VCA borrowed at the ESA materials laboratory

5. Results and Analysis

5.1. Post Processing

5.1.1. VCA Characterisation

In order to identify the relationship between the applied current I_{VCA} and the resulting force F_{VCA} , the voice coil actuator (VCA) and its magnet assembly have been mounted on top of a mass balance (Sartorius BP 211D), while a sourcemeter (Keithley 2440) was driving the VCA by a known current. The measurement result table of this characterisation is given in Table A.2.

As foreseen by the user manual of the ICL-TB, this data is to be linear fitted on the range that is planned to be used in the test [40]. Note that the fitted parameters change depending on the points that are being considered. In this test a thrust of around 125 mN was expected, therefore the rough range of 0 - 190 mN was considered for the linear fit, which corresponds to the measured points between 0 - 350 mA in current. The linear fit for this selected range is shown in Figure 5.1.

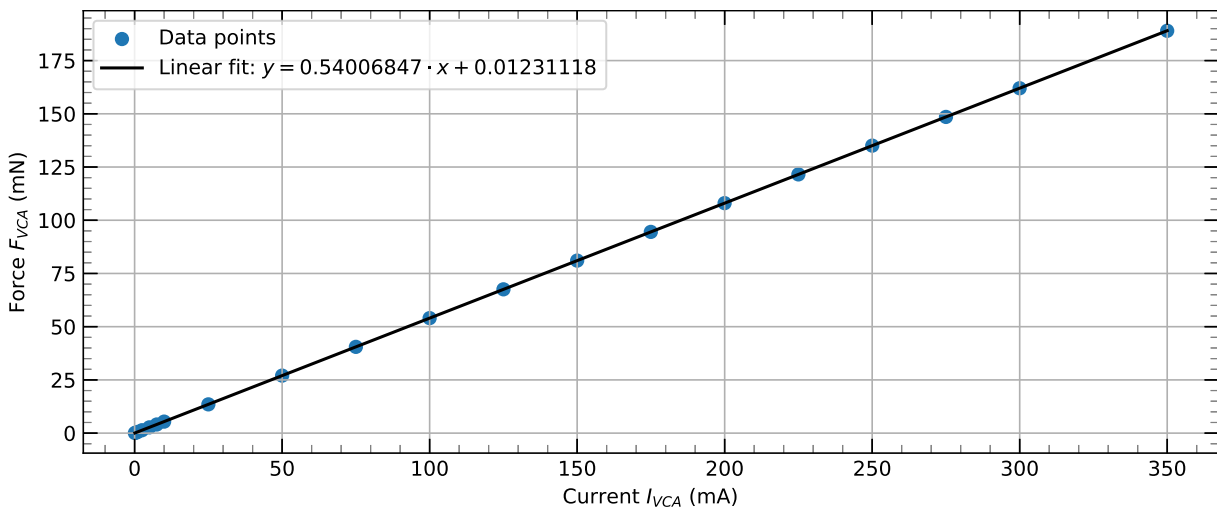


Figure 5.1.: Linear fit for the VCA characterisation

The acquired linear fit in this case shows a remarkable R^2 of 0.99999995 which underlines the linearity of this relationship. The gradient v_1 and the intercept v_2 are now set as in Equation 5.1, where only the gradient v_1 will be used later for the sensitivity parameter.

$$\begin{aligned} v_1 &= 0.540068468 \frac{mN}{mA} \\ v_2 &= 0.012311175 mN \end{aligned} \quad (5.1)$$

5.1.2. Cross Calibration

The cross calibration identifies the relationship between the applied current of the VCA and the resulting displacement measured by the laser. The VCA is current controlled by the same sourcemeter (Keithley 2440) and the distance is measured by the laser (optoNCDT 1700-1). To apply the current and processing the laser displacement for each step was initially supplied as a manual procedure, which turned out to be very time-consuming and tiresome. In order to improve on this, both the execution and the post processing was automated in this work. For the auto-cross-calibration execution, a LabView software was written that commands the sourcemeter through a pre-defined sequence of currents and timings. The parameters for the sequence definition that was used for this test are the steps in current from the VCA calibration with a 30 s enabled time and a 60 s wait time, resulting in an increasing square wave pattern.

For the post processing of the auto-cross-calibration, a MATLAB code was developed, that is able to process the entire pattern at once. This is achieved by aligning the known pattern of current with the laser distance flanks. The natural frequency of the balance has been filtered out through a newly developed method, identical to Section 5.1.4. The flank detection was previously not an algorithm either but a manual selection through a user interface. The here introduced algorithm for the flank detection is quite extensive and due to secondary importance described in the appendix in Section A.2. After the flank has been found, the pattern can be aligned to determine the displacement for each set-point of current. The resulting alignment is shown in Figure 5.2, with the zero reference and the enabled value which are used to calculate the displacement.

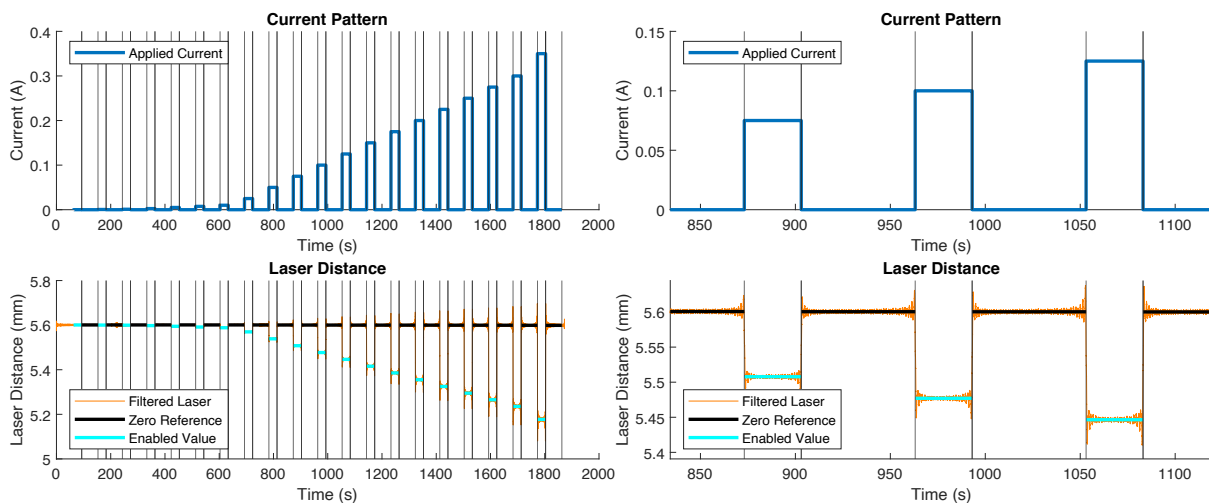


Figure 5.2.: Pattern alignment of the auto-cross-calibration (left: full view, right: zoomed section)

The resulting data table of the cross calibration is given in Table A.3. The linear fit between current and displacement is shown in Figure 5.3.

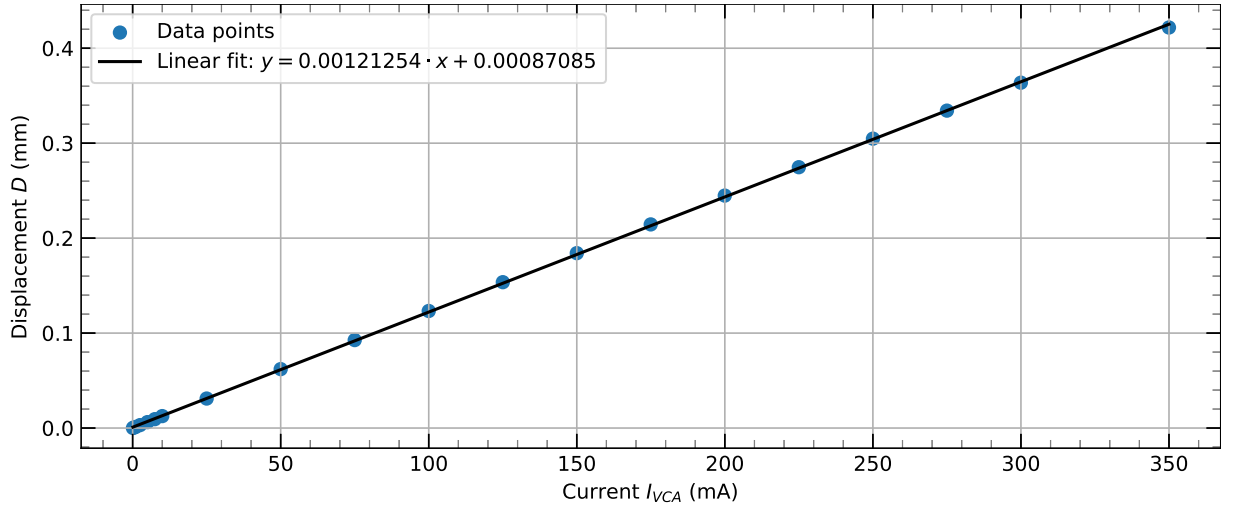


Figure 5.3.: Linear fit for the cross calibration

The gradient c_1 and the intercept c_2 of the cross calibration are now set as in Equation 5.2.

$$\begin{aligned} c_1 &= 0.001212545 \frac{mm}{mA} \\ c_2 &= 0.000870848 mm \end{aligned} \quad (5.2)$$

The sensitivity parameter S_{cal} can now be determined by both gradients v_1 and c_1 to achieve the relationship between displacement and force (Equation 5.3).

$$S_{cal} = \frac{c_1}{v_1} = 0.0022451686 \frac{mm}{mN} \quad (5.3)$$

Additionally, the intercept b_{cal} is computed in Equation 5.4, which is used for the uncertainty calculation.

$$b_{cal} = \left(v_2 - v_1 \cdot \frac{c_2}{c_1} \right) \cdot S_{cal} = -0.00084320717 mN \quad (5.4)$$

5.1.3. In-situ Calibration

The purpose of the In-situ calibration is to ensure that the conditions have not changed from the point of the cross calibration, so that the sensitivity factor is still valid. This can not be done via the VCA assembly, as electromagnetic interference is feared, which is why the VCA assembly is removed before vacuum is applied. It is instead achieved by a servo motor that is installed on the balance that can exert a small force on the balance depending on the angle it is commanded. The servo has a predefined pattern that puts a range of forces on the balance. This pattern and the alignment with the laser recording can be seen in Figure 5.4. In order to automatically post process these recordings as well, the MATLAB code from Section 5.1.2 was reused, as it is effectively the identical task with a different pattern. Note that the servo pulls the balance in the opposite direction than the VCA or the thruster. This is an issue that was already present when the balance got delivered and should be fixed by changing the arrangement of the servo in the future.

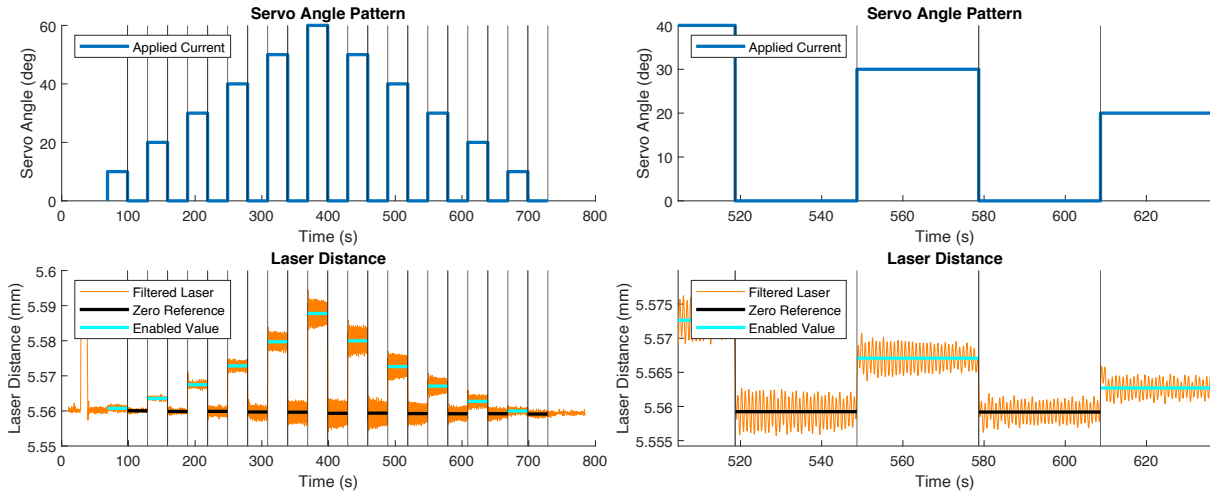


Figure 5.4.: Pattern alignment of the auto in-situ calibration (left: full view, right: zoomed section)

Note that the exact amount of the forces applied by the servo is unknown, only the repeatability of those forces is of importance for now. However, ideally the applied forces would match the range of forces applied during the cross calibration, which is a point to improve on for the future. The procedure of the user manual was extended with a criterion on how much deviation is allowed, as well as how this criterion is derived. Therefore, in order to verify the legitimacy of the sensitivity factor, the following approach was taken. The in-situ calibration is first done immediately after the cross calibration to create a baseline. This baseline should not only provide the expected displacement for each angle of the servo, but also tell how much deviation can be expected naturally as the setup is not perfectly reproducible. This is achieved by performing the in-situ calibration baseline twice. The average of the change in displacement between baseline1 and baseline2 is called in-situ calibration threshold value (ICTV). The result data of the baseline recordings is shown in Table 5.1, which results in an $ICTV = \overline{\Delta D} = 0.000241212 \text{ mm}$.

Table 5.1.: In-situ calibration baseline result

	Baseline1	Baseline2	
Servo Angle (deg)	Displacement D (mm)		ΔD
10	-0.00037	-0.00045	7.6625E-05
20	-0.00344	-0.00357	0.0001331
30	-0.00791	-0.00777	0.000143543
40	-0.01384	-0.01374	0.000109322
50	-0.02114	-0.02065	0.000497156
60	-0.02955	-0.02926	0.000288136
50	-0.02041	-0.02042	9.51457E-06
40	-0.01373	-0.01341	0.000319643
30	-0.00834	-0.00774	0.000604874
20	-0.00332	-0.00322	9.96813E-05
10	-0.00043	-0.00080	0.000371732

This ICTV is now expanded by the factor 3 to define a range of acceptable deviation when the in-situ calibration is done before and after the test in vacuum. The factor of 3 is debatable, however this expanded $3 \cdot ICTV$ can be translated into a thrust uncertainty, which in this case amounts to 0.32 mN. Ideally a requirement on thrust uncertainty would be used here for future tests to define the expanded ICTV. The in-situ calibrations before and after the test are called spotcheck1 and spotscheck2, and can now be compared to both baselines and the expanded $3 \cdot ICTV$. If the mean deviation in displacement $\overline{\Delta D}$ is bigger than $3 \cdot ICTV$, the test would need to be aborted and repeated. The result of the spot check in-situ calibrations and the pass/fail of the criterion is shown in Table 5.2.

Table 5.2.: In-situ calibration spot check result

	Baseline1 $\overline{\Delta D}$ (mm)	Criterion ($3 \cdot ICTV$) < 0.000724 mm	Baseline2 $\overline{\Delta D}$ (mm)	Criterion ($3 \cdot ICTV$) < 0.000724 mm
Spotcheck1	0.000378	pass	0.000206	pass
Spotcheck2	0.000491	pass	0.000296	pass

5.1.4. Thrust Measurement Method

In order to achieve the most meaningful thrust signal from the laser distance recording, two processing steps are applied on the laser distance data before the mapping to thrust values is applied. The first modification is the removal of the natural frequency of the balance, which is not part of the thrust signal. The second modification is the zero point adjustment, as the zero point experiences a drift over time.

Natural Frequency Removal

The method originally supplied in the user manual of the thrust balance is a 5th order Butterworth filter with a cut off frequency around 0.0015 Hz [40]. This however, acts like a low pass filter and suppresses not only the natural frequency, but also all other high frequencies altogether. This is a problem, as those frequencies can not be surely assigned to be external noise, they could be part of the exerted thrust from the thruster. Therefore, the thrust signal is supposed to retain all noise components, to not suggest a lower noise floor than actually present, which is especially of importance for the determination of the uncertainty. As a solution a method is created here to remove the natural frequency of the balance while ideally retaining all other frequencies of the thrust signal. The approach here is to convert the recording into the frequency domain by a fast Fourier transform (FFT), where the natural frequency can be identified precisely. In the frequency domain are then the magnitudes of the natural frequency set to zero before it is transformed back into the time domain.

One crucial prerequisite for applying a fast Fourier transformation (FFT) is that all time steps in the recording are equally sized. The distribution of the time steps of the acquired measurements during cold flow and hot flow is illustrated in Figure 5.5. It can be seen that the time steps are not perfectly identical over the full data-set, however they feature a very low standard deviation of only $0.378 \mu s$, which corresponds to 0.0945 % of the average $400 \mu s$. Interestingly almost identical characteristics can be observed in both data-sets. This low variation in time step size is taken as a sufficient condition to apply a FFT.

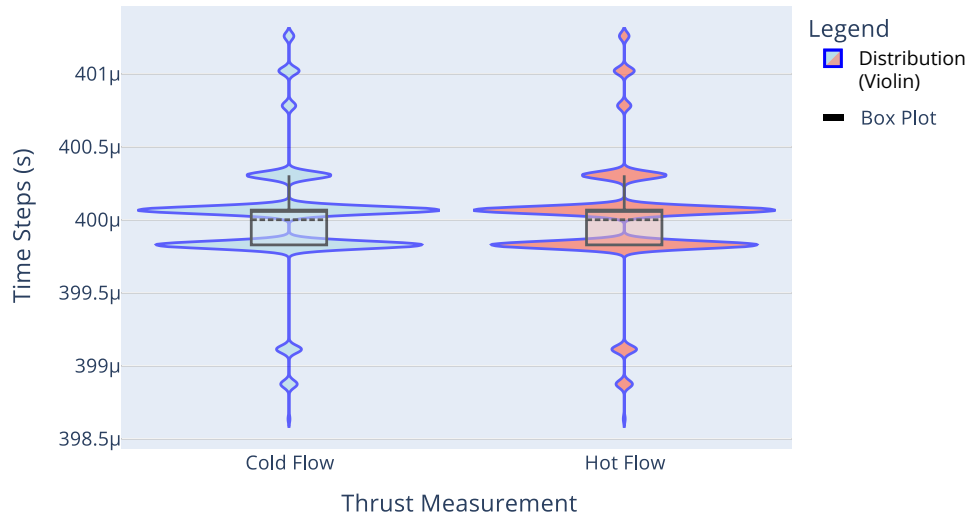


Figure 5.5.: Distribution of the time step variation in the two thrust measurements

The result of the FFT of the cold flow measurements can be seen in Figure 5.6, where the natural frequency of the balance can be identified by the significant magnitude spike around 1 Hz. Note that this spike is not perfectly thin, but affects surrounding frequencies, which results in a smeared out influence of this natural oscillation. Additionally, the harmonics of multiples of the natural frequency can be seen as well around 2.2 Hz, which also features the smeared out effect.

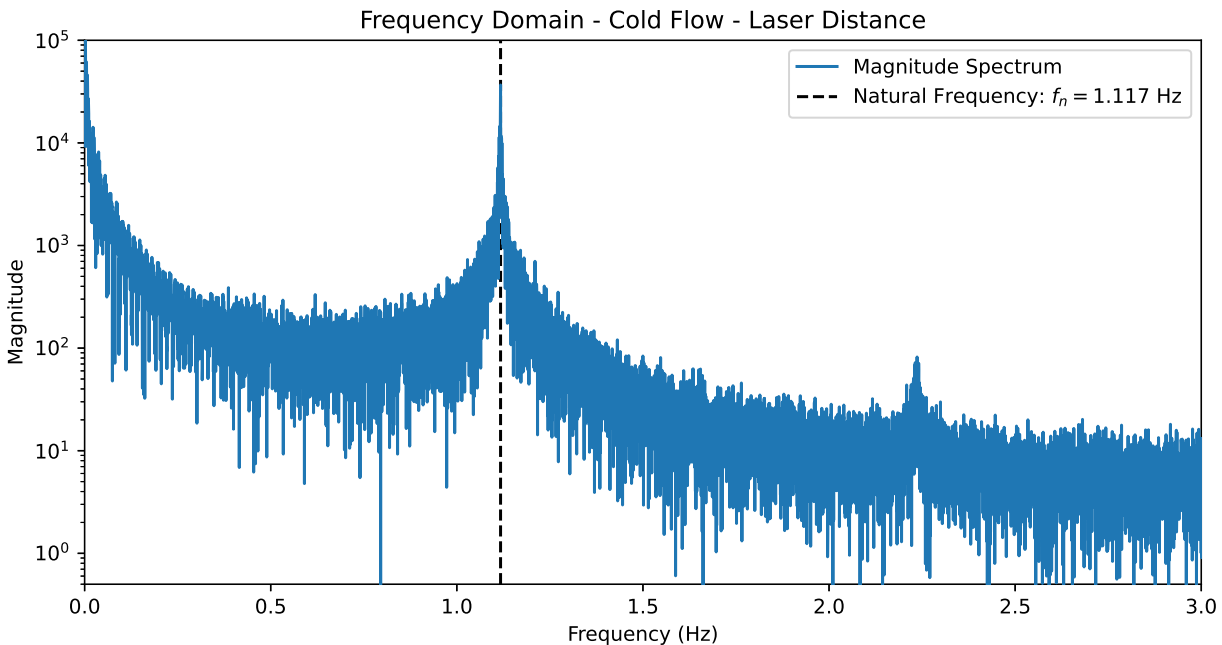


Figure 5.6.: Fast Fourier transform of the cold flow measurement in the frequency domain

In order to remove the influence of the natural oscillation, not only the natural frequency itself with $f_n = 1.117$ Hz is removed, but a range of $f_n \pm 0.3$ Hz. Hereby is the value of 0.3 Hz debatable as it influences the noise magnitude later in the time domain. It was chosen here as it covers the main part of the smeared out spike, so that the result is a more continuous noise level, which is shown in Figure 5.7.

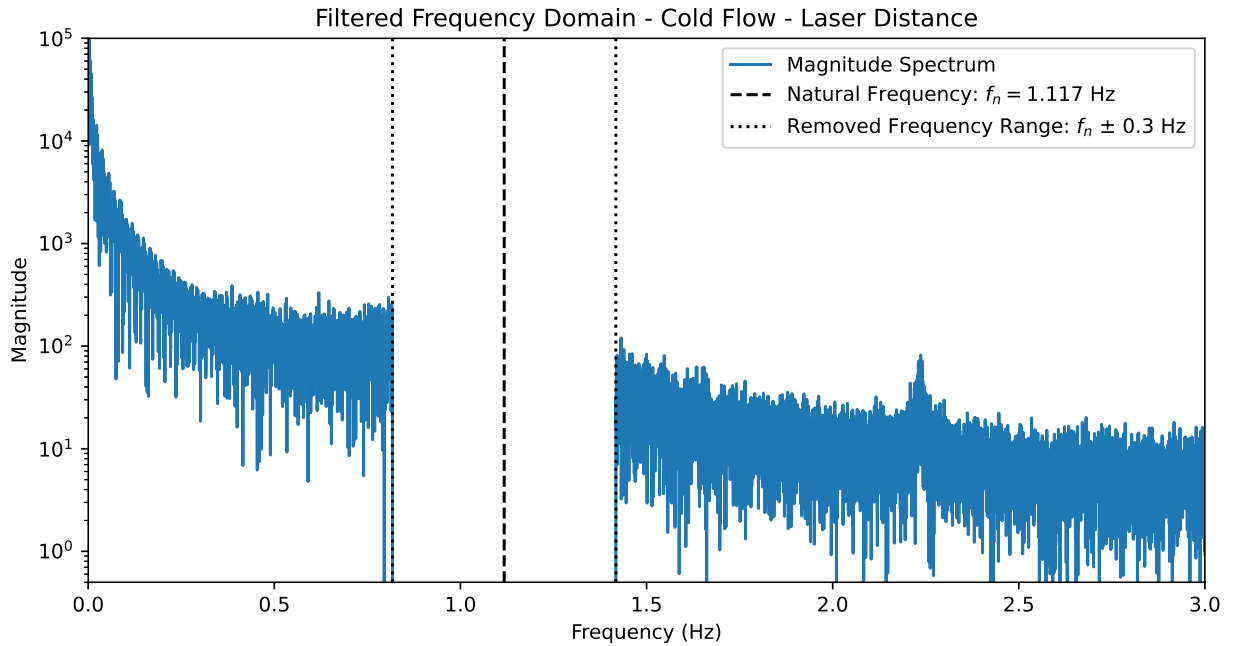


Figure 5.7.: Filtered fast Fourier transform of the cold flow measurement in the frequency domain

While the selected range of frequencies is considered to be primarily caused by the natural oscillation, it can not be ruled out that relevant noise was present under these frequencies. In fact the EPL has conducted noise characterisation studies in the past [7], which showed increased noise levels from 10 Hz and higher on the structures (Figure A.2) and especially elevated noise levels around 1 Hz on a balance when thrust was applied (Figure A.3). In those past tests, a reference setup (labeled as TCA) was measuring the noise only in order to subtract the noise from the thrust setup (labeled as MBA). Such a noise measuring reference does not exist on the ICL thrust balance.

The result of the frequency removal can be seen in Figure 5.8 in three different zoomed sections, which show that the filtered signal features no characteristics of the major oscillation from the raw signal, yet a noise band and smaller disturbances are preserved, which would have been lost with a Butterworth filter.

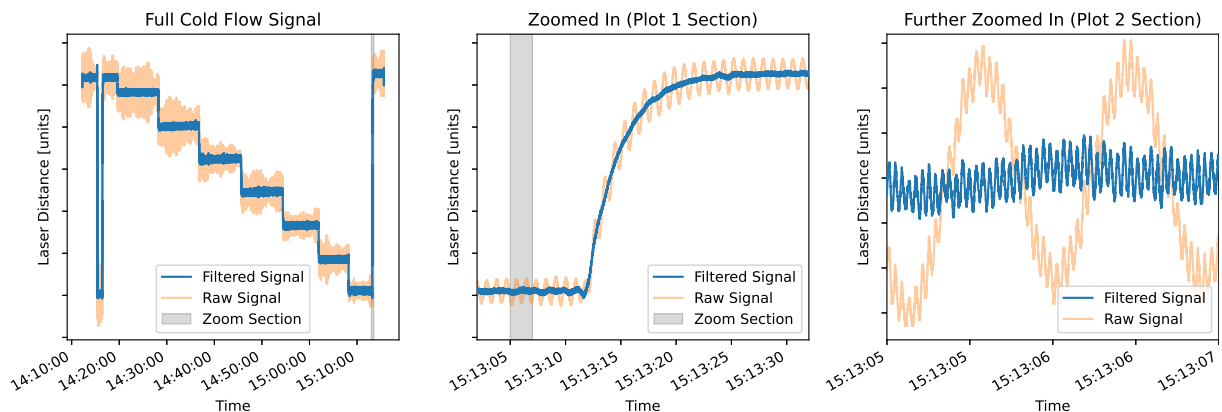


Figure 5.8.: Result of the natural frequency removal of the cold flow laser distance data

Zero Point Adjustment

In order to transform the laser distance recording into a thrust value, a zero point reference has to be defined. This is due to the functional principle of the thrust balance that a relative displacement is mapped to a corresponding force. To obtain this zero reference in laser distance, a no-thrust phase is required. The two no-thrust phases in the start and the end of the cold flow test are shown in Figure 5.9.

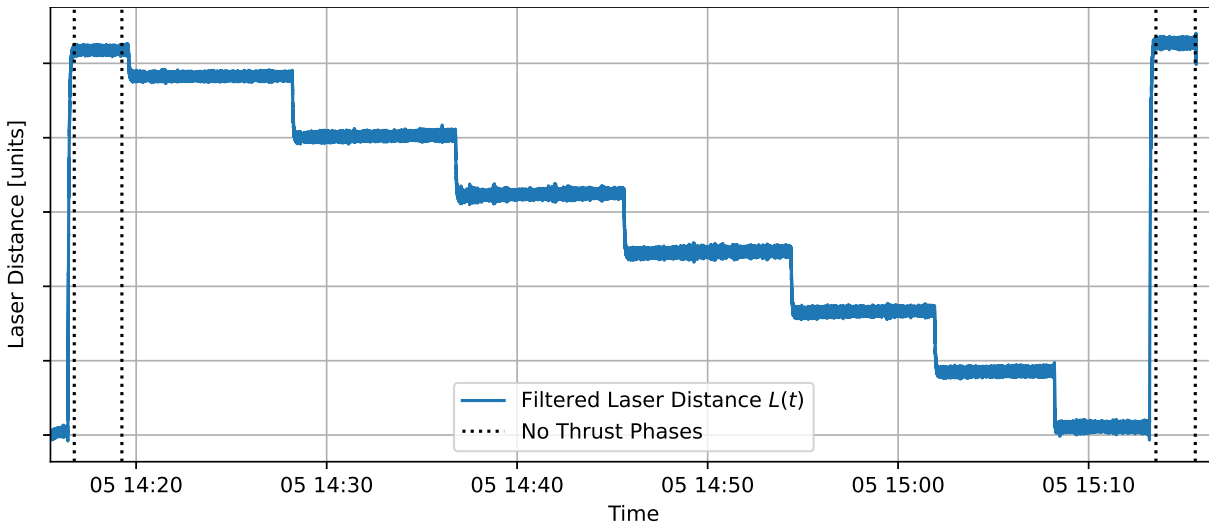


Figure 5.9.: No thrust phases marked in the filtered laser distance of the cold flow test

According to the user manual of the ICL-TB [40], the displacement for the thrust value is obtained by the difference between two linear fittings, once on the thrust phase and once on the no thrust phase immediately after. However, this imposes the restriction to measure the thrust only point-wise, and not as a continuous signal. In the attempt to improve on this, this procedure is revised to define a zero reference over the full recording, so that a continuous thrust signal can be obtained. Note that hereby the result of the point-wise measurement (old procedure) is practically identical and contained in the continuous measurements obtained by this new procedure. For the cold flow measurement this is the case for the last step tested, as the thruster was shut off directly afterwards. Note that for a hot flow measurement of the resistojet, the thruster can not be shut off directly after, as the filament would get damaged, therefore a point-wise measurement according to the old procedure is generally inappropriate.

The new procedure developed here defines a zero point reference over time by the two no-thrust phases in the start and the end. As this zero point reference experiences a drift over time, this imposes an interpolation and a characteristics assumption for the zero drift in the thrust phase. This drift is not only present between two no-thrust phases around a thrust phase, but also within a no-thrust phase itself. The drift characteristics is assumed linear, which is fitting the drift within a no-thrust phase very well. If a pure linear drift, decoupled from the thrust, would be present, the linear fit of the two no-thrust phases would be identical, when extended to the other. As shown in Figure 5.10 this is not completely the case, which invokes, that the drift is not purely linear. However, as there is no further information available on the drift characteristics, the linear fit over both no-thrust phases (black line in Figure 5.10) is used as the zero reference for the measurement.

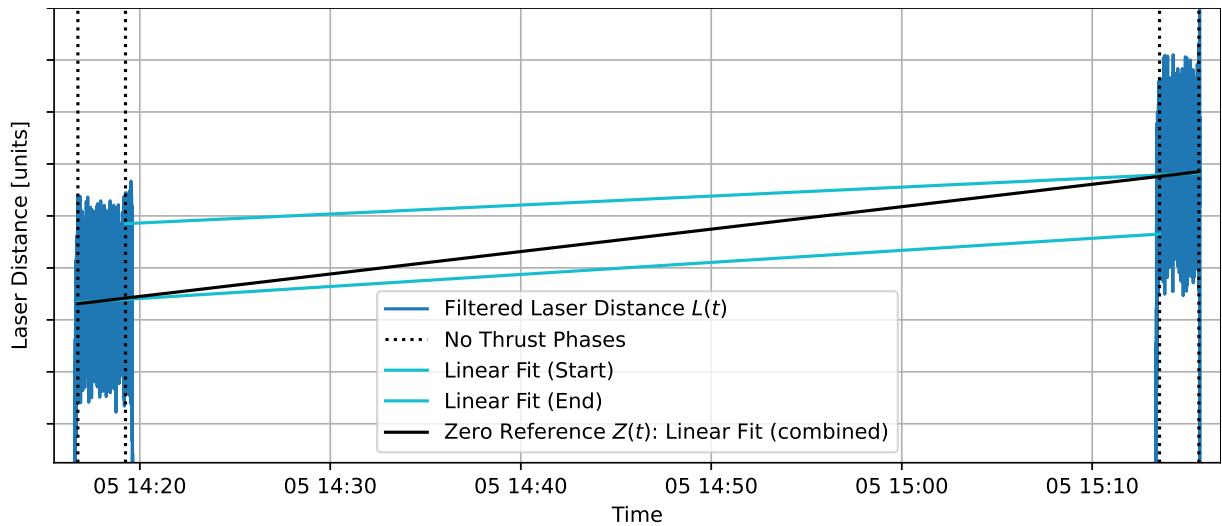


Figure 5.10.: Zero reference $Z(t)$ determination of the cold flow measurement (closeup)

Displacement

With a continuous zero reference $Z(t)$ defined, the continuous displacement $D(t)$ can be simply calculated by subtracting the continuous laser distance $L(t)$ from the zero reference as in Equation 5.5. The resulting displacement is plotted in Figure 5.11 for the cold flow data.

$$D(t) = Z(t) - L(t) \quad (5.5)$$

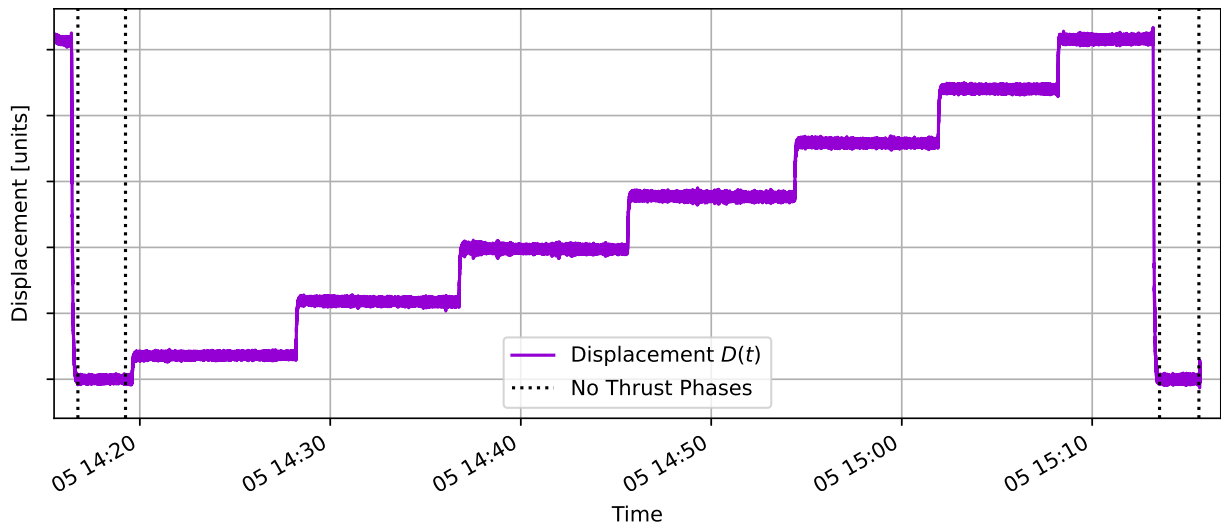


Figure 5.11.: Displacement $D(t)$ of the cold flow measurement

Thrust Mapping

The continuous thrust signal $F(t)$ can now be yielded from the displacement by the sensitivity factor $Scal$ by Equation 5.6. The sensitivity factor was determined earlier from the results of the VCA characterisation and the cross calibration. The resulting thrust signal for the cold flow measurement can be

seen in Figure 5.12, which concludes the post processing efforts. Although only the cold flow is shown here as an example, the hot flow measurements were processed in the identical way.

$$F(t) = \frac{D(t)}{Scal} \quad (5.6)$$

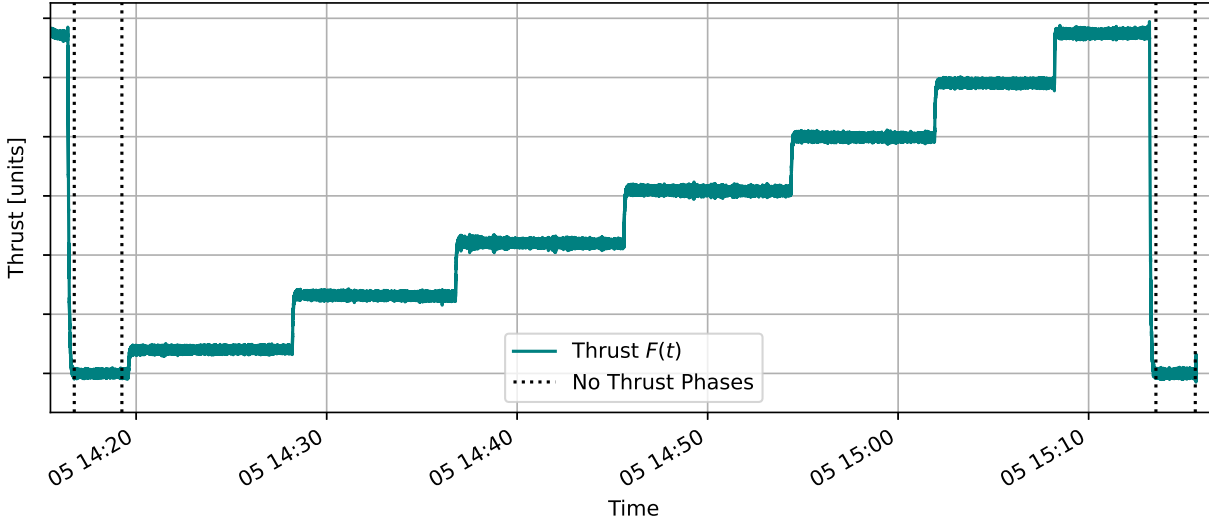


Figure 5.12.: Thrust $F(t)$ of the cold flow measurement

5.1.5. Pressure Variation Test

In order to characterise the pressure dependency of the mass flow controller (MFC), a pressure variation test is performed. The pressure is varied with $\pm 4\%$ around the target pressure for three levels of mass flow across the range that is used in this test. The continuous pressure and mass flow recordings have been hand-selected and averaged to determine the result value in Table 5.3. The relative standard deviation is used for the mass flow uncertainty, where the worst case is assumed, which is $\sigma_{rel} = 1.67532\%$. Note that this deviation is unusually big, which is caused by a single measurement and the low sample number.

Table 5.3.: Result of the pressure variation test in normalised units

Set mass flow \dot{m}_{set} (units)	Pressure before MFC p_{PT1} (units)	Read mass flow \dot{m}_{read} (units)	standard deviation σ (units)	arithmetic mean $\bar{\dot{m}}_{read}$ (units)	relative standard deviation to mean σ_{rel} (%)
0.0802	0.9570	0.07733	9.316 E-5	0.07727	0.12056
	0.9998	0.07735			
	1.0398	0.07714			
0.6057	0.9622	0.58890	8.044 E-6	0.58891	0.00137
	1.0010	0.58892			
	1.0394	0.58892			
1.0000	0.9604	0.94151	1.616 E-2	0.96436	1.67532
	1.0104	0.97586			
	1.0432	0.97571			

5.2. Test Results

5.2.1. Cold Flow Test

The base characteristic of the resistojet is the performance under pure cold flow conditions, which is characterised here by operating the resistojet on different levels of inlet pressure. The relevant variables of this cold flow test can be seen in Figure 5.13 as a time series, which is put together from various DAQs.

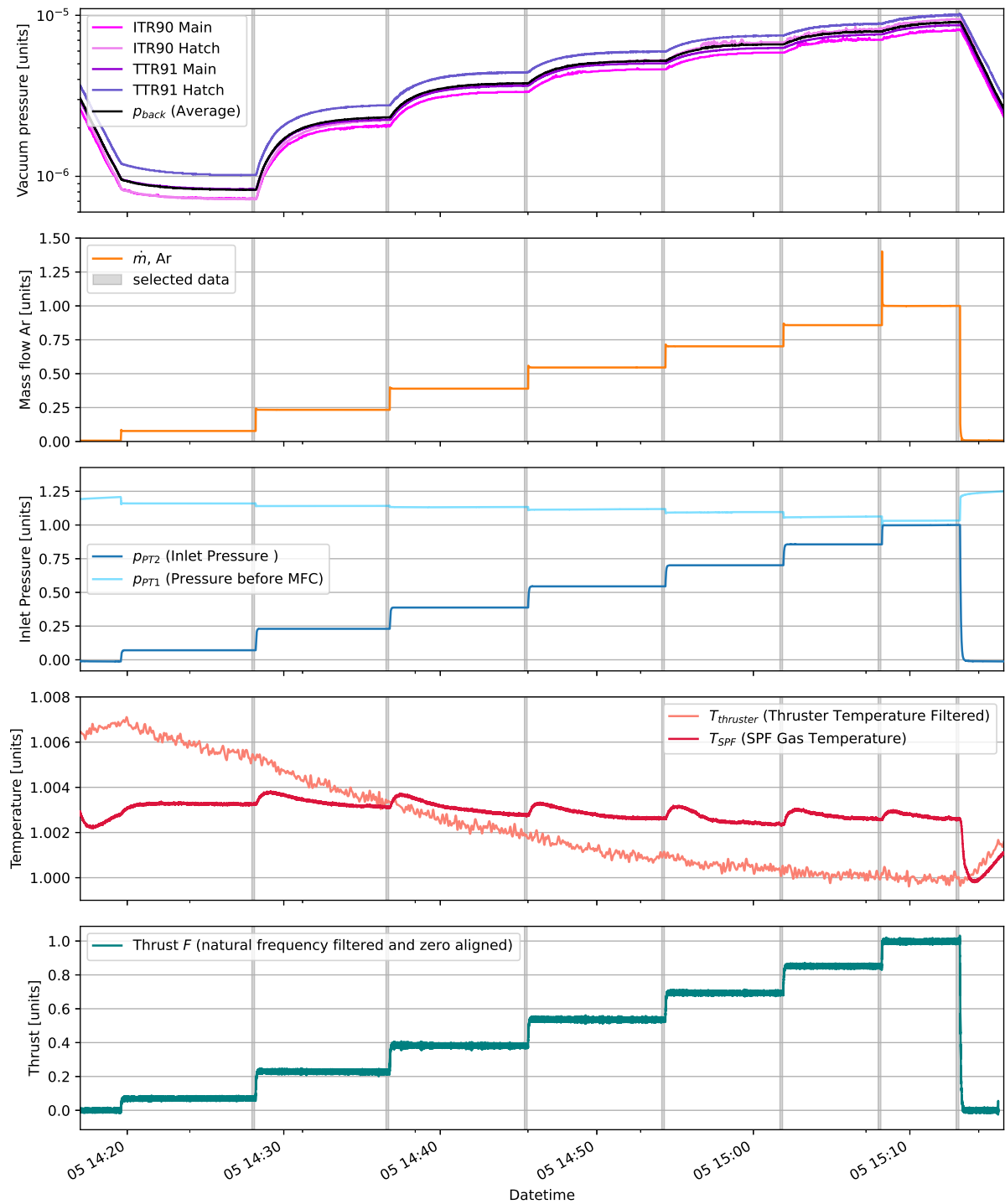


Figure 5.13.: Cold flow test timeline in normalised units (steady state sections marked in grey)

The grey marked areas in Figure 5.13 indicate the sections (each 10 seconds long) that are used to determine the performance at these equilibrium conditions. The average performance in those operation points is listed in Table 5.4, where F_{calc} and $I_{sp,calc}$ are estimations by the ALTA XR-100 control software. Note that only every second planned operation point was executed, as the stabilisation in background pressure took more time than expected and a buffer of propellant was still required for the hot flow test.

Table 5.4.: Result table of the cold flow test in normalised units

OP	\dot{m} [units]	p_{in} [units]	p_{back} [units]	$T_{thruster}$ [units]	F_{calc} [units]	F [units]	$I_{sp,calc}$ [units]	I_{sp} [units]
1	0.0773	0.0708	0.09044	1.0054	0.0675	0.0700	0.8732	0.9061
3	0.2334	0.2300	0.25581	1.0034	0.2194	0.2272	0.9400	0.9731
5	0.3895	0.3875	0.41667	1.0019	0.3697	0.3810	0.9493	0.9784
7	0.5457	0.5447	0.57235	1.0010	0.5197	0.5356	0.9523	0.9814
9	0.7017	0.7013	0.72545	1.0002	0.6690	0.6930	0.9534	0.9875
11	0.8580	0.8564	0.87339	1.0000	0.8170	0.8514	0.9522	0.9923
13	1.0000	1.0000	1.00000	1.0000	0.9540	1.0000	0.9540	1.0000

A comparison is drawn in Table 5.5 to the *Acceptance Test* of the EPL from 2013 [9]. It shows that the inlet pressure and mass flow have been almost perfectly reproduced, while the measured thrust and specific impulse are about 20% larger than in the *Acceptance Test*. The characterisation is visualised in Figure 5.14, which represents the determined performance map of the XR-100 resistojet in cold gas mode, including the uncertainties that will be determined later in Section 5.3.

Table 5.5.: Comparison of the cold flow test to the acceptance test in normalised units

	p_{back} [units]	p_{in} [units]	$T_{thruster}$ [units]	\dot{m} [units]	F_{calc} [units]	F_t [units]	$I_{sp,calc}$ [units]	I_{sp} [units]
<i>Acceptance Test</i>	1.00000	1.00000	1.00000	1.00000	1.09544	1.00000	1.13223	1.00000
This test	2.56338	1.01649	1.00476	1.00058 ± 0.0154	1.14004	1.20156 ± 0.0103	1.13963	1.20110 ± 0.0104
Δ [%]	+156.3%	+1.6%		+0.06 %		+20.1%		+20.1%

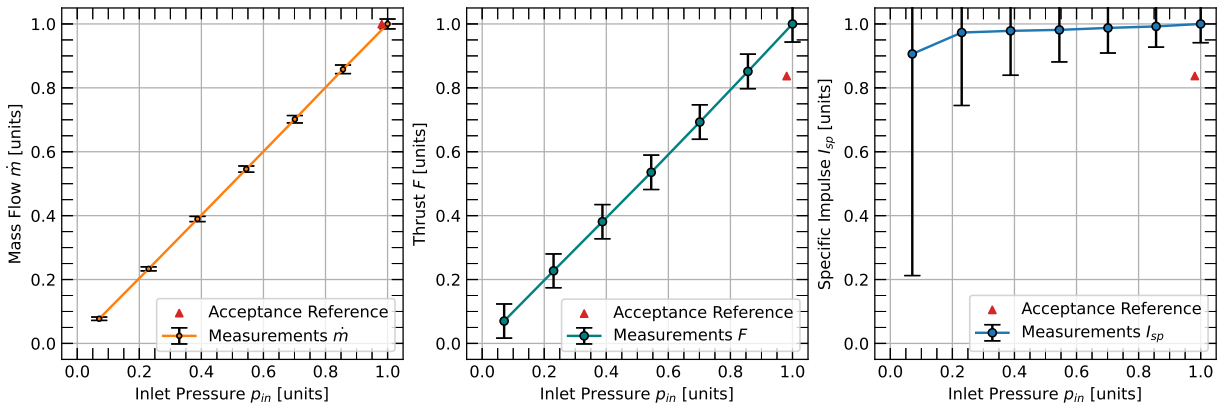


Figure 5.14.: Performance map of the XR-100 in cold gas mode (normalised)

The reason for this high deviation in thrust and therefore specific impulse is considered to be caused by the uncertainties of the two thrust balances. When the measured thrust from the *Acceptance Test* is compared to the expected value of the control software F_{calc} of that test, it is evident that actually less thrust than expected was measured (about -9%). In contrast, the thrust measurements of this test have been higher than the expected values from the control software (about $+5\%$). This shows that the calculated values from the ALTA control software are actually in between the measurements of the *Acceptance Test* and this test. Luckily there is one more point of reference available, which is from 2013 the ALTA internal testing result [35]. Together, all this data with its proportional relationship is visualised in Figure 5.15, which shows that the ALTA internal test from 2013 does almost perfectly match the expected values F_{calc} from both EPL tests and the measurements of the EPL are distributed around. This is taken as a reason to assume that the actual thrust is nearby F_{calc} and thrust measurement uncertainties are present in both EPL tests.

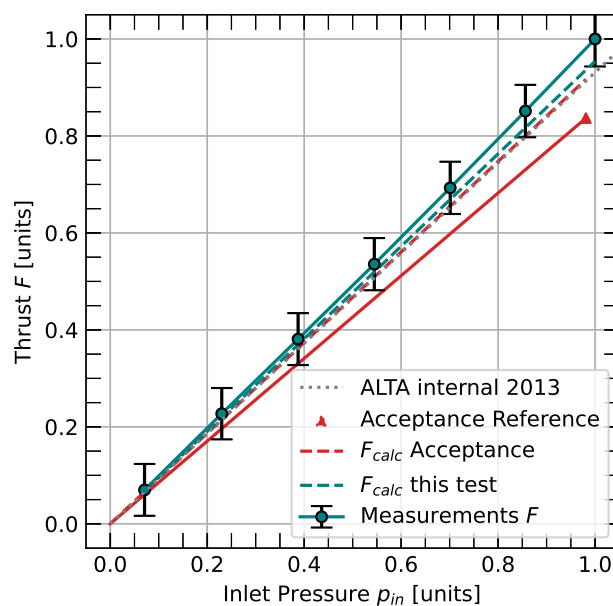


Figure 5.15.: Thrust results of multiple tests of the XR-100 in cold gas mode (normalised)

5.2.2. Hot Flow Test

The hot flow mode of the resistojet is its primary point of operation, where the electrical heating of the gas reduces the mass flow and the specific impulse is increased. The execution of such an operation requires a continuous mass flow while the thruster goes through a heat up phase. During this heat up phase the voltage is increased in steps. This voltage is then held constant for a few minutes, according to the user manual [36]. This procedure was executed, when for the final step in voltage suddenly the control software did shut down the power supply to the resistojet. After further investigation it became evident that one of the two heaters behaved abnormal and became unstable in the heat up phase and finally burned through, which triggered an alarm in the control software to shut down the power. However, this alarm did not prevent the burn through of the filament, so that afterwards no electrical continuity was measurable on heater A. Unfortunately, despite this thruster having two heaters for redundancy, the control software did not allow to operate the thruster on one heater alone. After multiple attempts to re-initiate the heat up phase with one heater alone, which was always interrupted by the control software,

5. Results and Analysis

the hot flow test had to be declared failed. This timeline of events can be followed well in the recorded parameters in Figure 5.16

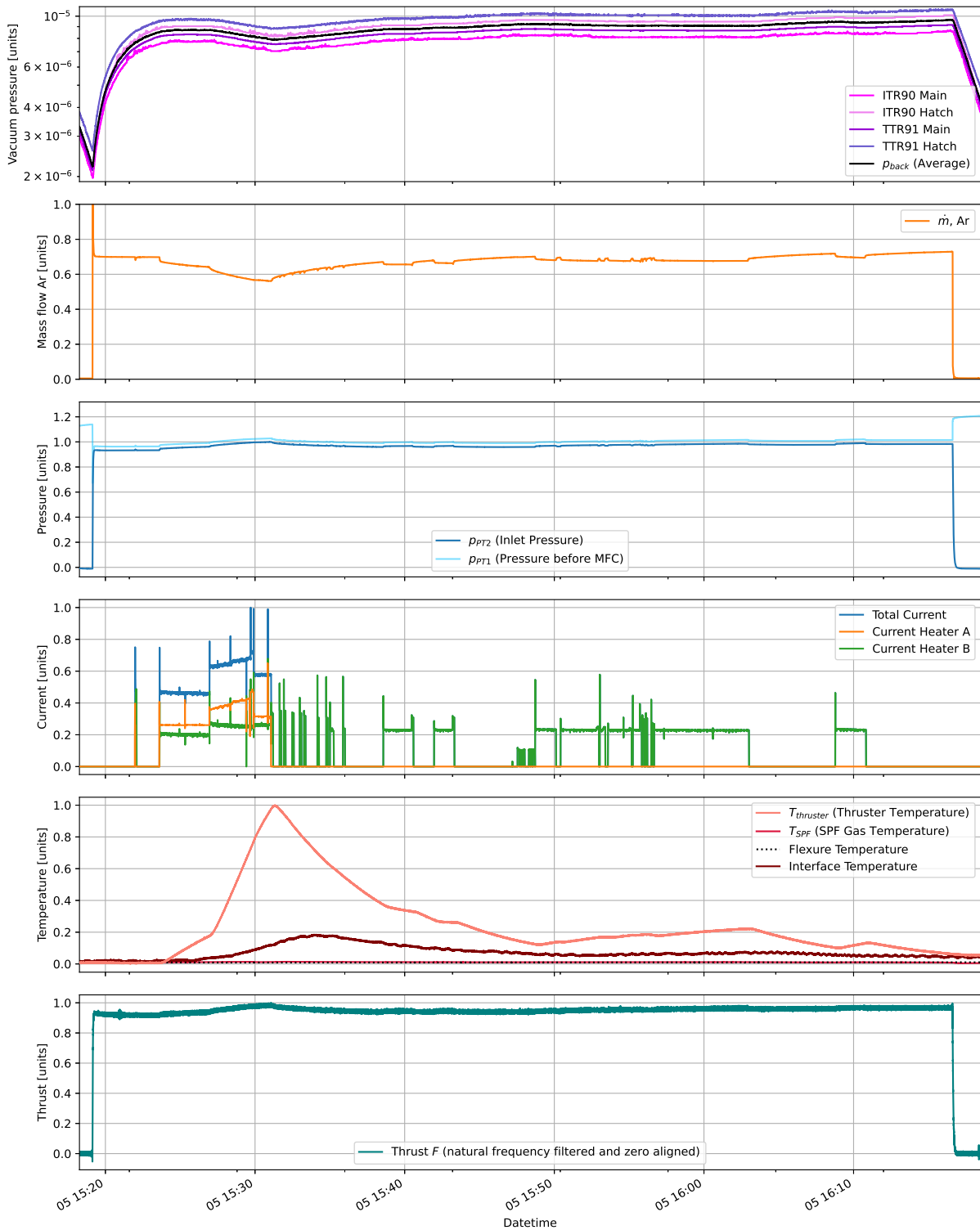


Figure 5.16.: Hot flow test timeline in normalised units

When the heater current is followed in Figure 5.16, it can be seen that for the first step in voltage, the

current in both heaters jumps to a constant value, which is the nominal behaviour of the filament. With the second step in voltage, heater B (marked green) still behaves with a constant current consumption, however heater A (marked orange) shows a linear increase in current with even a random jump back to a constant consumption, which is its first indication of its failure. When the final step in voltage was applied, heater A has experienced a burn through.

Up until then, the thruster temperature was increasing steadily as expected, where the different gradients of the temperature increase in Figure 5.16 mark the steps in voltage applied and therefore also roughly the levels of power insertion. For this point in time, the resistojet was already working in its hot flow mode, which is clearly indicated by the decreasing mass flow, without a lower level in thrust. The pressure before the mass flow controller (MFC) was not completely constant, which is caused by the pressure regulator drifting, and therefore also influenced the thrust, which would otherwise be expected to be more constant.

The whole duration of this test was recorded by a camera pointing into the vacuum chamber, which showed a point of light emitted from the resistojet under hot flow operation. On the video recordings it could also be seen, that this emission of light was not constant and occasionally increased in brightness into small flashes of light. This is considered the visual evidence of heater A's abnormal behaviour. A stacked photo from these video recordings is illustrated in Figure 5.17.



Figure 5.17.: The firing XR100 resistojet, emitting a point of light inside the vacuum facility during its heat up phase

Due to the reason that no equilibrium was reached, no meaningful characterisation for an operation point in the hot flow mode can be determined. This has the consequence that the test objectives regarding the hot flow mode could not be accomplished.

5.3. Uncertainty Calculation

5.3.1. Mass Flow Uncertainty

In order to state the uncertainty of the measured mass flow of one operating point, the EPL mass flow measurement procedure [38] is followed, which is based on the standard JCGM 100:2008 “*Guide to the Expression of Uncertainty in Measurement*” (GUM) [28]. The model equation 5.7, with variable definitions in Table 5.6, defines a number of influences that are being considered.

$$\dot{m}_f = \dot{m}_{f,meas} \cdot (1 + \delta\dot{m}_{f,cal} + \delta\dot{m}_{f,leak} + \delta\dot{m}_{f,press}) \quad (5.7)$$

Table 5.6.: Variable definition of the mass flow uncertainty budget calculation

Symbol	Unit	Definition
\dot{m}_f	mg/s	Mass flow to be determined
$\dot{m}_{f,meas}$	mg/s	Mass flow measured by the flow meter
$\delta\dot{m}_{f,cal}$	-	standard uncertainty of the calibration of the mass flow meter
$\delta\dot{m}_{f,leak}$	-	standard uncertainty due to propellant leaks in the flow line
$\delta\dot{m}_{f,press}$	-	standard uncertainty due to external and feed pressure variation

Depending on the source of knowledge of the uncertainty, the contributions are classified as type A or type B. Type A are series of observations, where type B are other means than observations, for example approximations or theoretical models [28]. The different influences from the model equation are grouped and listed in Table 5.7 with their type and distribution.

Table 5.7.: Mass flow uncertainty influences summary, types and distributions

Symbol	Value	Unit	Uncertainty	Type	Distribution	Sensitivity
$\dot{m}_{f,meas}$	\bar{x}	mg/s	$s(\bar{x})$	A	experimental	1
$\delta\dot{m}_{f,cal}$	0	-	$u_{f,cal}$	B	rectangular	$[\bar{x}]$
$\delta\dot{m}_{f,leak}$	0	-	$u_{f,leak}$	B	rectangular	$[\bar{x}]$
$\delta\dot{m}_{f,press}$	0	-	$u_{f,press}$	A	experimental	$[\bar{x}]$

Measurements

The first contribution to the uncertainty comes from $\dot{m}_{f,meas}$ itself, which is the standard deviation, more precisely the corrected sample standard deviation in Equation 5.8, of all N measurements x_i .

$$s(x) = \sqrt{\frac{1}{N-1} \sum_{i=1}^N (x_i - \bar{x})^2} \quad (5.8)$$

As the uncertainty decreases when more samples N are acquired, the actual contribution to the uncertainty is defined as the standard deviation of the mean in Equation 5.9.

$$s(\bar{x}) = \frac{s(x)}{\sqrt{N}} \quad (5.9)$$

Note that the average of this data series \bar{x} is also the only non-zero contribution to the absolute value, as listed in Table 5.7. The sensitivity coefficient α can be yielded by the partial derivative on the model equation, as shown in Equation 5.10.

$$\alpha_{f,meas} = \frac{\partial \dot{m}_f}{\partial \dot{m}_{f,meas}} = 1 + \delta \dot{m}_{f,cal} + \delta \dot{m}_{f,leak} + \delta \dot{m}_{f,press} = 1 \quad (5.10)$$

Calibration Certificate

The second influence is the uncertainty supplied with the calibration certificate, which is a defined range depending on the read value (RD) and the full scale (FS), in this case $\pm (0.005 \cdot RD + 0.002 \cdot FS)$. The read value boils down to \bar{x} and the full scale of the used mass flow controller is 416 mg/s Ar . In order to yield the uncertainty per unit of measured mass flow, the absolute uncertainty is normalised by $\dot{m}_{f,meas}$, which is \bar{x} . The half width hw of the rectangular distribution is therefore yielded through Equation 5.11.

$$hw_{f,cal} = \frac{(0.005 \cdot \bar{x} + 0.002 \cdot 416 \text{ mg/s})}{\bar{x}} \quad (5.11)$$

The standard uncertainty can be now derived from the rectangular distribution as in Equation 5.12.

$$u_{f,cal} = \frac{hw_{f,cal}}{\sqrt{3}} \quad (5.12)$$

The sensitivity coefficient α can be yielded again by the partial derivative on the model equation, as shown in Equation 5.13. The sensitivity coefficient is hereby rounded to the closest integer value.

$$\alpha_{f,cal} = \left\lfloor \frac{\partial \dot{m}_f}{\partial \delta \dot{m}_{f,cal}} \right\rfloor = \lfloor \dot{m}_{f,meas} \rfloor = \lfloor \bar{x} \rfloor \quad (5.13)$$

Propellant Leaks

The next influence is the mass flow by leaks in the feeding line, where the approximation from a previous test [12] is made, that if the maximum leak rate along the feeding line is below $1E - 7 \text{ mbar} \cdot \text{l/s}$, the uncertainty of $\delta \dot{m}_{f,leak}$ is lower than 0.01% of the mass flow. The standard uncertainty can therefore be directly computed as in Equation 5.14 by its rectangular distribution.

$$u_{f,leak} = \frac{0.0001}{\sqrt{3}} = 5.77E - 5 \quad (5.14)$$

Note that the leak testing with the helium leak detector could verify this requirement up until the last connection to the thruster and the thruster itself. Any leaks in that area are therefore not covered. The sensitivity coefficient can be yielded identical as before, as shown in Equation 5.15.

$$\alpha_{f,leak} = \left[\frac{\partial \dot{m}_f}{\partial \delta \dot{m}_{f,leak}} \right] = [\dot{m}_{f,meas}] = [\bar{x}] \quad (5.15)$$

Pressure Variation

The last considered influence is the pressure variation, for which the pressure variation test from Section 5.1.5 was conducted. The worst case result was a relative standard deviation of $\sigma_{rel} = 1.67532\%$. The standard uncertainty can be derived from the experimental distribution, as shown in Equation 5.16. The sample number is set to 9, as 3 pressures for 3 mass flow levels have been tested.

$$u_{f,press} = \frac{\sigma_{rel}}{\sqrt{9}} = 5.5844E - 3 \quad (5.16)$$

The sensitivity coefficient can be yielded identical as before, as shown in Equation 5.17.

$$\alpha_{f,press} = \left[\frac{\partial \dot{m}_f}{\partial \delta \dot{m}_{f,press}} \right] = [\dot{m}_{f,meas}] = [\bar{x}] \quad (5.17)$$

Note that the pressure variation test covered $\pm 4\%$ in pressure variation, however during the mass flow measurements the maximum pressure variation before the MFC was below $\pm 0.05\%$. Together with the unusually high σ_{rel} , due to an apparent outlier, the contribution to the uncertainty due to the pressure variation is likely to be overestimated.

Combined

The combined uncertainty can be calculated by the weighted sum as in Equation 5.18.

$$u_c = \sqrt{s(\bar{x})^2 + \alpha_{f,cal}^2 \cdot u_{f,cal}^2 + \alpha_{f,leak}^2 \cdot u_{f,leak}^2 + \alpha_{f,press}^2 \cdot u_{f,press}^2} \quad (5.18)$$

Finally, the combined uncertainty is expanded with a coverage factor k , which is set to $k = 2$ for a 95 % coverage level. This yields the expanded uncertainty u_e in Equation 5.19, which is rounded to one digit after the decimal as absolute value.

$$u_e = k \cdot u_c \quad (5.19)$$

When this set of equations is applied for each operation point (OP), the uncertainty in mass flow can be determined for all OPs, which is stated in Table 5.10.

The uncertainty budget calculation (UBC) was additionally carried out in a statistical software called GUM Workbench Pro, whose output tables are used in the reference EPL procedure [38]. The result table of GUM Workbench Pro is given for OP1 in Table 5.8 and for OP13 in Table 5.9, which are the operation points with the smallest and biggest mass flow measured in the cold flow test. When the ‘‘Index’’ value is compared between Table 5.8 and Table 5.9, it can be observed, how the different influences take over in significance when the mass flow is increased. For low mass flows, the combined uncertainty is almost

entirely determined by the uncertainty of the calibration certificate, where under high mass flows the uncertainty due to pressure variation slightly overtakes in significance.

Table 5.8.: Mass flow uncertainty normalised GUM Workbench Pro result table of OP1

Quantity	Value	Standard Uncertainty	Distribution	Sensitivity Coefficient	Uncertainty Contribution	Index
$\dot{m}_f, meas$	0.077303	1.165E-5	normal	1.0	1.155E-5	0.0 %
$\delta\dot{m}_f, cal$	0.0	0.0328	rectangular	0.077	2.551E-3	97.2 %
$\delta\dot{m}_f, leak$	0.0	2.778E-7	rectangular	0.077	4.477E-6	0.0 %
$\delta\dot{m}_f, press$	0.0	2.686E-5	normal	0.077	4.332E-4	2.8 %
\dot{m}_f	0.0773	0.00257				

Quantity	Value	Expanded Uncertainty	Coverage Factor	Coverage
\dot{m}_f	0.0773	± 0.005	2.0	95 % (normal)

Table 5.9.: Mass flow uncertainty normalised GUM Workbench Pro result table of OP13

Quantity	Value	Standard Uncertainty	Distribution	Sensitivity Coefficient	Uncertainty Contribution	Index
$\dot{m}_f, meas$	1.0000	1.665E-5	normal	1.0	1.685E-5	0.0 %
$\delta\dot{m}_f, cal$	0.0	2.503E-5	rectangular	1.0	5.295E-3	46.4 %
$\delta\dot{m}_f, leak$	0.0	2.777E-7	rectangular	1.0	5.777E-5	0.0 %
$\delta\dot{m}_f, press$	0.0	2.686E-5	normal	1.0	5.776E-3	53.6 %
\dot{m}_f	1.0000	0.00765				

Quantity	Value	Expanded Uncertainty	Coverage Factor	Coverage
\dot{m}_f	1.0000	± 0.0154	2.0	95 % (normal)

It is evident that both implementations, the GUM Workbench Pro output tables (Table 5.8 & Table 5.9) and the result of the applied equations (Table 5.10), lead to the identical result. When the expanded uncertainty is computed as relative percentage of the mass flow, a diminishing characteristic, similar to the calibration certificate, can be observed.

Table 5.10.: Mass flow uncertainty result table in normalised units

OP	\dot{m} [units]	u_e [units]	u_e [% of \dot{m}]
1	0.0773	± 0.0053	± 6.85
3	0.2334	± 0.0063	± 2.68
5	0.3895	± 0.0082	± 2.10
7	0.5457	± 0.0096	± 1.76
9	0.7017	± 0.0116	± 1.65
11	0.8580	± 0.0135	± 1.57
13	1.0000	± 0.0154	± 1.54

5.3.2. Thrust Uncertainty

For the thrust uncertainty calculation, the process is less straight forward, as the supplied method of the balance [41] differs substantially from the EPL procedure for other balances [6]. The supplied method used Equation 5.20, which only considers random influences of displacement x during the cross calibration and the effect from that on the sensitivity parameter S_{cal} .

$$\sigma_{F_t} = F_t \cdot \sqrt{\left(\frac{\sigma_x}{x}\right)^2 + \left(\frac{\sigma_{S_{cal}}}{S_{cal}}\right)^2} \quad (5.20)$$

However, this is considered overly optimistic, as there are more factors that influence the uncertainty that should be assessed individually. This is why the uncertainty model equation is expanded with further influences and is being brought into a more similar shape to the EPL thrust measurement procedure [6]. When the original equation $F = x/S_{cal}$ is used as a model equation for GUM, the sensitivity factor can not be computed by the partial derivative due to a division by zero. To solve this issue, the formula is readjusted to $F = x \cdot S_{cal}^{-1}$, where S_{cal}^{-1} is the pre-computed inverse. The new model equation that considers additional effects is shown in Equation 5.21 with the variable definitions in Table 5.11. Note that if the additional influences are set to zero, this model equation yields the same result as the supplied method.

$$F_t = \left(x_{meas} \cdot (1 + \delta x_{rand} + \delta x_{laser}) \cdot S_{cal,meas}^{-1} \cdot (1 + \delta S_{cal,rand}^{-1} + \delta S_{cal,align}^{-1})\right) \cdot (1 + \delta cos) \quad (5.21)$$

Table 5.11.: Variable definition of the thrust uncertainty budget calculation

Symbol	Unit	Definition
F_t	mN	Thrust to be determined
x_{meas}	mm	Displacement measurements, natural frequency filtered and zero reference adjusted
δx_{rand}	-	Standard uncertainty of the displacement due to random disturbances (supplied method)
δx_{laser}	-	Standard uncertainty due to the laser sensor non-linearity
$S_{cal,meas}^{-1}$	$\frac{mN}{mm}$	Sensitivity factor measurement by the cross calibration (pre-inversed)
$\delta S_{cal,rand}^{-1}$	-	Standard uncertainty of the sensitivity factor due to random disturbances (supplied method, pre-inversed)
$\delta S_{cal,align}^{-1}$	-	Standard uncertainty due to VCA alignment error during cross calibration
δcos	-	Uncertainty related to the misalignment of the thruster with the balance axis. If the uncertainty on the alignment angle is $\delta\alpha$, then $\delta cos = 0 \pm (1 - 1/\cos(\delta\alpha))$

Again, depending on the source of knowledge of the uncertainty, the contributions are classified as type A or type B. Type A are series of observations, where type B are other means than observations, for example approximations or theoretical models [28]. The different influences from the model equation are grouped and listed in Table 5.12 with their type and distribution.

Table 5.12.: Thrust uncertainty influences summary, types and distributions

Symbol	Value	Unit	Uncertainty	Type	Distribution	Sensitivity
x_{meas}	\bar{x}	mm	$s(\bar{x})$	A	experimental	\bar{S}_{cal}^{-1}
δx_{rand}	0	-	$u_{x,rand}$	B	normal	$\bar{x} \cdot \bar{S}_{cal}^{-1}$
δx_{laser}	0	-	$u_{x,laser}$	B	rectangular	$\bar{x} \cdot \bar{S}_{cal}^{-1}$
S_{cal}^{-1}	\bar{S}_{cal}^{-1}	$\frac{mN}{mm}$	$s(\bar{S}_{cal}^{-1})$	A	experimental	\bar{x}
$\delta S_{cal,rand}^{-1}$	0	-	$u_{S_{cal,rand}^{-1}}$	B	normal	$\bar{x} \cdot \bar{S}_{cal}^{-1}$
$\delta S_{cal,align}^{-1}$	0	-	$u_{S_{cal,align}^{-1}}$	B	rectangular	$\bar{x} \cdot \bar{S}_{cal}^{-1}$
δcos	0	-	u_{cos}	B	rectangular	$\bar{x} \cdot \bar{S}_{cal}^{-1}$

Displacement Measurements

The first newly considered influence comes from the displacement time series x_{meas} that is used for the thrust determination. The uncertainty for this influence is the standard deviation $s(x)$, more precisely the corrected sample standard deviation in Equation 5.22, of all N displacement measurements x_i .

$$s(x) = \sqrt{\frac{1}{N-1} \sum_{i=1}^N (x_i - \bar{x})^2} \quad (5.22)$$

As the uncertainty decreases when more samples N are acquired, the actual contribution to the uncertainty is defined as the standard deviation of the mean in Equation 5.23.

$$s(\bar{x}) = \frac{s(x)}{\sqrt{N}} \quad (5.23)$$

Note that the average of this data series \bar{x} is used for the non-zero contribution to the displacement value, as listed in Table 5.12. The sensitivity coefficient α can be yielded by the partial derivative on the model equation, as shown in Equation 5.10, where only \bar{S}_{cal}^{-1} remains as a non-zero value.

$$\alpha_{x,meas} = \frac{\partial F_t}{\partial x_{meas}} = \bar{S}_{cal}^{-1} \quad (5.24)$$

Random Disturbances in Displacement

This influence comes from the supplied method, from the balance authors dissertation [41]. Hereby are the deviations from the measurements to the fitting during the calibration used for an estimation on the uncertainty of the displacement. In Equation 5.25 is shown the computation of the uncertainty with the fitting intercept b_{cal} (from Equation 5.4) and S_{cal} (from Equation 5.3) and the used N points of force F_i shared between the VCA characterisation and the cross calibration.

$$\sigma_{x,rand} = \sqrt{\frac{\sum_{i=1}^N (x_i - b_{cal} - S_{cal} \cdot F_i)^2}{N-2}} \quad (5.25)$$

In order to get the standard uncertainty, this has to be normalised by \bar{x} as in Equation 5.26, due to the model formulation.

$$u_{x,rand} = \frac{\sigma_{x,rand}}{\bar{x}} \quad (5.26)$$

The sensitivity coefficient α is yielded by the partial derivative on the model equation (Equation 5.27).

$$\alpha_{x,rand} = \frac{\partial F_t}{\partial \delta x_{rand}} = \bar{x} \cdot \bar{S}_{cal}^{-1} \quad (5.27)$$

Laser Non-Linearity

The data sheet of the optoNDCT-1700-10 states a maximum deviation from linearity as 0.08% of the full scale output (FSO = 10 mm) [27]. Therefore, an uncertainty of $8\mu m$ for any distance measurement in the worst case. For a displacement measurement x two distance measurements are used. However, one of them, the zero reference, is yielded not only by one measurement but by a data series, which would actually reduce its uncertainty. However in favour of simplicity, the uncertainty for both distance measurements is assumed to be the worst case of the stated non-linearity. The standard half width of limits $hw_{x,laser}$ is determined by Equation 5.28, where the average displacement \bar{x} is entered in units of mm.

$$hw_{x,laser}(\bar{x}[mm]) = \frac{\sqrt{(0.008 \text{ mm})^2 + (0.008 \text{ mm})^2}}{\bar{x} [mm]} = \frac{0.008 \cdot \sqrt{2} \text{ mm}}{\bar{x} [mm]} \quad (5.28)$$

Due to the rectangular distribution the uncertainty u_{laser} is obtained through Equation 5.29.

$$u_{x,laser} = \frac{hw_{x,laser}}{\sqrt{3}} \quad (5.29)$$

The sensitivity coefficient α is yielded by the partial derivative on the model equation (Equation 5.30).

$$\alpha_{x,laser} = \frac{\partial F_t}{\partial \delta x_{laser}} = \bar{x} \cdot \bar{S}_{cal}^{-1} \quad (5.30)$$

Sensitivity Factor Measurements

The sensitivity factor is determined during the calibration in Section 5.1.1 and Section 5.1.2, where ideally this determination would be performed multiple times in order to gain a better estimate. This would mean multiple VCA characterisations and multiple cross calibrations in the same position. For multiple determinations of S_{cal} (and hence S_{cal}^{-1}), the uncertainty can be computed via Equation 5.31 and 5.32.

$$s(S_{cal}^{-1}) = \sqrt{\frac{1}{N-1} \sum_{i=1}^N (S_{cal,i}^{-1} - \bar{S}_{cal}^{-1})^2} \quad (5.31)$$

$$s(\bar{S}_{cal}^{-1}) = \frac{s(S_{cal}^{-1})}{\sqrt{N}} \quad (5.32)$$

In this test however, S_{cal} was only determined once, which gives no information on the standard deviation or uncertainty. Therefore, for $N = 1$ the value and uncertainty are defined through Equation 5.33.

$$\begin{aligned}\bar{S}_{cal}^{-1} &= S_{cal}^{-1} \\ s(\bar{S}_{cal}^{-1}) &= 0\end{aligned}\quad (5.33)$$

The sensitivity coefficient α is yielded by the partial derivative on the model equation (Equation 5.34).

$$\alpha_{Scal} = \frac{\partial F_t}{\partial S_{cal}^{-1}} = \bar{x} \quad (5.34)$$

Random Disturbances on Sensitivity Factor

This influence again stems from the supplied method by the balance authors dissertation [41]. The random disturbances on the displacement $u_{x,rand}$ from Equation 5.25 are now translated into the random disturbances on the sensitivity factor shown in Equation 5.35, with forces F_i and the average force \bar{F} .

$$\sigma_{Scal,rand} = \frac{u_{x,rand}}{\sqrt{\sum_{i=1}^N (F_i - \bar{F})^2}} \quad (5.35)$$

In order to get the standard uncertainty, the standard deviation is adjusted in Equation 5.36. Note that this standard uncertainty is already in the right form for the used model equation with the inverse sensitivity factor S_{cal}^{-1} , as it is now standardised.

$$u_{Scal,rand} = \frac{\sigma_{Scal,rand}}{\bar{S}_{cal}} \quad (5.36)$$

The sensitivity coefficient α is yielded by the partial derivative on the model equation (Equation 5.41).

$$\alpha_{Scal,rand} = \frac{\partial F_t}{\partial \delta S_{cal,rand}^{-1}} = \bar{x} \cdot \bar{S}_{cal}^{-1} \quad (5.37)$$

VCA Alignment

Another newly introduced influence is the alignment error of the VCA during the cross calibration. The operational procedure of the balance uses a linear stage to retract the coil assembly by a defined distance (2 mm) from the last point of contact, however this is not perfectly reproducible. This is a very crucial point, as the central calibration assumption is that the conditions are identical to the VCA characterisation, which is why this aspect should receive special attention. In order to examine how big of a difference a given misalignment would have on c_1 and therefore S_{cal} , the cross calibration was done additionally with 3 different retraction distances d . The results of the coil alignment test and the effect on an example thrust are listed in Table 5.13.

Table 5.13.: Effect of the coil alignment on the cross calibration gradient c_1

Test Setup	Coil Distance Last point of contact + d d [mm]	Cross Calibration Gradient c_1 [$\frac{mN}{mA}$]	Example Thrust $x = 0.25$ mm $v_1 = 0.54$ $\frac{mN}{mA}$
Initial cross calibration	2.0	0.001212515857964	111.3
Coil alignment test 1	1.5	0.001263485282264	106.8
Coil alignment test 2	2.0	0.001227258397413	110.0
Coil alignment test 3	2.5	0.001172004842578	115.2

From this data, a relationship between a change in retraction distance d and the cross calibration gradient c_1 is determined by a linear fit. The result is a $9.148044E - 5$ change in c_1 for each 1 mm of d . To put this into an uncertainty, d is estimated to be ± 0.1 mm reproducible, which is applied in Equation 5.38. Note that this assumed alignment error roughly matches the difference in c_1 observed between the two tests with the nominal retraction distance $d = 2.0$ mm.

$$\sigma_{c1} = \left(9.148044E - 5 \left[\frac{1}{mA} \right] \right) \cdot 0.1 [mm] = 9.148E - 6 \left[\frac{mN}{mA} \right] \quad (5.38)$$

The standard half width of limits in Equation 5.39 is also here already standardised and suited for the inverse sensitivity factor S_{cal}^{-1} .

$$hw_{Scal,align} = \frac{\sigma_{c1}}{c_1} \quad (5.39)$$

Due to the rectangular distribution, the final uncertainty for the VCA alignment error is shown in Equation 5.40.

$$u_{Scal,align} = \frac{hw_{Scal,align}}{\sqrt{3}} \quad (5.40)$$

The sensitivity coefficient α is yielded by the partial derivative on the model equation (Equation 5.41).

$$\alpha_{Scal,align} = \frac{\partial F_t}{\partial \delta S_{cal,align}^{-1}} = \bar{x} \cdot \bar{S}_{cal}^{-1} \quad (5.41)$$

Thrust Vector Alignment

Due to the thrust vector never being perfectly aligned with the axis of the balance, the measured thrust is only the axis component of the actual thrust. When $\delta\alpha$ is the angle of misalignment, then the real thrust can be determined via the trigonometric relationship $F_{real} = F_{axis} \cdot \frac{1}{\cos(\delta\alpha)}$. In the EPL thrust measurement procedure the usage of the equivalent term $F \cdot (1 + \delta\cos)$ in the model equation is demonstrated [6]. Also here the division by zero is prevented by pre-computing the numbers for $\delta\cos = 0 \pm (1 - 1/\cos(\delta\alpha))$. Here should be pointed out, that there is actually a mistake present, as with a symmetric uncertainty (\pm) the measured thrust on axis can also be reduced as an estimate for the real thrust. However, that the real thrust is lower than the measured thrust is physically impossible. The correct formulation of the

uncertainty due to misalignment therefore needs to be asymmetric with no reducing part of the on-axis thrust. However, the necessary correction will be postponed to a later date, in favor to reach compliance with the current procedure. As the angle of misalignment can not easily be measured, $\delta\alpha$ is estimated to 3° which is a common conservative estimation from the EPL procedure [6], which is shown in Equation 5.42.

$$hw_{cos} = \left| 1 - \frac{1}{\cos(\delta\alpha)} \right| = \left| 1 - \frac{1}{\cos(3^\circ)} \right| \approx 0.00137235 \quad (5.42)$$

When the rectangular distribution is applied, the final uncertainty can be expressed in Equation 5.43

$$u_{cos} = \frac{hw_{cos}}{\sqrt{3}} \quad (5.43)$$

The sensitivity coefficient α is yielded by the partial derivative on the model equation (Equation 5.44).

$$\alpha_{cos} = \frac{\partial F_t}{\partial \delta cos} = \bar{x} \cdot \bar{S}_{cal}^{-1} \quad (5.44)$$

Combined

The combined uncertainty can be calculated by the weighted sum for all n influences in Equation 5.45.

$$u_c = \sqrt{\sum_{i=1}^n (\alpha_i^2 \cdot u_i^2)} \quad (5.45)$$

Where the sum is explicitly formulated in Equation 5.46.

$$\begin{aligned} \sum_{i=1}^n (\alpha_i^2 \cdot u_i^2) = & \alpha_{x,meas}^2 \cdot s(\bar{x})^2 + \alpha_{x,rand}^2 \cdot u_{x,rand}^2 + \alpha_{x,laser}^2 \cdot u_{x,laser}^2 + \alpha_{Scal}^2 \cdot s(\bar{S}_{cal}^{-1})^2 + \\ & \alpha_{Scal,rand}^2 \cdot u_{Scal,rand}^2 + \alpha_{Scal,align}^2 \cdot u_{Scal,align}^2 + \alpha_{cos}^2 \cdot u_{cos}^2 \end{aligned} \quad (5.46)$$

Finally, the combined uncertainty is expanded with a coverage factor k , which is set to $k = 2$ for a 95 % coverage level. This yields the expanded uncertainty u_e in Equation 5.47, which is rounded to one digit after the decimal as absolute value.

$$u_e = k \cdot u_c \quad (5.47)$$

The uncertainty calculation was again executed both by applying the listed equations and with the GUM Workbench Pro software. The result table from the GUM software is shown for OP1 and OP13 in Table 5.14 and Table 5.15, which are the operation points with the lowest and the highest thrust. When also here the Index value is observed in Table 5.14, it can be seen that the uncertainty is dominated by the uncertainty of the lasers non-linearity and secondly influenced by the random disturbances on the displacement. For higher thrust levels in Table 5.15, more influences start to rise in significance, which are being the random disturbances on the sensitivity value and the VCA alignment error.

Table 5.14.: Thrust uncertainty normalised GUM Workbench Pro result table of OP1

Quantity	Value	Standard Uncertainty	Distribution	Sensitivity Coefficient	Uncertainty Contribution	Index
x_{meas}	1.5726E-4	6.104E-8	normal	450	4.342E-5	0.0 %
δx_{rand}	0.0	1.033E-3	normal	0.070344	8.337E-3	9.8 %
δx_{laser}	0.0	3.135E-3	rectangular	0.070344	2.518E-2	90.2 %
$S_{cal,meas}^{-1}$	445.40076	0.0	normal	1.57E-4	0.0	0.0 %
$\delta S_{cal,rand}^{-1}$	0.0	3.040E-5	normal	0.070344	2.432E-4	0.0 %
$\delta S_{cal,align}^{-1}$	0.0	3.786E-5	rectangular	0.070344	3.040E-4	0.0 %
δcos	0.0	6.878E-6	rectangular	0.070344	5.558E-5	0.0 %
F_t	0.070045	0.026748				

Quantity	Value	Expanded Uncertainty	Coverage Factor	Coverage
F_t	0.070	± 0.05345	2.0	95 % (normal)

Table 5.15.: Thrust uncertainty normalised GUM Workbench Pro result table of OP13

Quantity	Value	Standard Uncertainty	Distribution	Sensitivity Coefficient	Uncertainty Contribution	Index
x_{meas}	2.2452E-3	9.076e-08	normal	450	6.426E-5	0.0 %
δx_{rand}	0.0	7.243E-3	normal	1.0421	8.337E-3	9.4 %
δx_{laser}	0.0	2.197E-4	rectangular	1.0421	2.518E-2	86.3 %
$S_{cal,meas}^{-1}$	445.40076	0.0	normal	2.25E-3	0.0	0.0 %
$\delta S_{cal,rand}^{-1}$	0.0	E-5	normal	1.0421	3.474E-3	1.7 %
$\delta S_{cal,align}^{-1}$	0.0	E-5	rectangular	1.0421	4.342E-3	2.6 %
δcos	0.0	E-6	rectangular	1.0421	7.902E-4	0.0 %
F_t	1.0000	0.028345				

Quantity	Value	Expanded Uncertainty	Coverage Factor	Coverage
F_t	1.0000	± 0.05669	2.0	95 % (normal)

The result of the thrust uncertainty budget calculation for all operation points is stated in Table 5.16.

Table 5.16.: Thrust uncertainty result table in normalised units

OP	F [units]	u_e [units]	u_e [% of F]
1	0.0700	± 0.0534	± 76.30
3	0.2272	± 0.0530	± 23.31
5	0.3810	± 0.0535	± 14.05
7	0.5356	± 0.0538	± 10.05
9	0.6930	± 0.0539	± 7.78
11	0.8514	± 0.0541	± 6.35
13	1.0000	± 0.0567	± 5.67

5.3.3. Specific Impulse Uncertainty

The uncertainty of the specific impulse I_{sp} can be computed directly from the results of the mass flow uncertainty and the thrust uncertainty. The model equation is the general formula of specific impulse in Equation 5.48 with the standard gravity $g_0 = 9.80665 \frac{m}{s^2}$ [34].

$$I_{sp} = \frac{F}{\dot{m} \cdot g_0} \quad (5.48)$$

The combined uncertainty can be determined by Equation 5.49 from both combined uncertainties $u_{c,\dot{m}}$ (Equation 5.18) and $u_{c,F}$ (Equation 5.45), where I_{sp} , \dot{m} and F are holding the absolute value for each operation point.

$$u_{c,I_{sp}} = I_{sp} \cdot \sqrt{\left(\frac{u_{c,\dot{m}}}{\dot{m}}\right)^2 + \left(\frac{u_{c,F}}{F}\right)^2} \quad (5.49)$$

This combined uncertainty is again expanded by the coverage factor $k = 2$ into Equation 5.50.

$$u_e = k \cdot u_{c,I_{sp}} \quad (5.50)$$

Table 5.17 shows the result of the expanded uncertainties for all operation points, which are highly dominated by the uncertainty contribution of thrust.

Table 5.17.: Specific impulse uncertainty result table in normalised units

OP	I_{sp} [units]	u_e [units]	u_e [% of I_{sp}]
1	0.9061	± 0.6938	± 76.56
3	0.9731	± 0.2284	± 23.47
5	0.9784	± 0.1389	± 14.20
7	0.9814	± 0.1002	± 10.21
9	0.9875	± 0.0786	± 7.96
11	0.9923	± 0.0649	± 6.54
13	1.0000	± 0.0587	± 5.87

5.4. Chamber Response

From the experimental results of the cold flow test in Table 5.4, the relationship between \dot{m} and p_{back} is used to determine the pumping speed of the vacuum facility and its effective pressure response. The result is a linear dependency between the injected mass flow and resulting vacuum pressures, that corresponds to the pumping speed of the used roughing pump system. The determined pumping speed is a relatively steady 87 L/s (Argon), which is a good resemblance of the 111 L/s (air) specification of the manufacturer. The effective pumping speed S_{eff} was computed via $S_{eff} = R_0 \cdot T_{gas} \cdot \dot{m} / (\mathfrak{M} \cdot (p_{back} - p_{back,ult}))$, with the gas temperature inside the vacuum facility T_{gas} and the ultimate pressure $p_{back,ult}$.

5.5. Model Comparison

The experimentally determined results from Section 5.2 are now compared to the simulation results of the model from Section 3.3.2. Due to the breakdown of one heater during the heat-up phase, only the performance under cold flow condition was experimentally characterised, however the model was additionally executed for elevated temperatures, to draw out the expected effects. The visual comparison of both results is plotted in Figure 5.18, which shows the most characteristic variables \dot{m} , F and I_{sp} . Additionally, the result of a previous experimental characterisation of the *Acceptance Test* is shown.

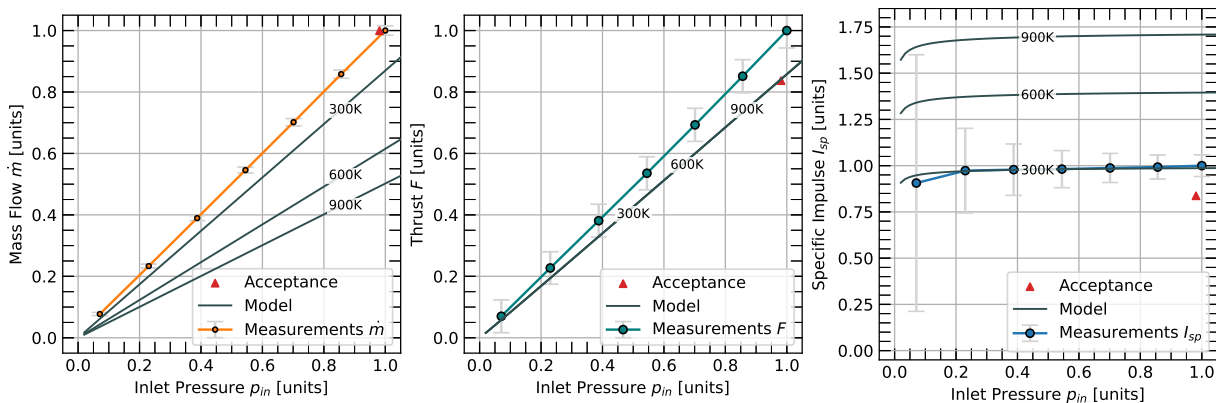


Figure 5.18.: Performance map of the XR-100 in cold gas mode compared to the model

From this figure, multiple observations can be derived. Starting at the mass flow, a clear difference between the expected mass flow at 300K and the measured mass flow can be seen. This deviation of roughly 10 % was already found before the *Acceptance Test* and is mentioned in a technical report from ALTA as a so called "mass flow anomaly" of this thruster unit [35]. The settled explanation that is stated in this report is a leak at the thruster body, with the justification that otherwise the expected thrust was met. This was concluded as confirmed, as both the ALTA internal tests and the EPL *Acceptance Test* measured both the mass flow deviation and the expected thrust. Therefore does the measurement align with previous tests and the deviation in mass flow to the theoretical model persists.

Comparing the thrust level next, the measurements show a clear overshoot to the expected value of the model, but this time also an overshoot to the *Acceptance Test*. The thrust measurements have been previously compared in Section 5.2.1 in Figure 5.15 to the theoretical model from ALTA and more previous tests, which suggests that the true thrust level lies somewhere between the measurements of this test and the *Acceptance Test*. In that case, the model would fit reality decently with a slight underestimation, however for the measurements of this thrust balance it means that a high uncertainty is present. The result of the uncertainty calculation from Section 5.3.2 is shown here in error bars which could explain part of up for the difference to the considered true value. Note that an uncertainty can only be as good as the considered effects and the modelling of that

For the specific impulse, the model perfectly aligns with the measurements, which must be a coincidental cancellation of the mass flow anomaly and the thrust overshoot of the ICL balance. When the true I_{sp} lies again between the measurements and the *Acceptance Test*, the model provides a decent prediction with an overestimation that could be explained by the mass flow anomaly.

6. Conclusion and Outlook

In order to arrive at the planned test conditions for the characterisation, the experimental test set up at the ESA Propulsion Laboratory required a great effort in preparation. The available hardware hereby showed a great influence on the ease of use and quality of the acquired data. Where the most hardware showed a seamless commissioning, the Imperial College London thrust balance required a deep dive into its functionality as improvements have been desired. The operation of the thrust balance was upgraded by the automation of the execution of calibration procedures as well as their post processing. Furthermore, an uncertainty budget calculation was developed for the thrust balance in compliance with the EPL operational procedures, which now considers multiple additional effects. Yet, the uncertainty budget calculation is still one of the main points to improve on for this balance in future work, as a noticeable deviation in thrust was measured from previous tests with this thruster unit, that can only be partially explained with the currently determined uncertainty. Next to the identification of the true uncertainty, active countermeasures could be implemented in future to lower the uncertainty physically. This could be approached by investigating and characterising the effects with the highest contribution to the combined uncertainty first, which presupposes that the effect is included in the first place.

The execution of the characterisation was successful for the cold flow operation of the XR-100 resistojet, however unsuccessful for the resistojet in hot flow mode, due to the breakage of one of the two internal heaters during the heat-up phase. The presence of two heaters in the resistojet was designed with the goal of redundancy in mind, however instead being implemented as a fail-safe mechanism, the thruster became unusable at nominal voltage after the breakdown of one heater, due to triggered safety shut-offs in the control software. In fact, the initially planned redundancy was already compromised by the nominal operation being defined to run both heaters in parallel, as one heater alone is not capable to deliver the nominal performance. Furthermore, the design of the filament, was optimised for efficiency in the heat transfer and the maximum gas temperature, however this came by the price of fragility of the filament itself. As a comparison, the single filament XR-150 resistojet was instead designed for robustness, with a slightly lower gas temperature [37], but has been proven to outlast the now already second failure of this XR-100 thruster unit. This sets an example that reliability does not always need to be approached by redundancy, but can be achieved with robustness instead.

The general methodology of the characterisation of a thruster was attempted to be carried out with the variation of each of the relevant operational parameters to create a performance map across the entire possible operational range. For the resistojet these degrees of freedom in operation are essentially the inlet pressure and the power input. The performance was characterised for a series of steps in the inlet pressure during the cold flow mode, which covers one degree of freedom of the thruster. However, it was not possible to me to apply also a step-wise variation in the power input, due to guiding restraints as it was not explicitly allowed in the user manual, but ultimately also due to the heater breakdown. In a future work all degrees of freedom should be explored to provide a full characterisation of a thruster.

Bibliography

- [1] Albertoni, R.; Paganucci, F.; Andrenucci, M.: A phenomenological performance model for applied-field MPD thrusters. *Acta Astronautica*, Vol. 107, pp. 177–186, 2015.
- [2] Alnaqbi, S.; Darfilal, D.; Swei, S. S. M.: Propulsion Technologies for CubeSats: Review. *Aerospace*, Vol. 11, No. 7, p. 502, June 2024.
- [3] Barrère, M.; Jaumotte, A. L.; Veubeke, B. F. de; Vandenkerckhove, J.; Schneider, W. K.; Kármán, T. von: *Raketenantriebe*, Amsterdam: Elsevier, 1961.
- [4] Bock, D.; Herdrich, G.; Lau, M.; Lengowski, M.; Schönherr, T.; Steinmetz, F.; Wollenhaupt, B.; Zeile, O.; Röser, H.-P.: Electric propulsion systems for small satellites: the low earth orbit mission perseus. In: *Progress in Propulsion Physics*, 2011.
- [5] Borràs, E. B.: EPL Process Definition, ESA-TECMP-EPL-PR-004710 V4.5, Mar. 2017.
- [6] Borràs, E. B.: Thrust Measurement Procedure - Operational Procedure, ESA-TECMP-EPL-PR-004713 V1.0, Apr. 2017.
- [7] Borràs, E. B.; Amo, J. G. del; Hughes, B.: ISO17025 Accreditation of the ESA Micro-Newton Thrust Balance. In: *Joint Conference of 30th International Symposium on Space Technology and Science, 34th International Electric Propulsion Conference, and 6th Nano-satellite Symposium*, July 2015.
- [8] Boxberger, A.; Behnke, A.; Herdrich, G.: Current Advances in Optimization of Operative Regimes of Steady State Applied Field MPD Thrusters. In: *36th International Electric Propulsion Conference, IEPC-2019-585*, Sept. 2019.
- [9] Bulit, A.; Borràs, E. B.: Acceptance test of XR-100 resistojet and Direct Thrust Measurement - ISO17025 Test - Test Report, TEC-MP/2013/1301/AB V1.0, Oct. 2013.
- [10] Chase, M.: *NIST-JANAF Thermochemical Tables*, 4th Edition, American Institute of Physics, -1, 1998-08-01 1998.
- [11] Croes, V.: *Modélisation bidimensionnelle de la décharge plasma dans un propulseur de Hall*. Université Paris Saclay (COMUE), PhD thesis, 2017SACLX060, Oct. 2017.
- [12] Dannemeyer, K.; Schönherr, T.: Krypton Large IMPulse Thruster - KLIMT test at EPL ISO 17025 test, TECMP/2016/1551/KD V1.0, June 2016.
- [13] Daras, I.; March, G.; Mass Chng Mission Expert Group, J.; Wiese, D.; Blackwood, C.; Forman, F.; Loomis, B.; Luthcke, S.; Peralta-Ferriz, C.; Sauber-Rosenberg, J.; Eicker, A.; Panet, I.; Visser, P.; Meyssignac, B.; Wouters, B.; Bamber, J.; Pail, R.; Flechtner, F.: *Next Generation Gravity Mission (NGGM) Mission Requirements Document*, Sept. 2023.
- [14] Desai, P. D.; Chu, T. K.; James, H. M.; Ho, C. Y.: Electrical Resistivity of Selected Elements. *Journal of Physical and Chemical Reference Data*, Vol. 13, No. 4, pp. 1069–1096, Oct. 1984.

- [15] Djamal, D.; Mohamed, K.; Aslan, A. R.: RESISTOJET Propulsion System for Small Satellite. 2019 9th International Conference on Recent Advances in Space Technologies (RAST), pp. 159–166, 2019.
- [16] Egbert, R. B.: Heat transmission by radiation from gases. Massachusetts Institute of Technology, PhD thesis, 1941.
- [17] Eizinger, M.; Bianchi, L.: HT100-SHC1000 Coupling Test - Test Plan, ESA-TECMPE-EPL-TP-024257 V1.0, Mar. 2021.
- [18] Electrothermal Thrusters – Resistojets - SITAEL, <https://www.sitael.com/space/advanced-propulsion/electric-propulsion/> (accessed 2024-09-22), 2024.
- [19] ESA Propulsion Laboratory (EPL) - ESA, https://www.esa.int/ESA_Multimedia/Images/2009/08/ESA_Propulsion_Laboratory_EPL (accessed 2024-09-22), 2009.
- [20] Gibbon, D.; Baker, A.; Coxhill, I.; Sweeting, M. N.: The Development of a Family of Resistojet Thruster Propulsion Systems for Small Spacecraft. In: 2003.
- [21] Goebel, D. M.; Katz, I.: Fundamentals of electric propulsion, Jet Propulsion Laboratory - NASA, 2008.
- [22] HEMPT-NG EU Project: High Efficiency Multistage Plasma Thruster – Next Generation - Technology, <https://www.hempt-ng.eu/hempt-ng-technology.html> (accessed 2024-09-15), 2023.
- [23] Hofer, R.; Simmonds, J.; Goebel, D.; Steinkraus, J.; Payman, A.: The H10 High Power Density Hall Thruster. In: 38th Int. Electric Propulsion Conf. IEPC-2024-515, 2024.
- [24] Holkeboer, D. H.; Jones, D. W.; Pagano, F.; Santeler, D.: Vacuum Technology and Space Simulation, 1966.
- [25] Holste, K.; Dietz, P.; Scharmann, S.; Keil, K.; Henning, T.; Zschätzsch, D.; Reitemeyer, M.; Nauschütt, B.; Kiefer, F.; Kunze, F.; Zorn, J.; Heiliger, C.; Joshi, N.; Probst, U.; Thüringer, R.; Volkmar, C.; Packan, D.; Peterschmitt, S.; Brinkmann, K. .-.; Zaunick, H.-G.; Thoma, M. H.; Kretschmer, M.; Leiter, H. J.; Schippers, S.; Hannemann, K.; Klar, P. J.: Ion thrusters for electric propulsion: Scientific issues developing a niche technology into a game changer. *Review of Scientific Instruments*, Vol. 91, No. 6, p. 061101, June 2020.
- [26] Hutchins, M.; Simpson, H.; Palencia Jimnez, J.: QinetiQ’s T6 and T5 Ion Thruster Electric Propulsion System Architectures and Performances, Joint Conference of 30th International Symposium on Space Technology and Science. In: 34th International Electric Propulsion Conference, and 6th Nano-satellite Symposium, Hyogo-Kobe, Japan, 2015.
- [27] Instruction Manual optoNCDDT 1700 optoNCDDT 1710 – MICRO-EPSILON, <https://www.micro-epsilon.pl/download/man--optoncdt-1700--en.pdf> (accessed 2024-10-31), 2024.
- [28] Joint Committee for Guides in Metrology: Evaluation of Measurement Data — Guide to the Expression of Uncertainty in Measurement, Paris, France: JCGM, Sept. 2008.
- [29] Koppel, C.; Marchandise, F.; Estublier, D.; Jolivet, L.: The SMART-1 electric propulsion subsystem in flight experience. In: 40th AIAA/ASME/SAE/ASEE Joint Propulsion Conference and Exhibit, 2004.
- [30] Krejci, D.; Reissner, A.; Seifert, B.; Jelem, D.; Hörbe, T.; Plesescu, F.; Friedhoff, P.; Lai, S.: Demonstration of the IFM Nano FEEP Thruster in Low Earth Orbit. In: The 4S Symposium 2018, 2018.

-
- [31] Linstrom, P.: NIST Chemistry WebBook, NIST Standard Reference Database 69, 1997.
- [32] Mohr, P. J.; Tiesinga, E.; Newell, D. B.; Taylor, B. N.: *Codata Internationally Recommended 2022 Values of the Fundamental Physical Constants*, 2024-05-08 04:05:00 2024.
- [33] Muñoz Tejada, J.; Knoll, A.; Marchioni, F.; Cappelli, M.: Plasma properties characterisation of oxygen-fuelled Hall Effect Thrusters for Water Electrolysis propulsion. In: May 2024.
- [34] Newell, D.; Tiesinga, E.: *The International System of Units (SI)*, 2019 Edition, Aug. 2019.
- [35] Passaro, A.: *Refurbished XR100-01 Resistojet System Acceptance - Report*, ALTA/SPF/TN-33 V1.0, Aug. 2013.
- [36] Passaro, A.; Caredda, P.; Gabbani, M.: *XR100 ResistoJet Complete System - User Manual*, ALTA/SPF/TN/32i2 V2.2, Aug. 2013.
- [37] Passaro, A.; Pieri, L.: *XR150 ResistoJet Complete System - User Manual*, ALTA/SPF/TN/34 V1.1, Sept. 2012.
- [38] Schönherr, T.: *Mass Flow Measurement Procedure - Operational Procedure*, ESA-TECMP-EPL-PR-004715 V5.1, Apr. 2017.
- [39] Schönherr, T.; Little, B.; Krejci, D.; Reissner, A.; Seifert, B.: Development, production, and testing of the IFM nano FEEP thruster. In: *36th International Electric Propulsion Conference*, 2019.
- [40] Schwertheim, A.: *Imperial College London Thrust Balance User Manual*, V1.1, Feb. 20, 2020.
- [41] Schwertheim, A.: *The Water Electrolysis Hall Effect Thruster*. Imperial College London, PhD thesis, May 2022.
- [42] Shimmin, R.: Trajectory design for a very-low-thrust lunar mission. In: 2013.
- [43] Snyder, J.; Goebel, D. M.; Hofer, R. R.; Polk, J. E.; Wallace, N. C.; Simpson, H.: Performance Evaluation of the T6 Ion Engine. *Journal of Propulsion and Power*, Vol. 28, No. 2, pp. 371–379, Mar. 2012.
- [44] Starlink 1010, NASA Space Science Data Coordinated Archive, <https://nssdc.gsfc.nasa.gov/nmc/spacecraft/display.action?id=2019-074D> (accessed 2024-11-03), 2019.
- [45] Steinert, S.; Bäckström, T.: *XR100 Resistojet Characterisation with the Imperial College London Thrust Balance - Test Plan*, ESA-TECMPE-TP-2024-002557 V1.1, Sept. 2024.
- [46] Steinert, S.; Bäckström, T.: *XR100 Resistojet Characterisation with the Imperial College London Thrust Balance - Test Report*, ESA-TECMPE-TR-2024-002904 V1.0, Sept. 2024.
- [47] Steinert, S. J.: *Design of a Hall Thruster and Investigation for a Water Electrolysis Propulsion System*. Semesterthesis, Mar. 2024.
- [48] Sutton, G. P.; Biblarz, O.: *Rocket Propulsion Elements*, Nashville, TN: John Wiley & Sons, Dec. 2016.
- [49] Tsay, M.; Frongillo, J.; Hohman, K.: Iodine-fueled mini RF ion thruster for CubeSat applications. In: *34th International Electric Propulsion Conference*, Kobe, Japan, 2015.
- [50] Volkmar, C.; Geile, C.; Hannemann, K.: Radio-Frequency Ion Thrusters—Power Measurement and Power Distribution Modeling. *Journal of Propulsion and Power*, Vol. 34, No. 4, pp. 1061–1069, July 2018.

- [51] Wachs, B.; Jorns, B.: Technique for two-frequency optimization of an ECR magnetic nozzle thruster. In: Proceedings of the 36th International Electric Propulsion Conference, Vienna, Austria, 2019.
- [52] White, F. M.: Fluid mechanics, McGraw-Hill, 1999.
- [53] XR resistojet product family: Product Sheet - SITAEL, https://satcatalog.s3.amazonaws.com/components/937/SatCatalog_-_SITAEL_-_XR-100_-_Datasheet.pdf (accessed 2024-09-15), 2015.

A. Appendix

A.1. Resistivity of Tungsten

Table A.1.: Resistivity of tungsten depending on temperature (data from [14])

$T[K]$	$\rho_W[10^{-8}\Omega m]$	$T[K]$	$\rho_W[10^{-8}\Omega m]$	$T[K]$	$\rho_W[10^{-8}\Omega m]$
0	0.0000150	200	3.18	1500	40.33
1	0.0000157	250	4.30	1600	43.65
4	0.0000267	273	4.82	1700	47.01
7	0.0000580	293	5.28	1800	50.41
10	0.000137	298	5.40	1900	53.85
15	0.000567	300	5.44	2000	57.33
20	0.00196	400	7.83	2200	64.41
25	0.00553	500	10.35	2400	71.63
30	0.0133	600	13.00	2600	79.00
40	0.0543	700	15.76	2800	86.51
50	0.141	800	18.61	3000	94.18
60	0.266	900	21.53	3200	102.00
70	0.422	1000	24.51	3400	110.00
80	0.606	1100	27.57	3600	118.30
90	0.809	1200	30.68	3660	120.80
100	1.020	1300	33.84		
150	2.088	1400	37.06		

A.2. Flank Detection Algorithm

In order to reliably detect the known pattern, multiple methods of pattern recognition have been tried out and the following algorithm finally delivered satisfactory results. The recording is analysed from the back to the front, where the idea is here, that the pattern is best recognisable by its biggest signal peak in the sequence. In the case of the VCA characterisation, the biggest signal is the last signal. Later this detection algorithm was also used for the in-situ calibration, where a backwards evaluation would not necessarily be required anymore, as the peak signal is now in the middle of the pattern, but the code was instead kept to evaluate backwards just with a different starting position near the maximum value in the recording. The key identifier that was selected is the so called peak-to-peak value of a window of a given time frame that is shifted over the data to create the peak-to-peak value signal. The width of the window, hence the time section was chosen to be 2 times the natural period of the signal. The natural period was derived by multiplying the sample frequency with the natural frequency of the balance. The natural frequency was determined via the main magnitude in the frequency domain between 0.5 Hz and 1.5 Hz, that was computed via an FFT. This peak-to-peak value from the shifted window is very steadily increasing before the flank is reached, which represents the slow dampening of the oscillation.

When the flank in the distance measurement is reached, the peak-to-peak value will experience a local maximum that drops as soon the window does not cover the full flank anymore. Through this window evaluation, the hardly detectable flank in the oscillating distance measurement has been converted into a steady but narrow bell curved characteristic. After this local maximum is crossed and the peak-to-peak value falls under 80 % of again, this window evaluation is stopped and the center of the flank can now be found by the bell curve alone. On this bell shaped cure, the center of the peak is identified by taking the center value of the steep gradients. This is evaluated at 80 % of the maximum value before and after the maximum, where then, the middle point in time aligns perfectly with the center point of the flank in the original distance measurements.

A.3. Heat Capacity Ratio Map of Argon

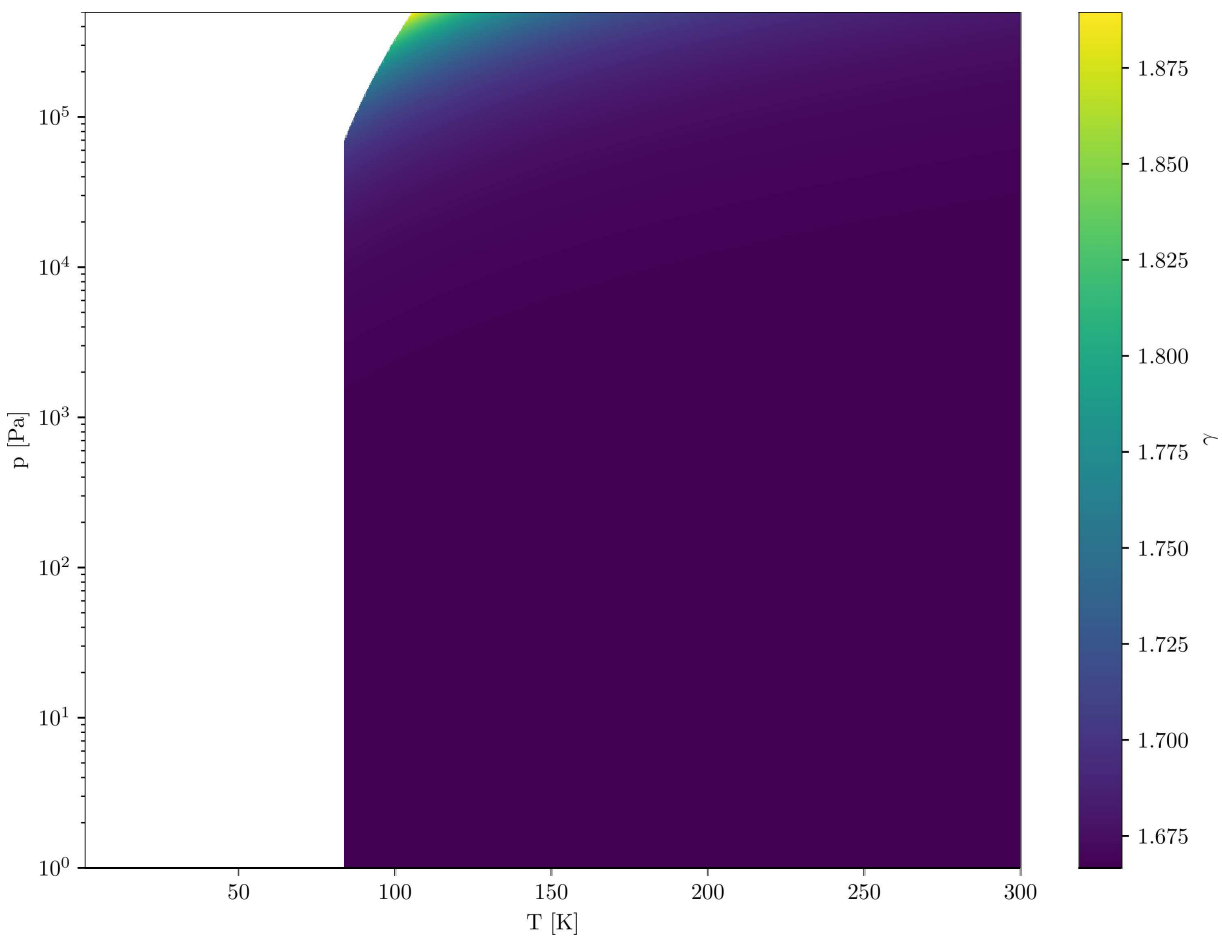


Figure A.1.: The heat capacity ratio γ of the gas phase of argon depending on temperature and pressure (obtained through CoolProp, with missing information below the triple point temperature)

A.4. VCA Characterisation Data

Table A.2.: Result data table of the VCA Characterisation

I_{VCA} (mA)	Measured Mass (g)		Corrected Mass (g)	F_{VCA} (mN)
Current Measured	Mass reading before current applied	Mass reading while current applied	Change in Mass	VCA Force
0.100001	0.0254	0.0317	0.0063	0.0618
0.50000	0.0254	0.0538	0.0284	0.2785
0.99998	0.0254	0.0814	0.0560	0.5492
2.5000	0.0255	0.1641	0.1386	1.3592
5.0000	0.0262	0.3018	0.2756	2.7027
7.4999	0.0263	0.4395	0.4132	4.0521
9.9999	0.0263	0.5773	0.5510	5.4035
25.000	0.0263	1.4038	1.3775	13.5087
50.001	0.0263	2.7812	2.7549	27.0163
75.001	0.0263	4.1583	4.1320	40.5211
99.998	0.0263	5.5351	5.5088	54.0229
125.02	0.0263	6.9144	6.8881	67.5492
150.00	0.0263	8.2901	8.2638	81.0402
174.97	0.0264	9.6656	9.6392	94.5283
199.98	0.0263	11.0427	11.0164	108.0340
224.99	0.0264	12.4195	12.3931	121.5348
250.02	0.0264	13.7972	13.7708	135.0454
275.01	0.0263	15.1724	15.1461	148.5325
299.98	0.0263	16.5470	16.5207	162.0127
349.99	0.0264	19.2985	19.2721	188.9947
400.02	0.0264	22.0478	22.0214	215.9562
450.00	0.0263	24.7964	24.7701	242.9117
500.03	0.0264	27.5467	27.5203	269.8819
600.02	0.0263	33.0423	33.0160	323.7764
800.02	0.0263	44.0224	43.9961	431.4544
1000.00	0.0264	54.9902	54.9638	539.0107

A.5. Cross Calibration Data

Table A.3.: Result data table of the auto cross calibration

I (mA)	Laser Distance		D (mm)
	Reference Zero	Reference Enabled	Displacement
0.1	5.6009	5.6008	0.000075577
0.5	5.6009	5.6003	0.000641792
1.0	5.6009	5.5998	0.001130020
2.5	5.6011	5.5980	0.003096597
5.0	5.6011	5.5948	0.006246860
7.5	5.6009	5.5916	0.009363764
10.0	5.6010	5.5884	0.012585122
25.0	5.6008	5.5698	0.031070145
50.0	5.6007	5.5386	0.062064762
75.0	5.6004	5.5078	0.092640550
100.0	5.6003	5.4771	0.123277623
125.0	5.6001	5.4465	0.153613602
150.0	5.6001	5.4159	0.184183346
175.0	5.6001	5.3856	0.214450287
200.0	5.6000	5.3552	0.244800255
225.0	5.5998	5.3251	0.274689972
250.0	5.5997	5.2949	0.304760762
275.0	5.5996	5.2653	0.334270352
300.0	5.5993	5.2356	0.363698844
350.0	5.5990	5.1772	0.421814568

A.6. EPL Noise Characterisation

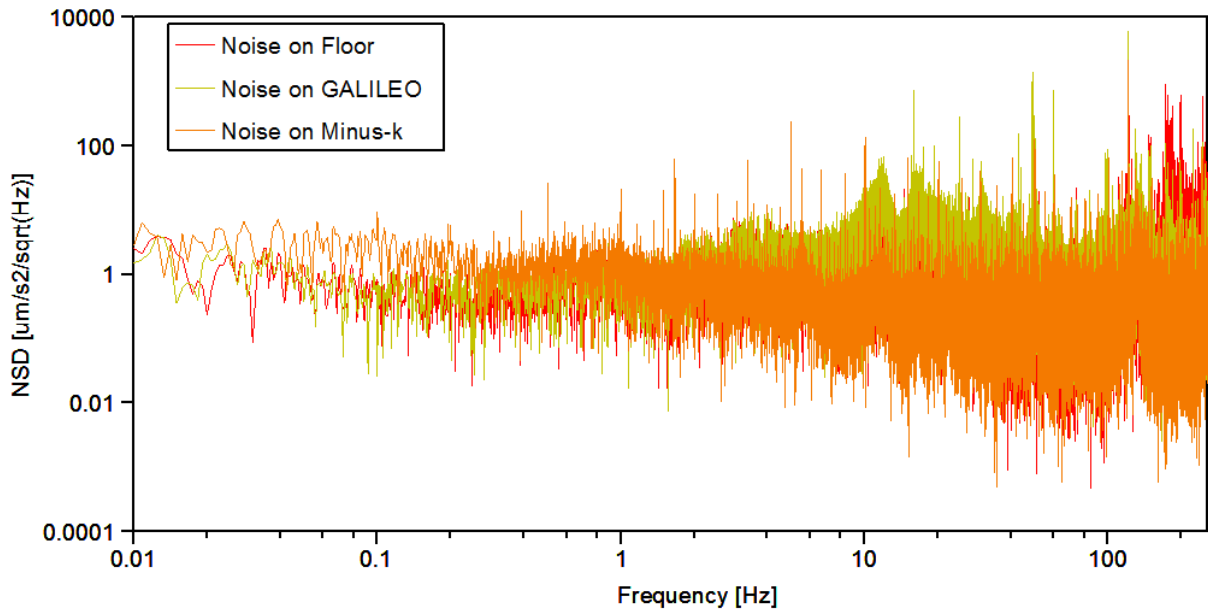


Figure A.2.: Noise spectral density (NDS) on structures with no thrust applied of a previous test (published by Bosch Borrás [7]) in the vacuum facility GALILEO on the uNTB

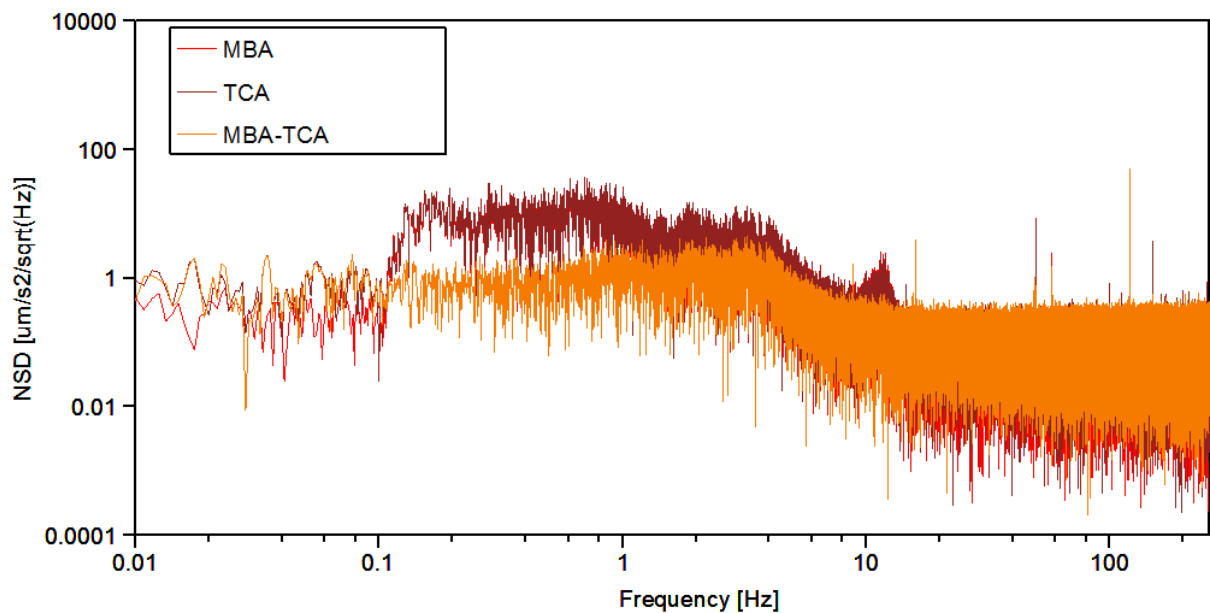


Figure A.3.: Noise spectral density (NDS) with thrust applied of a previous test (published by Bosch Borrás [7]) in the vacuum facility GALILEO on the uNTB